DEPARTMENT OF ECONOMICS

PhD IN SCIENCE AND MANAGEMENT OF CLIMATE CHANGE

FINAL DISSERTATION

Development and application of new methods to perform Iron Speciation in ice cores

PhD Candidate:

François Burgay

956210

Tutor:

Prof. Carlo Barbante

Co-tutor:

Dott. Andrea Spolaor

XXXI Cycle
February 2019

Summary

Abstract

Since Martin first published the "Iron hypothesis" that linked the Marine Primary Productivity (MPP) in the High Nutrient Low Chlorophyll (HNLC) Area to the Fe availability, the Iron biogeochemical cycle has been one of the most studied cycles on Earth. Understanding the Fe sources and how they might evolve under a global warming scenario, becomes crucial to unravel how the climate system might develop in the next decades. In particular, the Fe delivery from iceberg melting and glacial runoff will become increasingly important in a warmer world. These sources will potentially promote negative feedbacks that might dampen the increase in atmospheric CO_2. Volcanoes represent another important source of soluble Fe. They have been recognized as significant Fe^{2+} and soluble iron emitters. Remote sensing studies and in-situ surveys from terrestrial (e.g. Ejyafjallajokull, Kasatochi) and submarine volcanoes (e.g. El Hierro), showed that, because of their significant Fe^{2+} and soluble Fe emissions, they can increase the marine productivity. The Spirakis hypothesis, postulated in the 90's, questioned the role of volcanoes in promoting MPP in the HNLC regions suggesting that Plinian and Ultra-Plinian eruptions might have a crucial role in causing a net decrease in atmospheric CO_2 (e.g. after the Pinatubo eruption).

Ice cores represent the perfect archive from where it is possible to answer this critical environmental and climatic question. This thesis, through the development of a new method, that is able to quantify and detect Fe^{2+} species, and through the optimization of an existing method for the total soluble Fe, represents the first step to address the Spirakis hypothesis.

The successful application of the CFA-CL-Fe^{2+} method and the total soluble Fe method on a Greenland ice core showed that Fe^{2+} high-resolution quantification is feasible in ice core and that volcanic eruptions have a clear fingerprint on the ice cores. Furthermore, studying the Fe post-depositional processes on a Svalbard ice core, the relevance of organic ligands in promoting the Fe^{2+} dissolution has been highlighted.

The optimization of a method for the continuous determination of soluble iron in ice cores and its application on the EGRIP ice core, provided the longest soluble iron profile from an ice core and it will be expanded in the next melting campaigns.

1.

Introduction

1.1 The Iron biogeochemical cycle

Iron is the fourth most abundant metal of the Earth's crust (4%) and it plays a crucial role in oceanic biogeochemistry. It is an enzymatic co-factor in those enzymes involved in the photosynthesis and in atmospheric nitrogen fixation (Mills et al., 2004). However, since its solubility in oxic environments and at pH > 4 is very low, iron bioavailability might limit Marine Primary Productivity (MPP) (Martin and Fitzwater, 1988). This is true in particular for the so-called High-Nutrient Low-Chlorophyll (HNLC) regions (Figure 1) which are characterized by high concentrations of major nutrients (e.g. nitrate and phosphate), but low MPP in terms of chlorophyll production. In light of this and to better assess the iron importance in those areas, different experiments have been realized. Several tons of acidified $FeSO_4 \cdot 7H_20$ were added to a 65-m deep surface mixed layer over an area of 50 km^2. The experiments confirmed that in HNLC regions, Fe^{2+} significantly enhanced the phytoplankton bloom and the biological respiration affecting the cycling of carbon, silica and Sulphur, leading to a considerable drawdown of surface CO_2 (Smetacek et al., 2012). HNLC regions constitutes up to the 20% of the world's oceans (Langmann et al., 2010) suggesting a crucial role that Fe have in promoting/limiting productivity.

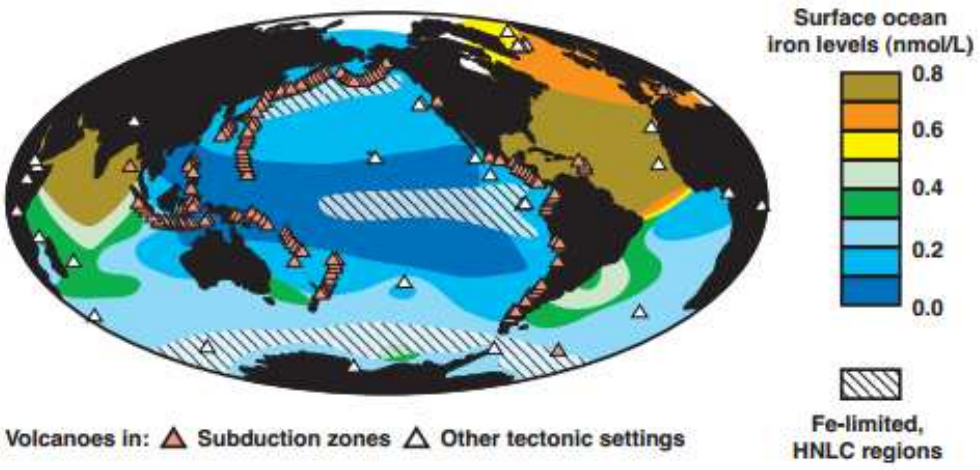

Figure 1 - Distribution of Fe-limited, HNLC regions (Duggen et al., 2010)

The main iron sources to the ocean are: 1) rivers, 2) hydrothermal vents, 3) aeolian mineral dust, 4) volcanic eruptions, 5) sediment release during diagenesis, 6) iceberg melting, 7) sea-ice melting, 8) anthropogenic sources (Jickells et al., 2005). The main source is represented by the fluvial input (625-962 Tg

Fe yr^{-1}). However only a small fraction is actually soluble in seawater. Indeed, because of the differences in ionic strength between rivers and seawater, most of the iron flocculates and precipitates in the estuarine environment. The actual dissolved Fe delivered by rivers is lower and of about 1.5 Tg Fe yr^{-1}. More details about the iron supply to the oceans are reported in Table 1. In the next sections, we will discuss more in details the atmospheric, the anthropogenic, the sea-ice, the iceberg and ice sheets melting and the volcanic contributions.

Table 1 - Flux of iron to the oceans (Jickells et al. 2005 and integrations)

Source	Flux (Tg Fe yr^{-1})
Fluvial particulate total iron	625-962
Fluvial dissolved iron	1.5
Glacial sediments	34-211
Atmospheric	16
	0.01-0.13[1]
Coastal erosion	8
Hydrotermal	14
Authigenic	5
Sea-ice melting	0.003[2]
Ice shelf melting	0.46- 2.71[3]
Anthropogenic sources	0.011[4]
Iceberg melting	0.06-0.12[5]

1.1.1 Atmospheric dust as the main source for Iron

The main aerosol sources are located in the Northern Hemisphere (Figure 2) and in particular in the so-called "Dust Belt" which comprises the arid regions of North Africa, the Arabian Peninsula, Central Asia, China, North America, South Africa and Australia. More often, the aerosol regions are basins located near mountain slopes. Dust production is linked to the availability of wind-erodible lands, which usually requires fluvial erosion followed by drying out and loss of vegetative protection.

[1] Raiswell R, Benning LG, Tranter M, Tulaczyk S. Bioavailable iron in the Southern Ocean: the significance of the iceberg conveyor belt. Geochemical transactions 2008; 9: 7. and it refers to the aeolian input of Fe in the Southern Ocean.
[2] Wang S, Bailey D, Lindsay K, Moore J, Holland M. Impact of sea ice on the marine iron cycle and phytoplankton productivity. 2014. and it refers to the sea-ice input of Fe in the Northern Hemisphere.
[3] Hawkings JR, Wadham JL, Tranter M, Raiswell R, Benning LG, Statham PJ, et al. Ice sheets as a significant source of highly reactive nanoparticulate iron to the oceans. Nature communications 2014; 5: 3929.
[4] Matsui H, Mahowald NM, Moteki N, Hamilton DS, Ohata S, Yoshida A, et al. Anthropogenic combustion iron as a complex climate forcer. Ibid. 2018; 9: 1593.
[5] Raiswell R, Benning LG, Tranter M, Tulaczyk S. Bioavailable iron in the Southern Ocean: the significance of the iceberg conveyor belt. Geochemical transactions 2008; 9: 7. and it refers to the Iceberg input of Fe in the Southern Ocean.

Iron content in mineral dust is highly variable (average: 3.5%) and it has low solubility (<1 to 2%) (Jickells et al., 2005). However, several factors might increase iron solubility. Among them:

- **aerosol size:** particles with a diameter < 2,5 μm show greater concentration of soluble iron than coarser particles (Baker and Croot, 2010);
- **aerosol pH** which is affected by the emission of acid precursors (SO_2 and NO_X) or organic compounds from both natural (terpenes from plants) and anthropogenic sources (biomass and fossil fuels burning). The increase in iron solubility due to high emissions of SO_2, promoted a phytoplanktonic bloom in the HNLC North East Pacific (Meskhidze et al., 2005);
- **photochemical processes** that involve iron species when the aerosol is scavenged by cloud or rain droplets during its transport, providing the right humidity and acidity to promote the photo-induced transformation (Zhuang et al., 1992);
- **the reaction between Fe(III) and I^-** that results in the production of Fe^{2+}_{aq} and I_2 species, under acidic conditions (pH ≤5). The mechanism involves a ligand to metal charge transfer (LMCT) followed by the dissolution of Fe^{2+}. I_3^- is originated from the disproportionation reaction $I_2^{\cdot} + I_2^{\cdot}$ (Kim et al., personal communication).

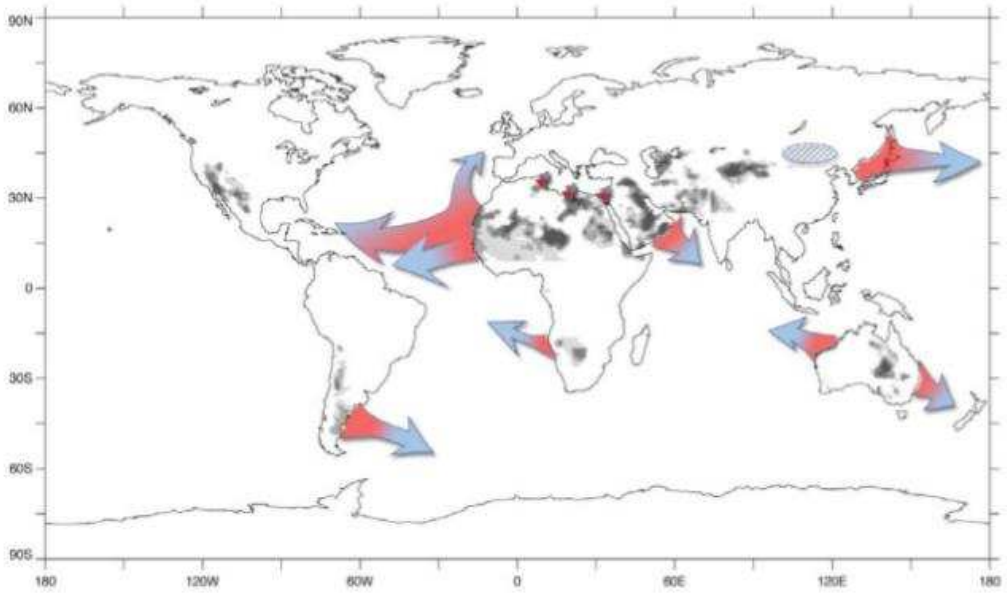

Figure 2 – Main dust sources and transport (Mahowald et al., 2007)

Human activities might influence the dust cycle since they introduce additional sources (e.g. agriculture) whose contribution, however, is still controversial. Some studies (Tegen et al., 2004) estimated that land use sources, in terms of dust contribution, can contribute less than 10% of the total source, while other calculations

(Mahowald et al., 2004) found that an increase in the range 0-50% of the land use source did not cause any significant increase in the overall dust flux. The relatively small impact of agricultural areas was also confirmed by other studies (Xuan and Sokolik, 2002). However, land use might have more regional impacts. The best, and most dramatic example, is represented by the Aral Sea, whose surface has decreased since 1971. The exposure of over 36.000 km^2 of the former seabed has significantly increased dust storm potential (Wiggs et al., 2003). Further studies are needed to better quantify the dust emissions due to anthropogenic perturbation of the hydrological cycle.

Under a human-induced global warming scenario, what will be the dust concentration into the atmosphere? Performing several model simulations, dust emissions will decrease between the 20% and the 60% in the next 80 years (Mahowald and Luo, 2003). This estimate is confirmed by observations that have reported a downward trend in dust transport from North Africa (one of the main aerosol source) to the Atlantic Ocean (Chiapello et al., 2005; Evan and Mukhopadhyay, 2010; Mahowald et al., 2007) since the 1980s. If this trend continues in the future, the decrease in mineral aerosols may have a great impact on the Earth's climate. In particular, it can lead to a decrease in the iron input into the ocean that can reduce the ocean productivity and, as a consequence, the capacity to capture the atmospheric CO_2. Three-dimensional models have shown that, on the one hand, there is only a small change in atmospheric CO_2 when the aeolian source is increased several fold, while, on the other hand, a reduction in the aeolian iron source might decrease significantly the atmospheric CO_2 drawdown to the ocean. This suggest that a warmer and wetter world will be also less dusty leading to an amplification of the ongoing increase in atmospheric CO_2 (Parekh et al., 2006).

1.1.3 Iron cycle in the ocean

Iron in the ocean is supplied mainly by the aeolian mineral dust. However, secondary sources are: 1) upwelling of iron-rich waters (Ross Sea); 2) glacial/iceberg melting; 3) seasonal sea-ice retreat; 4) hydrothermal activity; 5) volcanism (Baker and Croot, 2010). In seawater, Iron is involved in several enzymes such as the ones that participate in atmospheric N_2 fixation (Kustka et al., 2003) and might enhance MPP in the so-called HNLC regions (Martin and Fitzwater, 1988; Martin et al., 1990). To verify this hypothesis, several iron fertilization experiments (SOIREE, SOFeX) were performed in the biggest HNLC ocean of the Earth: the Southern Ocean. Tons of acidified and highly soluble $FeSO_4$ were injected into the Southern Ocean where a

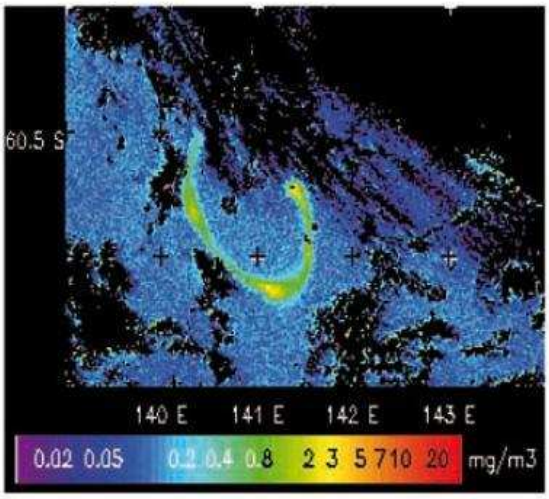

Figure 3 - NASA ocean colour over the Southern Ocean after the SOIREE experiment. It is possible to appreciate an increase in Chlorophyll-a concentration along the ship track

significant increase in MPP (Figure 3) and a drawdown of CO_2 were both recorded (Buesseler et al., 2005; Smetacek et al., 2012). Several scientists suggested to extend this experiment on a wider scale in order to enhance the biological pump (Vaughan and Lenton, 2011).

However, this geoengineering approach is not risk-free (Strong et al., 2009). Among the possible negative consequences, some studies done on halogens species along the ship's track (Wingenter et al., 2004), highlighted that seawater, which usually is a net sink for CH_3Br (the Southern Ocean represents 6% of the total global sink (Butler, 1994)), was no longer a sink for this gas. Methylbromide has a significant impact on stratospheric ozone depletion. This means that if large-scale iron fertilization experiments will be done in the Southern Ocean, an increase of about 0.5 ppt (Wingenter et al., 2004) in atmospheric CH_3Br would be expected. Since bromine is very effective in the radical ozone depletion reactions, this possible increase would delay its recovery by approximately one year (Wingenter et al., 2004).

In seawater, Iron has a typical nutrient profile: strongly depleted at the surface (0.05 nmol l^{-1}) and enriched (with a maximum around 0.7 nm l^{-1}) at 1000-1500 meters depth (Achterberg et al., 2001). However, coastal waters contain iron in higher concentrations because of the high riverine input (0.4-28 nmol l^{-1})(Achterberg et al., 2001).

Iron in seawater is differentiated between soluble iron (operationally defined as the Fe content after filtering at 0.2 μm) and particulate iron (0.45 μm) where the first prevails in the oligotrophic region of the central North Pacific, while the second prevails in coastal waters (Achterberg et al., 2001). Another important aspect for defining iron biogeochemistry in seawater is its speciation. Iron can exist in two oxidation states: Fe^{2+} and Fe^{3+} and they can form inorganic and insoluble complexes (such as $Fe(OH)_3$) or they might be organically complexed. Fe^{3+} is the dominant species in oxygenated waters and it tends to form insoluble compounds. The small fraction of soluble Fe^{3+}_{aq}, is mostly complexed by organic ligands increasing its solubility in seawater that is higher than the typical iron hydroxides solubility at the natural seawater pH (max solubility: 0.1 nmol l^{-1}) (Morel et al., 1993). To the contrary, Fe^{2+} is more soluble, thus bioavailable. However, Fe^{2+} is not thermodynamically stable in oxygenated environments such as surface seawater and it is rapidly oxidised.

Fe-binding ligands, that can increase Fe solubility and might decrease the oxidation rate of Fe^{2+} species (Rue and Bruland, 1997) can be divided into two categories (Boyd and Ellwood, 2010):

1) L_1, strong ligands: they are called siderophores and they are produced by bacteria in the upper ocean. They have a crucial role in keeping iron in its soluble, thus bioavailable form;

2) L_2, weak ligands: they are released during bacterial degradation of sinking particles in subsurface waters.

Only prokaryotes have shown to produce siderophores (Haygood et al., 1993), while eukaryotes used directly dissolved inorganic Fe^{3+} and they then reduce it through enzymes (Hudson and Morel, 1990).

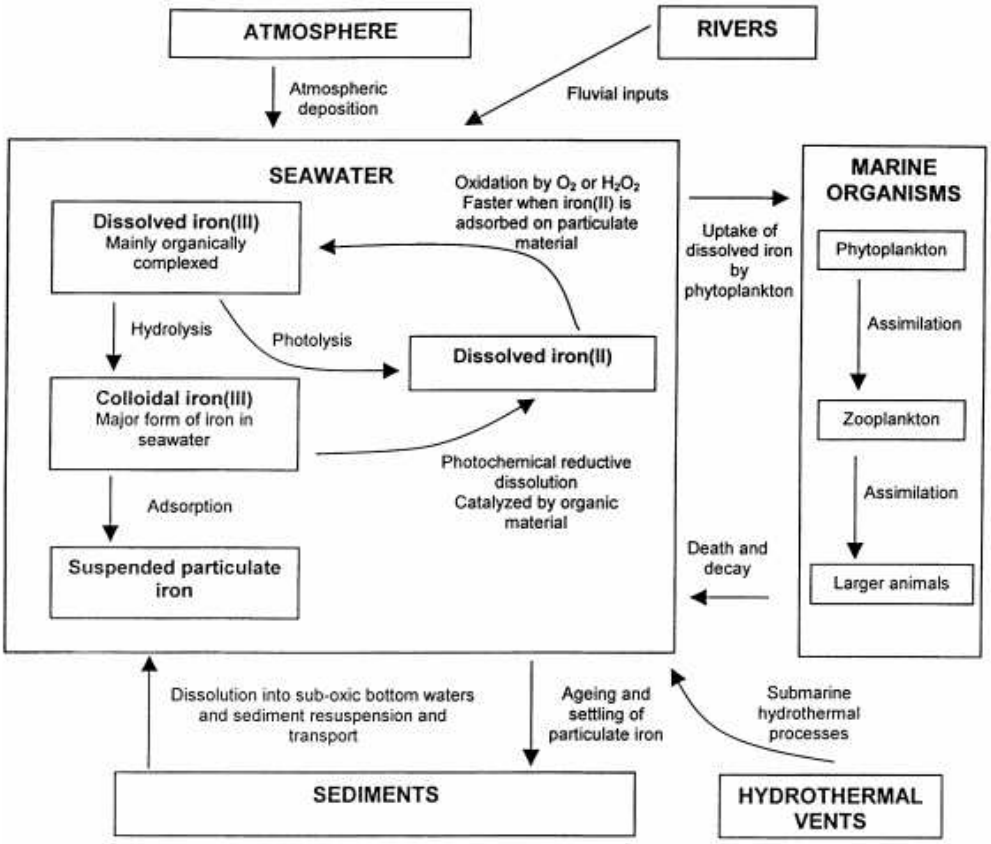

Figure 4 - Iron biogeochemical cycle in seawater (Achterberg et al., 2001).

Once dissolved in seawater, Fe undergoes several processes involving photochemical reductions, oxidation, photolysis and absorption on the sinking particulate matter (Figure 4). Dissolved iron is taken up by the phytoplankton that are then grazed by zooplankton and other larger animals of the food chain. Zooplankton can introduce Fe in seawater through fecal pellets playing a pivotal role in recycling it (Kirchman,

1996). When organisms die, Fe can be released in the seawater environment through remineralization processes. This process is also known as *the ferrous wheel* (Boyd and Ellwood, 2010; Kirchman, 1996).

The bottleneck for iron fertilization is its solubility in seawater after atmospheric deposition. As we previously mentioned, siderophores and other organic chelators help the solubilisation of iron keeping it in a dissolved form. Laboratory studies performed using Saharan dust, showed that while for other trace elements (e.g. Manganese), the dissolution was dependent upon the dust concentration, for iron the dissolution was dependent on the water's ligand complexing capacity (Mendez et al., 2010). This is a crucial aspect in the attempt to understand how past oceanic productivity could have been influenced by dust input. Indeed, if iron solubility in seawater is dependent on the concentration of organic ligands, marine productivity is limited by their concentration and it is not only dependent on the aeolian supply.

The ongoing increase of atmospheric CO_2 is leading to a progressive decrease in pH. This might might cause several consequences both on the phytoplankton and on the Fe chemistry. As previously mentioned, Fe is mainly present in the ocean as Fe^{3+} which is either chelated by organic compounds or it is present as highly insoluble Fe(III) hydroxides. With an increased ocean acidity, Fe speciation and solubility can change. Solubility will be enhanced for the insoluble Fe(III) species which will be more available for the phytoplankton. However, it was found (Shi et al., 2010) that, with the decrease of seawater pH from 8.2 to 7.7 (as expected by 2100), iron uptake by some diatom species might decrease by 20%, reducing, in turn, the biological carbon pump. This decrease in iron uptake may be linked with the increase in the binding constants between dissolved organic molecules and iron that will not allow Fe uptake by the phytoplankton. Also other factors should be taken into account. In particular, with a decrease in the pH, the reduction rates from Fe^{3+} to Fe^{2+} will likely increase, producing more bioavailable iron (Breitbarth et al., 2009). In the end, the overall effect of the ocean acidification on the iron bioavailability and on the biological carbon pump is unclear and needs more investigation. The effects of seawater acidification on iron speciation were observed in Canary Islands following the El Hierro submarine volcanic eruption. It was shown that submarine volcanic eruptions have the capacity to lower the seawater pH down to pH 6.5 (Fraile-Nuez et al., 2012; Santana-González et al., 2017). The low pH conditions favour the presence of higher amounts of iron in its reduced state and increase the solubility of Fe^{3+}, augmenting the amount available iron for the biological community potentially inducing a phytoplankton bloom (Mantas et al., 2011; Santana-Casiano et al., 2013).

1.1.4 Iron from ice melting

The role of iceberg melting in fertilizing the Southern Ocean by the delivery of terrigenous iron has been poorly investigated in the past. However, satellite measurements have highlighted a 5% increase in iceberg

calving from Antarctica (Rignot et al., 2011) in the last 20 years, especially from the West Antarctic Ice Sheet (Paolo et al., 2015) suggesting an increasing relevance for this phenomenon in fertilizing the Southern Ocean. Recent investigations (Duprat et al., 2016) have reported that melting of giant icebergs (horizontal length > 18 km) can release major nutrients together with trace elements into the ocean. In particular, after the passage of these icebergs, an increase in Marine Primary Productivity (MPP) has been reported which resulted in a CO_2 drawdown of up to 10% (0.012 – 0.040 Gt yr^{-1}) of the total Southern Ocean carbon export. The iron input in the Southern Ocean from iceberg melting, mainly as goethite (FeO(OH)) and ferrihydrite ($Fe_2O_3 \cdot 0.5\ H_2O$) is comparable (0.06-0.12 Tg yr^{-1}) with the aeolian dust contribution (0.01-0.13 Tg yr^{-1}) with the nanofraction more bioavailable than the macroscopic counterpart (Raiswell et al., 2008). The fertilization effects promoted by the icebergs vary significantly with respect to the origin of the icebergs themselves. Icebergs from the sector 0°-90°W have a greater impact in fertilizing the Southern Ocean because of their more easily weatherable metavolcanic rock composition (Duprat et al., 2016).

Iron fertilization promoted by iceberg melting (Figure 5a) can last more than 30 days (Figure 5b) and it is significant up to 300 km away from the source, peaking around 50-200 km.

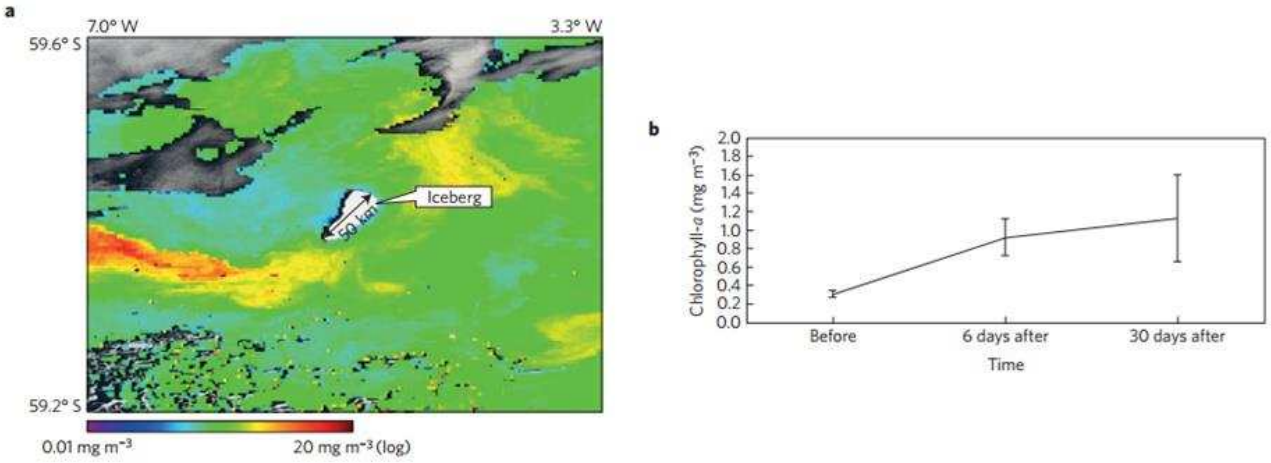

Figure 5 – a): chlorophyll-a concentration from the MODIS Aqua satellite. b): Mean chlorophyll level before and after the giant iceberg passage

If Antarctic ice sheet loss of 13.2 Gt yr^{-1} (Rignot et al., 2011) will continue for the next decades, the iron fertilization effect promoted by giant iceberg discharge will have the potential to enhance carbon export providing a new negative feedback loop to mitigate fossil fuel emissions (Raiswell et al., 2008).

Another similar and less exploited iron input into seawater, is the one from ice-sheet melting. Similarly to iceberg input, it can provide significant amount of iron in seawater in highly soluble form (e.g. goethite) and with fluxes that, at least in Greenland and in Antarctica, are comparable to the aeolian contribution. In particular ice-sheet melting provides 0.40-2.54 Tg Fe yr^{-1} in Greenland and 0.06-0.17 Tg Fe yr^{-1} in Antarctica

(Hawkings et al., 2014). Here again, under a global warming scenario, this might represent an important negative feedback through the enhancement of the biological carbon pump. This contribution might be more significant in the west Antarctic coastal margin which is considered iron limited and where annual blooms correlate with ice sheet melting (Frajka-Williams and Rhines, 2010). The same fertilization effect is not likely to be present in Greenland (Hopwood et al., 2015). Even though, the Greenland ice sheet input of iron is significant, the East Greenland Coastal Current acts as a natural barrier limiting the Fe export into the North Atlantic during summer. Thus, on the one hand global warming will increase the fluxes of Fe-enriched meltwater, on the other hand there will be no input into the Fe-limited waters of the North Atlantic and no significant impact on marine productivity.

1.1.5 Iron from sea-ice

Sea ice is considered one of the key components of the Earth's system and, therefore, it plays a crucial role in the climate evolution (de Vernal et al., 2013). In particular, having a very high albedo index (from 0.5 to 0.8) (McEvoy et al., 2003), it influences the energy budget at the surface of the Earth through the ice-albedo feedback. The high reflectivity of sea ice contrasts with the low albedo surface of the ocean (smaller than 0.1). During summer, sea ice reflects most of the incoming solar radiation and keeps the temperature relatively low in the Arctic. However, the continuous retreat of sea ice, whose surface has decreased from the last 30 years by 11% per decade (Kinnard et al., 2008), allows the low albedo ocean to absorb solar energy, increasing the summer heat content in the ocean mixed layer and delaying the ice formation in autumn and winter.

Several studies have reported that sea ice might also be an important iron reservoir, releasing it into surface water during spring and, together with increased light availability, boosting productivity (Lannunzel et al., 2007). If we exclude some regional exceptions where the main iron source to sea-ice is the aeolian mineral dust, the most of the iron found in sea-come comes from below, entrained into the mixed layer from deeper waters (Lannuzel et al., 2016).

When the sea-ice melts, it can deliver iron to surface waters in concentrations that are comparable to the major iron sources (e.g. dust, fluvial input). Considering that the global seasonal sea-ice area is about 22.5 million km2, it is quite easy to understand that sea-ice induced fertilization is a key factor in regulating MPP, especially in the HNLC regions (Kanna et al., 2014). Its contribution in terms of ocean fertilization potential is higher off-shore where the other fertilization sources (e.g. fluvial input, erosion, glacial melting) are less important (Gerringa et al., 2012). Sea-ice might induce fertilization also through the dissolution of coloured organic matter (CDOM) that can photo-reduce Fe^{3+} species into the more soluble and bioavailable Fe^{2+} species (Lannuzel et al., 2016).

Sea-ice is particularly vulnerable to climate change. Its retreat can have important consequences on the biological pump. With a decrease in seasonal sea-ice, there will be more light that can penetrate the upper ocean favouring phytoplankton blooms and growth (Arrigo et al., 2008). Arrigo et al., showed in their study that the annual primary production in the Arctic has increased by about 31 Tg C yr^{-1} from between 2003 to 2007. They attributed 30% of this increase to a decrease in the minimum summer ice extent and 70% to a longer phytoplankton growing season. This mechanism, at least in the Arctic, might increase MPP by up to 3 times than the 1998-2002 average. On the other hand, a decrease in sea-ice extent might reduce the Fe export from areas where it is more abundant (close to the coasts) to the off-shore HNLC areas. Consequently, with sea-ice melting the link between continental sources, and the off-shore HNLC region, where Fe is requires, would disappear (Lannunzel et al., 2016).

1.1.6 Iron from volcanic eruptions

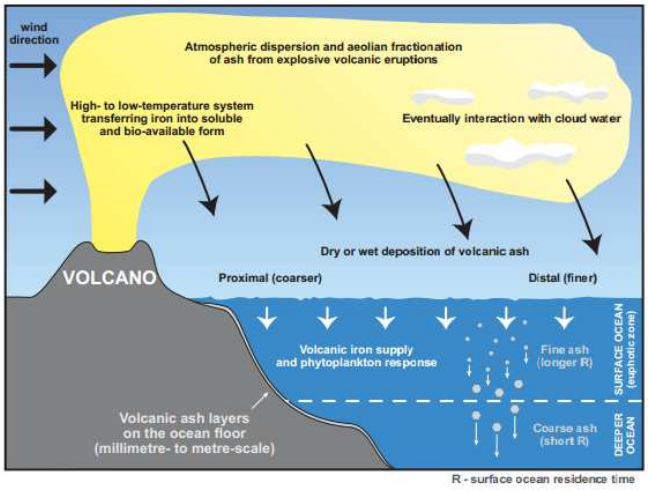

Figure 6 - Volcanoes might inject in the atmosphere significant amount of soluble iron that can trigger pythoplankton blooms in HNLC Area (From: Duggen et al., 2010)

Explosive volcanic eruptions have the potential to cool the Earth and affect the climate on annual to multiannual time scales through the injection of large quantities of gases and fine particles both into the troposphere and in the stratosphere (Oppenheimer, 2003). This can lead to a global increase in the Earth's albedo resulting in a decrease in average surface temperatures. To define the magnitude of a volcanic eruption, the Volcanic Explosivity Index (VEI) is commonly used (Newhall and Self, 1982). The VEI classifies volcanic eruptions through the volume of erupted tephra, and the eruption column height. Its values range from 0 (Hawaiian eruption) to 8 (Ultra-Plinian eruption). It has been reported that explosive eruptions (VEI > 6) have the capacity to cool the Earth's climate from between 0.2°C to 2.7°C for several years (Sigl et al., 2015; Zielinski, 2000). Ultra-Plinian eruptions, such as the Toba eruption (≈ 73 kya), could have affected the climate on a centennial time scale and could have even been involved in glaciation/deglaciation processes (Huybers and Langmuir, 2009; Williams, 2012). However, the mechanisms through which volcanoes affect climate are not fully understood, as they are limited to increases in planetary albedo.

Besides being an important source of radiatively active aerosol, it was suggested (Spirakis, 1991) that volcanoes could be a significant source of bioavailable Fe, potentially triggering phytoplanktonic blooms in the

so-called High Nutrient Low Chlorophyll (HNLC) regions (Figure 6). Volcanic ash typically contains highly soluble iron salts such as $FeCl_2$, $FeCl_3$, FeF_2, FeF_3 and $FeSO_4 \cdot 7H_2O$. These salts settle on the ocean surface after dry or wet deposition (Duggen et al., 2010). The first also involves the simple dissolution of iron once in contact with seawater, while the second one involves the interaction between the ash particle and cloud water before entering the ocean surface as rain. Typically, the amount of iron found in the erupted volcanic material is around 3% by weight. This means that 10^{10} g or more of Fe can be released into the ocean, depending on the magnitude of the volcanic eruption (Watson, 1997). This can increase the total dissolved iron (DFe) regionally in surface waters by up to 2 nM (Langmann et al., 2010; Rogan et al., 2016; Watson, 1997) potentially triggering a phytoplanktonic bloom in the above-mentioned HNLC areas where DFe concentrations are normally below 1 nM (de Baar, 2001). However, some laboratory experiments suggest that the phytoplanktonic response to the addition of volcanic ash is modest, suggesting that small amounts of Fe actually become bioavailable (Achterberg et al., 2013). This is probably due to other processes such as scavenging or the presence of organic ligands that can affect the solubility and biogeochemical cycling of iron from volcanic sources in the surface waters (Achterberg et al., 2013; Duggen et al., 2010).

The Spirakis' hypothesis of volcanically induced increases in Marine Primary Productivity (MPP) (Spirakis, 1991) has not yet been confirmed since the first reliable satellite images have become available. Only in recent years the link between volcanic eruptions and increase MPP could be documented in some HNLC regions. For instance, the Kasatochi eruption on the Aleutian Islands (August 2008) promoted an interesting phytoplanktonic bloom over the open NE Pacific (Langmann et al., 2010) where the MPP is typically low (chlorophyll concentration < 0,1 mg m^{-3}) (Iida and Saitoh, 2007). Using remote sensing techniques via the MODIS Aqua satellite, Langmann et al. detected an important increase in bioproductivity (average increase in chlorophyll concentration from 0.5 mg·m^{-3} to 1.0 mg·m^{-3}) in the open NE Pacific in the period that followed the volcanic event. The total amount of iron emitted by the volcano was in the order of $1 \cdot 10^8$ mol. If all of this was effectively used by the phytoplankton, up to 1.2 10^{14} g of C could have been removed from the atmosphere (Langmann et al., 2010). The same approach was used following one of the greatest volcanic eruption of the last 500 years in terms of tephra emissions (19,2 km^3): the Huaynaputina eruption in Peru (De Silva and Zielinski, 1998). In this framework, the iron fertilization effect promoted by the volcano could have explained the 10 ppm decrease in CO_2 recorded in Antarctic ice cores after 1600 (Langmann et al., 2010) More recently, a decrease in CO_2 concentration after the Agung and Pinatubo eruptions has been reported (Cather et al., 2009) that occurred in 1963 and 1991 respectively. Another important source of Fe^{2+} into the oceans is represented by submarine volcanoes that also have the capacity to reduce the seawater pH (Santana-González et al., 2017). The low pH conditions favour the presence of higher amounts of iron in its reduced state and increase the

solubility of Fe^{3+}, augmenting the amount of available iron for the biological community (Mantas et al., 2011; Santana-Casiano et al., 2013). However, the climatic impact of volcanic eruptions and their role on MPP is still under debate.

1.1.7 Anthropogenic iron emissions

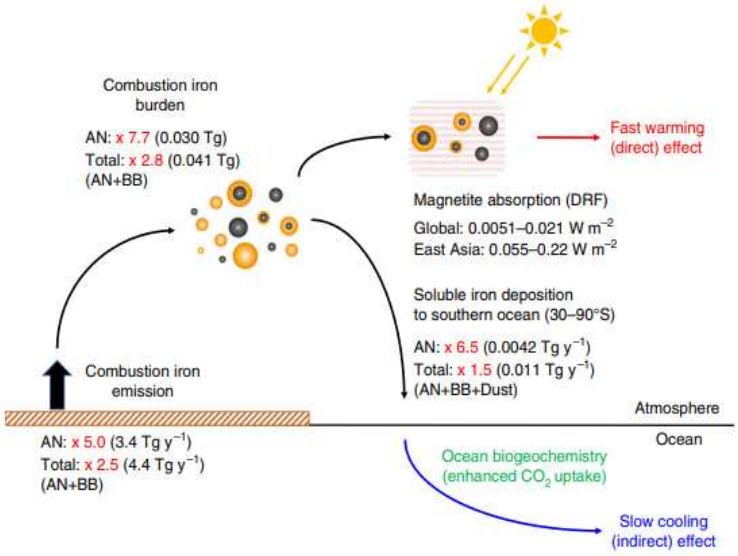

Figure 7 - The climate roles of Anthropogenic Iron (AN): details in the text. BB: biomass burning iron. From: Matsui et al., 2018.

Anthropogenic iron (AN iron) can be injected into the atmosphere following two main mechanisms: fossil fuel combustion and biomass burning (Sedwick et al., 2007). Even though the magnitude of these emissions is low compared with other sources (Table 1), combustion can provide iron in a higher soluble form. Different estimates suggest that combustion iron can contribute up to 40% of the soluble iron input in the HNLC regions (Matsui et al., 2018). AN iron solubility in the ocean is reported to be 7.7% (Matsui et al., 2018), which is higher compared with dust sources (4.0%).

Furthermore, combustion iron, in the form of magnetite, has a relevant role in absorbing shortwave radiation in the atmosphere with a direct radiative forcing comparable to that of brown carbon (Matsui et al., 2018; Moteki et al., 2017). This suggests a double role of AN iron on the Earth system: on the one hand, as stated above, it might act as a cooling factor because AN iron is more soluble than other sources and might fertilize the HNLC regions potentially cooling climate on a longer time scale. On the other hand, magnetite emissions might result globally in an increase of 0.0051-0.021 W m^{-2} of radiative forcing causing a fast (hours to weeks) and local (e.g. in megacities) warming of the atmosphere. The role of each of these components it is not still clear, especially because of the high uncertainty related to the magnetite fraction that might vary from between 20% to 80% and depends on the combustion sources (Sanderson et al., 2016).

1.2 Dust and iron in ice cores

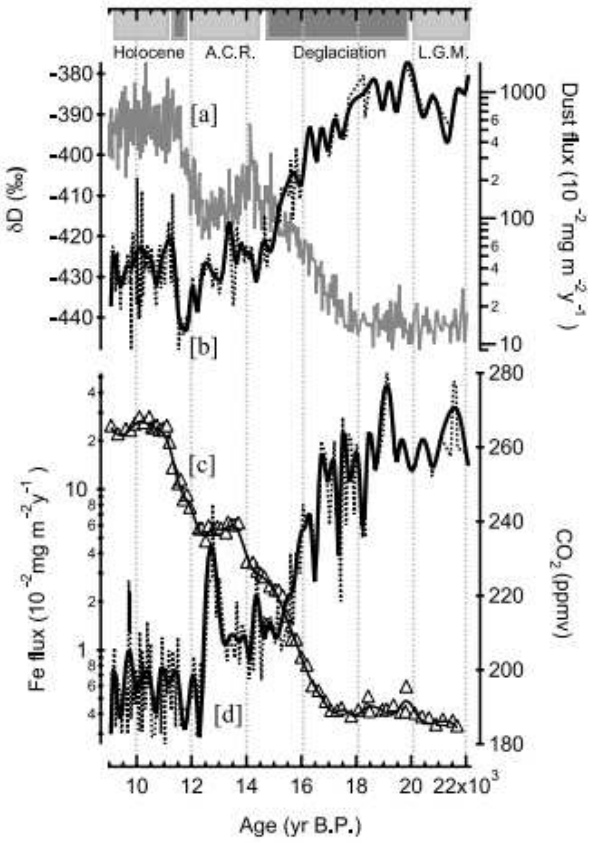

Figure 8 - EDC profile for temperature (a), dust flux (b), CO_2 concentration (c) and Fe flux (d). From: Gaspari et al.,2006

Ice cores provide a unique archive of the Earth's past climate. The oldest deep ice core ever drilled is the one collected during the European Project for Ice Coring in Antarctica (EPICA) that allows us to understand how climate has changed from 800 kyrs ago (Parrenin et al., 2007). The alternation between cold (glacial) and warm (interglacial) periods highlighted strong differences both in terms of temperature and in terms of dust fluxes (Lambert et al., 2008). Dust fluxes during the interglacials were ≈30 fold lower (≈0.4 mg m^{-2} yr^{-1}) than during glacial periods (≈ 12 mg m^{-2} yr^{-1}). The explanation relies on the decrease in vegetation, lower sea-level and increase in arid lands that were more exposed to wind erosion (Mahowald et al., 2005). Furthermore, since the lifetime of the particles in the atmosphere is constrained by wet deposition (Mahowald et al., 2006) and so by temperature and atmospheric water content, an atmospheric cooling of 5°C reduces the saturation vapour pressure by about one half. In other words, a cooler atmosphere holds less water vapour. This implies that the main dust scavenging process (i.e. wet deposition) is reduced, and both the particles lifetime and the dust flux are increased (Markle et al., 2018) .

An enhancement of the dust transport during glacial periods, together with a decrease in Southern Ocean ventilation and lower SST facilitating gas dissolution, might be an explanation of the lower glacial CO_2 concentration compared to interglacials (Martínez-Garcia et al., 2011; Sigman et al., 2010). As explained in the previous paragraphs, soluble iron supply from aeolian mineral dust might promote, in particular in the HNLC areas, a CO_2 drawdown from the atmosphere to the ocean. Unfortunately, Iron solubility is very low, thus, to assess its actual bioavailability total concentration values are not enough. Leachable iron experiments from the EDC ice core have been done (Gaspari et al., 2006) (24h digestion with HNO_3 at pH = 1) and it was found that soluble iron fluxes were ≈ $24 \cdot 10^{-2}$ mg Fe $m^{-2} \cdot yr^{-1}$ during the Last Glacial Maximum and ≈$0.7 \cdot 10^{-2}$ mg Fe $m^{-2} \cdot yr^{-1}$ at the beginning of the Holocene (Figure 8). The authors plotting the Fe flux vs CO_2 concentration appreciated that there was a high response in CO_2 concentration for small variation of Fe fluxes in low dusty periods. To

the contrary, a greater flux variation in high dusty periods, did not result into an appreciable variation in CO_2 concentration. This can be related to the fact that, actual Fe solubility is dependent on organic ligand concentration in seawater and that, after a certain threshold, the system did not respond to greater Fe concentration. In other words, Fe probably has a key role in starting a "feedback loop" that can cause warming or cooling, but it cannot explain all of the observed 90 ppmv amplitude of glacial-interglacial CO_2 change (Gaspari et al., 2006).

To understand further the possible Fe fertilization during glacial periods, it is important to perform Fe speciation studies since its biogeochemical properties depend on its oxidation state. Fe^{2+} species are, as stated above, more soluble and bioavailable (Shaked et al., 2005) than Fe^{3+} species (Baker and Croot, 2010). An insight on the iron speciation in an ice core was gained using an FIA-CRC-ICP-MS (Spolaor et al., 2013a). It highlighted that during the Last Glacial Maximum, Fe^{2+} concentrations in dust increased by up to seven times compared with average Holocene concentration (from 0.21 ng/g to 1.57 ng/g), while Fe^{3+} only doubled (from 0.59 ng/g to 1.23 ng/g).

1.3 Overview of the main analytical techniques to analyse Fe^{2+}

Performing Fe speciation in ice cores is an analytical challenge because of its very low concentration. High-resolution analytical techniques such as Continuous Flow Analysis (CFA) are the most suitable and frequently used (Kaufmann et al., 2008). In recent years, several methods have been set up, even though only one has been directly applied on ice cores: Fe speciation has been especially an oceanographic research topic and many methods were applied to quantify Fe^{2+} in seawater rather than in other matrices. A general overview about the main methods used are reported in Table 2.

1.3.1 ICP-MS speciation

ICP-MS is widely recognized as a powerful way to analyse inorganic elements at trace and ultra-trace levels in environmental matrices. The determination of ^{56}Fe (91,6% isotopic abundance) is difficult because of the presence of some interferences such as $^{40}Ar^{16}O^+$ and $^{40}Ca^{16}O^+$. These interfering species can be eliminated using a Collision Cell (CRC) with a constant helium stream. Since, an ICP itself is not able to perform any kind of speciation between the two Fe oxidation states, it is necessary to use a Ni-NTA Superflow resin before the injection of the sample into the ICP-MS (Spolaor et al., 2012) to quantify Fe^{2+}. In particular, the resin is able to retain Fe^{3+} completely at pH = 2 with no Fe^{2+} retention. Even though the method for Fe^{2+} quantification presents a low Limit of Detection (0.01 ng g^{-1}) and was able to quantify the Fe^{2+} concentration during glacial

Table 2 - Overview of the main analytical methods to detect Fe^{2+} species in different matrices. n.a. = not available

Method	LOD /ng·ml^{-1}	Dynamic Range	References	Matrix
ICP-MS	0.01	n.a.	(Spolaor et al., 2012)	Ice
Ferrozine	0.56	1.4 ng ml^{-1} – 16 µg ml^{-1}	(Pullin and Cabaniss, 2001)	Natural waters
	0.06	0.5 – 20 ng ml^{-1}	(Chan et al., 2016)	Aerosol
1-10 phenantroline	300	0.1 – 3 mg l^{-1}	(Kozak et al., 2010)	Natural water
Brilliant Sulfoflavine	0,02	0.02 – 0.56 ng ml^{-1}	(Elrod et al., 1991)	Seawater
Luminol	0,0007	0.0007 – 0.07 ng ml^{-1}	(Hansard and Landing, 2009)	Seawater
	0,0067	0.01 – 0.06 ng ml^{-1}	(Croot and Laan, 2002)	
	0,0022	0.002 – 0.56 ng ml^{-1}	(Bowie et al., 2002)	
	0,0002	0.0002 – 0.006 ng ml^{-1}	(Schallenberg et al., 2016)	

and interglacial periods from the Antarctic Talos Dome Ice Core (Spolaor et al., 2012), it does not allow a continuous determination of Fe species and it is not suitable for field measurements.

1.3.2 Spectrophometric techniques

Spectrophotometric techniques to quantify Fe^{2+} species involve different ligands that can selectively bind Fe^{2+} in order to produce a coloured complex that can be identified through a spectrophotometer. Quantification is possible thanks to the Lambert-Beer Law. It is known that organic molecules containing the ferroin group (–N=C-C=N-) might selectively bind ferrous ion in order to produce coloured complexes (Blau, 1898). One of the most promising is the disodium salt of 3-(2-pyridyl)-5,6-bis(4-phenylsulfonic acid)-1,2,4-triazine, also known as ferrozine (Pullin and Cabaniss, 2001; Stookey, 1970). When ferrozine selectively binds Fe^{2+} it produces a magenta-coloured complex that exhibits a maximum absorbance at 562 nm (molar absorbivity: 27900 M^{-1} cm^{-1}).

More recent attempts have been made on the quantification of Fe^{2+} in airborne particles using a 1-m long liquid waveguide capillary cell (LWCC) in order to reduce the detection limit of the method down to 0.06 ng/g (Chan et al., 2016; Majestic et al., 2006). This method exhibits a wide dynamic range (up to 10^4) and an excellent precision. Nevertheless, because of the long LWCC, this approach might led to important drawbacks in

particular related to the presence of bubbles inside the cell that can significantly disturb the analysis, to memory effects and low resolution for Continuous-Flow-analyses (Chan et al., 2016).

1,10 phenantroline is a reagent that presents, as ferrozine does, the ferroin group. When 1,10-phenantroline is added in a solution containing both Fe^{2+} and Fe^{3+}, it forms two complexes: one reddish complex with Fe^{2+} and one yellow complex with Fe^{3+}. The first absorbs at 512 nm, while the second at 380 nm (Harvey Jr et al., 1955) with a little absorption also at 512 nm. The molar absorbivity (11100 M^{-1} cm^{-1}) is lower than ferrozine, which means a detection limit of 0.3 mg l^{-1}.

1.3.2 Chemiluminescence techniques

Chemiluminescence (CL) techniques for the determination of Fe^{2+} are the ones that guarantee low LOD, high responsivity and no memory effect. The CL reaction between brilliant sulfoflavine, hydrogen peroxide and Fe^{2+} in a neutral medium was first used to detect Fe^{2+} in hydrothermal plume samples and gave a LOD of 0.45 nM (Elrod et al., 1991). The method proposed involved a pre-concentration of the sample on an ion-exchange column (8-hydroxyquinoline, 8-HQ). The method is quite sensible to interferences. In particular the authors found that Mn(II), Ni(II) and Cr(III) caused a slight suppression of the CL signal when present at 10 times the iron concentration. Cu(II) caused a significant enhancement of the signal when present at 10 times the iron concentration. However, if the abovementioned metals were present at concentrations similar to the Fe^{2+} one, the authors did not find any alteration of the CL signal given by Fe^{2+}. The calibration curves are linear if the peak area is used to quantify the detector response for two order of magnitudes.

Luminol is the other reagent commonly used to determine Fe^{2+} species (Rose and Waite, 2001). It is widely used in the oceanographic field (Hansard and Landing, 2009; Schallenberg et al., 2016) and on sea-ice (Lannuzel et al., 2006) with low detection limit (down to pg·g^{-1}), high sensitivity and no memory effects. The sensitivity of the method depends on the pH at which the luminol solution is buffered. It was found that pH = 10.3 (Seitz and Hercules, 1972) represents the best value to ensure the maximum sensitivity and at which the most favourite reaction is the one between Fe^{2+} species and the oxygen dissolved in the reagent. This reaction leads to the production of superoxide radicals that in turn oxidizes luminol to the excited α-hydroxy-hydroperoxide (α-HHP) species. It is the decomposition of the α-HHP that results into a blue light emission (λ = 425 nm). The signal, if correctly and frequently calibrated (Rose and Waite, 2001) is then proportional to the concentration of Fe^{2+} in the sample. Different authors reported linear (Croot and Laan, 2002; Hansard and Landing, 2009) and polynomial (King et al., 1995; Rose and Waite, 2001) calibration curves. This probably depends both on the sample matrix and on the calibration range. As brilliant sulfoflavine, also luminol exhibits

some interferences. Studies (Lannuzel et al., 2006) conducted spiking Co(II), Mn(II), Cu(II), Zn(II), Cr(III), Cd(II) and Ni (II) to Antarctic seawater with 2 nM Fe^{2+} showed interferences with Cu(II) because of the redox reaction with Fe^{2+} in which Cu(II) participates (eq. 1) and which results in a suppression of the signal:

$$Cu(II) + Fe^{2+} \rightarrow Cu(I) + Fe(III) \qquad \text{eq. 1}$$

The other species that can interfere is Co(II) that can lead to an overestimation of the signal if in concentration more than two times higher than Fe^{2+} species. However, it is unlikely that these species can interfere because their concentration in ice cores are either below or comparable to the Fe^{2+} ones (Barbante et al., 1997). To our knowledge, luminol has not been applied neither on snow nor on ice samples.

1.3.2.1 How luminol detection works?

The mechanisms involved into the CL reaction are still poorly understood, even though one reliable mechanism was proposed (Merényi et al., 1990; Rose and Waite, 2001). First, the reaction happens into a basic environment. This means that Luminol is present as an anion (LH^-). The first step is the luminol oxidation promoted by a primary oxidant which, in a Fe^{2+}-O_2 system, is OH. The luminol oxidation gives a luminol radical. The importance of OH in the formation of the luminol radical is proven by the fact that the addition of an $OH^{\cdot}$ scavenger (such as ethanol), decreases the chemiluminescence intensity at working pH of 10.3 (Pascual and Romay, 1992).

In a second step, the luminol radical can be oxidized into an α-hydroxy-hydroperoxide (α-HHP) by the radical superoxide. Because of the high pH (≈ 10) the α-HHP is present as an anion and it is very susceptible to the oxidation by $O_2^{\cdot -}$. The superoxide is produced both by the reaction of the luminol radical with O_2 and by the reaction between Fe^{2+} and O_2 (eq. 2, eq 3):

$$L^{\cdot -} + O_2 \rightarrow L + O_2^{\cdot -} \qquad \text{(eq. 2)}$$

$$Fe^{2+} + O_2 \rightarrow) + Fe(III) + O_2^{\cdot -} \qquad \text{(eq. 3)}$$

The latter reaction is directly connected to the working pH. In particular a second-order relationship between pH and the rate constant for Fe^{2+} oxidation by O_2 was found up to pH = 9. Other authors (King, 1998) suggested that over pH = 9, the rate constant still increase but with a smaller magnitude.

Only the decomposition of the monoanion results in excitation and subsequent light emission (λ = 425 nm). The α-HHP decomposition, and so the light emission, depends on the working pH. Seitz and Hercules (1972) highlighted that the efficiency of CL increasing up to pH = 10.5 because of the increased formation of the monoanion. After pH = 11, the quantum yield decreases.

In the following, we are going to summarize all the reactions (Figure 9):

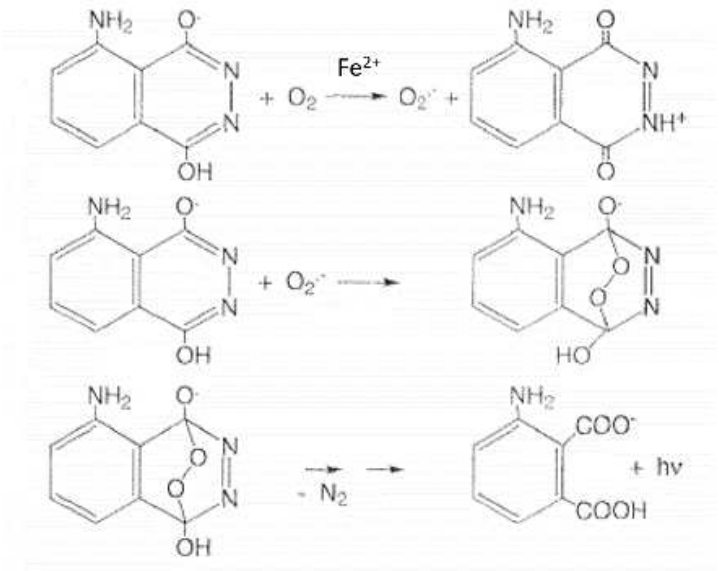

Figure 9 - Proposed mechanism of luminol oxidation Fe^{2+} and O_2 driven (From: Rose and Waite, 2001)

Luminol is found to be very photosensitive. Rose and Waite (2001) highlighted that when exposed to light, it started to produce a chemiluminescent signal without the presence of the sample. It is supposed that the exposure to light produces luminol radicals that can react with dissolved oxygen in the solution to produce superoxide, which in turn can oxidize other luminol radicals producing low levels of CL.

The effect of the organic matter on the complexation of Fe^{2+} and in turn on the chemiluminescence signal is still under debate: it may enhance (Saitoh et al., 1998), quench (Rose and Waite, 2001) or not have any effect (Hansard and Landing, 2009) on the CL signal.

The presence of organic ligands may help the free Fe^{2+} to form an organic complex (eq. 4):

$$Fe^{2+} + Org \rightarrow Fe^{2+}Org \qquad \text{(eq. 4)}$$

Even though some authors reported that this organically bound Fe^{2+} was not able to produce a CL signal (Seitz and Hercules, 1972), some strong evidences (Rose and Waite, 2001) suggest that Fe^{2+}Org might produce

superoxide and hydroxyl radicals but at a slower rate (100 M^{-1} s^{-1} vs 1 x 10^4 M^{-1} s^{-1}) than the one that involves inorganic Fe^{2+} (eq. 5):

$$Fe^{2+}Org + O_2 \rightarrow Fe^{3+}Org + O_2^{\cdot-} \quad \text{(eq. 5)}$$

The quenching effects are mainly related to:

- radical scavenging by organics *(marginal effect)*

$$Fe^{2+}Org + OH^{\cdot} \rightarrow Fe^{3+}Org + OH^- \quad \text{(eq. 6)}$$

$$Org + O_2^{\cdot-} \rightarrow Org_{ox} + O_2 \quad \text{(eq. 7)}$$

$$Org + OH^{\cdot} \rightarrow Org_{ox} + OH^- \quad \text{(eq. 8)}$$

$$Org + L^{\cdot-} \rightarrow LH^- + Org_{ox} \quad \text{(eq. 9)}$$

- CL light absorption (λ = 425 nm)
- Organic complexation of Iron *(main effect)*

The organic complexation of Iron is much faster than the reaction of inorganic Fe^{2+} with O_2 (1.2 x 10^5 $M^{-1}{\cdot}s^{-1}$ vs 1 x 10^4 $M^{-1}{\cdot}s^{-1}$). This means that, especially at high pH values, where the competition between protons and metals is in favour of the last ones, we may have an increase in the organic complexation of Fe^{2+}. Considering that, the production of superoxide and hydroxyl radicals that are necessary for the luminol CL signal from the organically complexed Fe^{2+} is very slow (see above), we record a decrease in the CL signal.

Nevertheless, if this it is true for some organic ligands (fulvic acids), it is not true for others. Hansard and Landing (2000) showed that there is no appreciable changing in the CL response if 50 pM or 500 pM of desferrioxamine B and protoporphyrin IX are added to a 50 pM Fe^{2+} solution. To the contrary, Saitoh et al., (1998) showed that citric acid acts as an activator of Fe^{2+} masking the Fe^{3+} present in the solution, while other ligands (e.g. Tiron and 1,10 phenantroline) quench the signal.

To sum up, the role of the organic matter is not fully understood and it depends on the working pH, on the nature of the organic ligands and, as a consequence, on the different rate constants of the reactions involved. Because of that, chemiluminescence should not be used when Dissolved Organic Matter (DOM) is present in high concentrations especially in freshwater samples (2-40 mg C/L) (Pullin and Cabaniss, 2001).

The analytical signal might also be influenced by the decrease in the pH. An increase in the response was immediately observed when an aged water sample was brought to pH 2 (Hansard and Landing, 2009). This

parameter has been carefully taken into account during the method development and it will be discuss in Chapter II.

In conclusion, the quantification of Fe^{2+} by luminol chemiluminescence represents the best compromise between low LOD and wide dynamic linear range. Even though there are other metals that can alter the chemiluminescence reaction (e.g. Cu(I), Mn(II) and V species), their concentration in ice cores are too low to cause significant interferences.

1.4 The aim of the thesis: iron speciation in ice cores, a new powerful tool to date and synchronize ice cores.

As highlighted in the previous paragraphs, Iron plays a key role in the biogeochemistry of the ocean since it can fertilize HNLC waters. Even though the fertilization effect between glacial and interglacial periods is supposed to be less than 40 ppmv in CO_2 concentration (Gaspari et al., 2006), understanding how Iron fluxes have changed during the last centuries or millennia is crucial to better assess its impact on marine communities and on climate.

Up to now, only few studies have been performed on iron speciation in ice cores. Traversi et al., 2004 first applied a total soluble iron method on discrete samples from Antarctica. Over the last 29 kyrs, concentrations varied from 1 $\mu g \cdot l^{-1}$ (bag mean) during the last glacial to 0.1 ug l^{-1} (bag mean) during the Holocene. It was also highlighted that the percentage of soluble Fe was around the 3% during the glacial period, maximum (64%) during the Antarctic Cold Reversal (from 11.6 kyrs to 14.2 kyrs) and around 34% during the Holocene.

Spolaor et al. (2012) applied for the first time the total soluble method on a CFA system for the analysis of a Greenland ice core (NEEM). They showed that in the period that spanned from between 1728 to 1733, total soluble Iron showed a seasonal profile (together with dust). Furthermore, they first reported a possible association between volcanic eruptions and spikes in total soluble iron.

Hiscock et al., 2013, performed the first comparison between an Antarctic and a Greenland Ice Core using the total soluble iron method coupled to a CFA system. During the Holocene, iron mean values in Antarctica (50 pg g^{-1}) were 0.33 times the ones detected in Greenland (150 pg g^{-1}). During glacial times the difference between the two locations was even more pronounced, with Antarctic mean values (80 pg g^{-1}) being 0.2 times the ones of Greenland (400 pg g^{-1}). The Last Glacial Maximum (LGM) was the period when the highest concentration of total soluble iron were detected (130 pg g^{-1} in Antarctica).

The first quantification of Fe^{2+} species in ice core has been performed on an Antarctic sample covering the last 50 years (Spolaor et al., 2012). The study showed a 5-fold increase in soluble Fe^{2+} species from the interglacial to the glacial period.

Up to now, if we consider all the available CFA data avoiding the low-resolution discrete samples, only 65 meters of both Antarctic (14 meters) and Greenland (51 meters) ice cores have been analysed for total soluble iron. Regarding Fe^{2+}, 32 discrete samples (covering 32 meters in the last 50 kyrs) have been analysed. However, no continuous data are available.

In this context, the main goal of this thesis was to validate and optimize two continuous flow analysis and discrete methods for the determination of soluble iron and soluble Fe^{2+} in ice and snow matrices (Chapter II). We then applied the methods on different ice cores (Dome C, Holtedalhfonna, B17 and EGRIP) enlarging significantly the amount of Fe data available in different environments (Table 3).

*Table 3 - Summary of all the new available data for Fe^{2+} and Total Soluble Iron. *--> data not already processed*

	Antarctica	**Svalbard Islands**	**Greenland**
Fe^{2+}	2.95 m (Dome C)	10 m (HDF)	*218 m (EGRIP)**
			15 m (B17)
Total Soluble Fe	-	-	280 m (EGRIP)
			15 m (B17)

During the analysis of the B17 ice core, I demonstrated how the Fe^{2+} quantification was particularly useful in order to detect past volcanic eruptions. Up to now, volcanic eruption horizons have been quantified through the detection of sulphates. However, the methods commonly used for this purpose coupled with a Continuous Flow Analysis system struggle to achieve the limit of detection and the resolution needed for deep polar ice cores. The innovative approach presented in this thesis might overcome these limitations and it demonstrated its reliability for past volcanic eruptions detection in a Greenland ice core and in an Antarctic snow pit (Chapter III).

Furthermore, the transport and post-depositional mechanisms that might affect Fe^{2+} species were investigated using an Antarctic and a Svalbard sample (Chapter IV)

The results obtained during my PhD represent a starting point for future research in this field, in particular addressing key questions such as the possible fertilization role that volcanic eruptions might have in the HNLC

areas. The setup of a reliable analytical method for the determination of Fe^{2+} and soluble Iron, together with the optimization of a soluble Al method, might be applied for ice older than 400 kyrs (i.e. EPICA Oldest Ice project) where volcanic layers are not detectable using the traditional sulphate methods (Chapter V).

Appendix A is devoted to the presentation of continuous total soluble Fe data from EGRIP covering approximately the time interval from the 1st century B.C. to the mid 17th century. For selected time intervals, where strong volcanic eruptions happened, the Fe^{2+} profile is reported as well.

2.

Material and methods

The author has previously published part of the work described in this chapter in:

Burgay, François, et al. "Fe^{2+} in ice cores as a new potential proxy to detect past volcanic eruptions." *Science of The Total Environment* (2018)

2. Material and methods

2.1 Sampling sites

Ice cores and snow samples for this PhD thesis were collected in Svalbard (Holtedahlfonna glacier), in Greenland (B17 and EGRIP) and in Antarctica (Dome C). These sites were selected because of their different features. The main differences among them are related to different Fe concentrations. The Holtedahlfonna glacier is the one with the highest Fe concentration and it was chosen for preliminary tests with discrete samples and to look at possible factors that can enhance or reduce Fe solubility. Once optimized, the method for discrete analyses was tested on two Greenland ice cores with similar Fe concentrations. In the end, we decided to test the method for discrete analyses on a snow pit collected at Dome C to evaluate if the method was suitable for the detection of past volcanic eruption also in a site with low accumulation and lower Fe concentrations.

Figure 10 - Location of the Holtedahlfonna glacier in the Sbalvard Archipelago

Holtedahlfonnna (2017)

One of the objectives of the Iron Speciation in Svalbard Ice Core and Snow (ISSICOS) project was to drill a shallow core on the Holtedahlfonna glacier (Figure 10; 79°8 'N; 13°16' E; 1150 m a.s.l.). The Holtedahlfonna has an extension of 300 km^2 and it is located 40 km north-east from Ny-Alesund (Figure 10; Figure 11). To reach the desired depth, we performed 17 drill runs with an average length of 44 cm (Figure 12). Each piece of ice was logged, recording its length and its density. The ice core was brought back to Ny-Alesund and stored in a freezer facility for one week. We processed and decontaminated the ice core outdoor close to the Gruvebadet station wich represents the cleanest location close to Ny-Alesund (Figure 13) The researchers wore Tyvex coveralls and polyethylene gloves over their anorak. The chosen resolution was 5 cm, sufficient to resolve the seasonal cycle. Each sample was subsampled: the outer part was used for isotopic analysis, while the inner and not contaminated one, was used for the chemical analysis (Iron speciation, Halogens). Discrete ice core samples were then shipped to Italy in an insulated box. Samples were melted using a 80°C warm water bath, subsampled for halogens and immediately analysed for Iron(II) under a laminar flow-hood class 100.

Figure 11 - The Holtedahlfonna glacier

Figure 12 - A typical ice core collected during the drilling campaign at the Holtedahlfonna. Ice lenses are visible suggesting that melting occurs

Figure 13 - Ice core processing in Gruvebadet

Figure 14 - Location of the two drilling sites in Greenland: B17 and EGRIP

B17 (1993)

The 100.8 meter long B17 ice core was recovered in the framework of the North Greenland Traverse (NGT) carried out by the Alfred-Wegener-Institute for Polar and Marine Research, Bremerhaven, in 1993 at 2820 m. a.s.l. (Figure 14; 75°25° N; 37°63 W; 2820 m. a.s.l.).

EGRIP (2017)

The East Greenland Ice-core Project, EastGRIP (Figure 14, 75°38 N; 36°00 W; 2720 m. a.s.l.) is an ongoing project with the aim to drill a 2.5 km long ice core in order investigate how ice streams will contribute to future sea-level change. The core will also provide an impurity record of the last 25.000 years from the end of the last ice period until present day. The project is financed by 12 countries: Denmark, US, Germany, Norway, France, Japan, Switzerland, China, Iceland, Italy, Sweden and South Korea. In

February-March 2018 the first 350 meters were melted covering approximately the last 3000 years of the Earth's climatic history. The drilling activities will end in 2020.

Dome C (2014)

A 2.975 meters-deep snow pit was dug 2 km far from the Concordia Station in Dome C (Figure 15; 75° 06′ S, longitude 123° 21′ E; 3233 m a.s.l.). Sampling was done using pre-conditioned 2.5 cm diameter polyethylene (PE) vials. The vials were pushed into the snowpit wall one below the other along a vertical line with a resolution of 2.5 cm. Snowpit samples were shipped to Italy in a freezer at -20°C. Samples were melted using a 80°C warm water bath and immediately analysed for Iron (II) under a laminar flow-hood class 100.

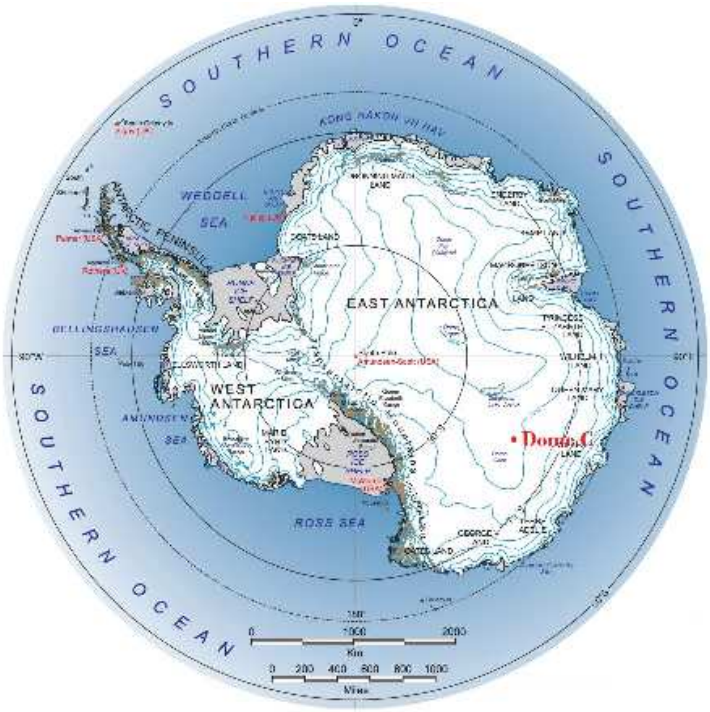

Figure 15 - Antarctica and the Dome C sampling site

Table 4 summarizes all the main features of the sampling sites.

Table 4 - Sampling site features

Sampling Site	Latitude	Longitude	Altitude	Accumulation rate	Depth
Holtedahlfonna	79°08 N	13°16 E	1150 m. a.s.l.	0.50 m we yr^{-1}	9.47 m
B17	75°25 N	37°63 W	2820 m. a.s.l.	0.12 m we yr^{-1}	100.8 m
EGRIP	75°38 N	36°00 W	2720 m. a.s.l.	0.11 m we yr^{-1}	350.9 m
Dome C	75°06 S	123°21 E	3233 m. a.s.l.	0.03 me yr^{-1}	2.98 m

2.2 Cleaning pocedures

All the plastic material used for analyses (HDPE Amber bottles, Nalgene Corp., USA) was washed for 5 days in a soap bath (Citronox©), rinsed 5 times using UWP water, then filled with Suprapure HNO_3 (Romil,

Cambridge, UK) 3% for 1 week. Then it was rinsed again 5 times with UWP water and then filled with Ultrapure HNO_3 (Romil, Cambridge, UK) 1% for 1 week. Finally, it was rinsed 5 times with UWP water and filled with Ultrapure HNO_3 0.1% (Romil, Cambridge, UK) until the planned analyses.

All the tubing system was washed with a 2% Suprapure HNO_3 (Romil, Cambridge, UK) solution before and after every analytical session and between two runs in order to limit memory effects.

Standards were prepared under a class-100 laminar flow hood.

2.3 Iron (II)

The CL induced by the reaction among luminol, O_2 and Fe^{2+} has been widely used in oceanography (Rose and Waite, 2001; Hansard and Landing, 2006; Schallenberg et al., 2016 and references therein) and on sea-ice (Lannunzel et al., 2006) with low detection limit (< 10 $pg \cdot g^{-1}$), high sensitivity and no memory effects. The sensitivity of the method depends on the pH at which the luminol solution is buffered. Seitz and Hercules (1972), found that pH = 10.3 represents the best value to ensure the maximum sensitivity and at which the reaction between Fe^{2+} species and the oxygen dissolved in the reagent is favoured. This reaction leads to the production of superoxide radicals that in turn oxidizes luminol to the excited α-hydroxy-hydroperoxide (α-HHP) species. It is the decomposition of the α-HHP that results in a blue light emission corresponding to λ_{max} = 425 nm. The recorded signal is proportional to the concentration of Fe^{2+} in the sample. Different authors reported linear (Croot and Laan, 2002; Hansard and Landing, 2006) and polynomial (King et al., 1995; Rose and Waite, 2001) calibration curves. This probably depends both on the sample matrix and on the calibration range.

Luminol might exhibit some interferences. Studies (Lannunzel et al., 2006) conducted spiking Co(II), Mn(II), Cu(II), Zn(II), Cr(III), Cd(II) and Ni (II) to Antarctic seawater with 2 nM Fe^{2+} showed interferences with Cu(II). The reason likely is because Cu(II) participates in the redox reaction with Fe^{2+} which results in a suppression of the signal (Gonzalez et al., 2016).

The other species that can interfere is Co(II) that can lead to an overestimation of the signal if in concentration more than two times higher than Fe^{2+} species. However, it is unlikely that this species can interfere because its concentration in ice cores is either below or comparable to the Fe^{2+} ones. For instance, Cobalt concentration in the Summit ice core (Greenland, Barbante et al., 1997) ranges from 0.65 $pg \cdot g^{-1}$ to 15.5 $pg \cdot g^{-1}$ (average value 5.8 $pg \cdot g^{-1}$).

2.3.1 Fe^{2+} - Reagents and standards

Fe^{2+} carrier: HCl 0.001 M was prepared diluting 50 µl of 37% HCl (ACS reagent, Sigma Aldrich) in 500 ml Ultra Pure Water (UPW) water (lifetime: 9.6 h)

Luminol solution: dissolution of 0.178 g of Luminol (Sigma Aldrich) in 1 M NH_3 solution (73 ml of Ammonium Hydroxide Solution (TraceSELECT™, Honeywell Fluka) in 1 L of UWP water, lifetime: 9.6 h). The solution was stirred for 60 seconds and then stored for 12/24 h to ensure complete dissolution. After that, the pH was adjust to 10.3 with the addition of 10-15 ml of HCl (ACS reagent, Sigma Aldrich). To enhance sensitivity, the solution was ultrasonicated for 30' (Greenway et al., 2006) and then cooled to room temperature. Because luminol is light-sensitive (Rose and Waite, 2001), the solution was stored in amber HDPE bottles and all tubing was shielded from light. The luminol solution was prepared at least 2 days before the analytical session, in order to be sure that it was all in the dissolved form.

Fe^{2+} standards: a standard stock solution was prepared by dissolving 0.3921 g of ammonium iron(II) sulphate hexahydrate (Honeywell Fluka) in a 100 ml 0.1 M HCl solution. This solution was stable up to one month (Hansard and Landing, 2006). One intermediate (50 µM) and one working solution (250 nM) are prepared daily by dilution of the stock solution and acidified with 300 µl HCL 37% (ACS reagent, Sigma Aldrich). The calibration (see following) was made with the standard addition method.

No reagent purification procedure was performed.

2.3.2 Fe^{2+} – Instrumental setup

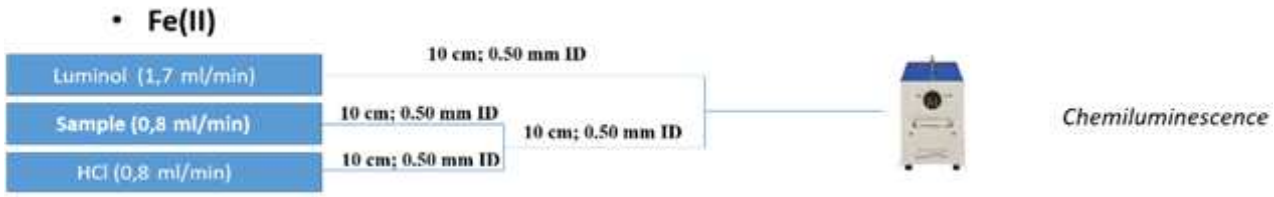

Figure 16 - Instrumental setup of the Fe^{2+} method. Tubing lenght was optimized to minimize back-pressure issues

Figure 17 - Homemade spiral flow cell for CL measurements

Tygon pump tubing and 1/16" PTFE Tubing (Figure 16) and high-pressure fittings were used to transport reagents and samples to the detectors via an 8-channel peristaltic pump (Ismatech, Germany) at a rate of 27 rpm. Flow rates and the length of PTFE Tubing are optimized to minimize backpressure issues. For the luminol detection, we used a home-made spiral flow cell made of 25 cm PTFE Tubing (Figure 17; 1/16", 0.75 mm ID, VICI, USA) put in front of a

photomultiplier (SensTech, USA) completely shielded from light. All data were acquired every second using the Sens-Tech Counter Timer 2.8 software (Sens-Tech Ltd, USA).

2.4 Total Soluble Iron method

The total soluble iron method relies on the catalytic oxidation of the N,N-dimethyl-p-phenylenediamine dihydrochloride (DPD, colourless) to the semiquinonic form (DPDQ, pink) driven by Fe^{3+} species (Hiscock et al., 2013; Spolaor et al., 2012). H_2O_2 is added to the reaction oxidizing both the Fe^{2+} originally present in the sample and the reduced one after the reaction with the DPD in order to regenerate Fe^{3+} to conclude the redox cycle (Traversi et al., 2004). The quantification of total soluble iron is possible by monitoring absorption at 514 nm where DPDQ shows a maximum of absorption (Measures et al., 1995).

2.4.1 Total soluble Iron – Reagent

Total soluble Fe carrier: HCl 0.2 M prepared diluting 2 ml of 37% HCl (ACS reagent, Sigma Aldrich, USA) in 100 ml UWP water (lifetime: 15 h)

DPD solution: dissolution of 1.28 g (0.03 M) of DPD (Sigma Aldrich, USA) in 100 ml of UWP water (lifetime: 15 h) where 0.07 g of Na_2SO_3 (Sigma Aldrich) were previously added. Na_2SO_3 acts as an oxygen scavenger and helps preserving the DPD that easily oxidizes when in contact with air (Hiscock et al., 2013).

DPD Buffer: prepared by dilution of 150 ml of acetic acid (HAc, ACS reagent, Honeywell Fluka) and 210 ml of ammonium hydroxide solution (TraceSELECT™, Honeywell Fluka) in 500 ml of UWP water (lifetime: 26.8 h). The final pH was adjusted with small additions either of HAc or of NH_3. To avoid interferences with copper, 10 µl of triethylenetetramine (Sigma Aldrich) are added (Measures et al., 1995). 5 ml of Brij L23 (Sigma Aldrich) are also added. We found that increasing the concentration of Brij L23 helps in microbubble prevention. In particular, the use of this surfactant prevents that bubbles get stuck in the flow cell. The drawback is an increase of the baseline because of the impurities contained in the Brij L23.

H_2O_2 5%: prepared by dilution of 82 ml of H_2O_2 (Sigma Aldrich) in 500 ml of UWP water (lifetime: 13.4 h). Even though it was reported (Spolaor et al., 2012) that a higher H_2O_2 concentration increased sensitivity, we found a greater production of microbubbles that may affect and disturb the signal.

Fe^{3+} standards: are prepared by diluting the ICP-MS standard 1000 ppm (Merck) to a 1 ppm working solution. Working standards are prepared at 0.5 ng g^{-1}, 1 ng $g^{-1}$and 1.5 ng g^{-1}.

No reagent purification procedure was performed.

2.4.2 Total soluble Iron – Instrumental setup

Figure 18 - Total Iron instrumental setup

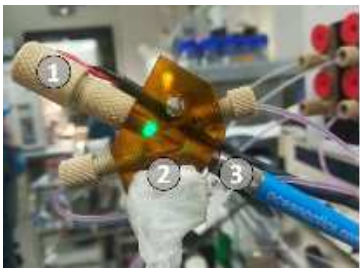

1) LED (525 nm)
2) Z-Cell (ULTEM)
3) Fiber optics connected to the T-FLAME spectrometer

Figure 19 - Detection cell for the Total Soluble Iron method

Tygon pump tubing and 1/16" PTFE Tubing (Figure 16) and high-pressure fittings were used to transport reagents and samples to the detectors via an 8-channel peristaltic pump (Ismatech, Germany) at a rate of 27 rpm. Flow rates and the length of PTFE Tubing are optimized to minimize backpressure issues. Absorption was measured at 514 nm in a 10 mm path length microvolume flow cell (Z-cell) (Figure 19; SMA-Z-microV-10, FIAlab instruments, USA) irradiated by a 525 nm LED light source (Roithner Laserchnik GMbH, Austria). The flow that reaches the cell is 1 ml·min^{-1}. This ensures a higher stability of the signal. An important upgrade compared with the previous applications, was the introduction of a vacuum degasser (Systec, IDEX, USA) just before the Z-cell. We obtained a greater stability of the signal and negligible microbubble formation. The choice of a transparent Z-cell is crucial because in that way it is possible to control microbubbles formation that can affect the results. The detector was a T-FLAME Spectrophotometer (Ocean Optics, USA) with an integration time from 6000 μs to 200000 μs. The integration time was kept constant during one complete analytical session (1 day), but it might change from one day to the other. All data were acquired every second using the OceanView software (Ocean Optics, USA).

2.5 Coupling with the CFA-system

Continuous Flow Analysis (CFA) is a technique commonly used to analyse inorganic elements in ice cores at a higher resolution than discrete sampling techniques. Furthermore, this analytical approach excludes external laboratory contamination since the sample does not enter in contact with any external source except the melthead. The internal section of the ice is used to perform impurity analyses, while the external section, more susceptible to contaminations, is generally used for stable water isotope analyses.

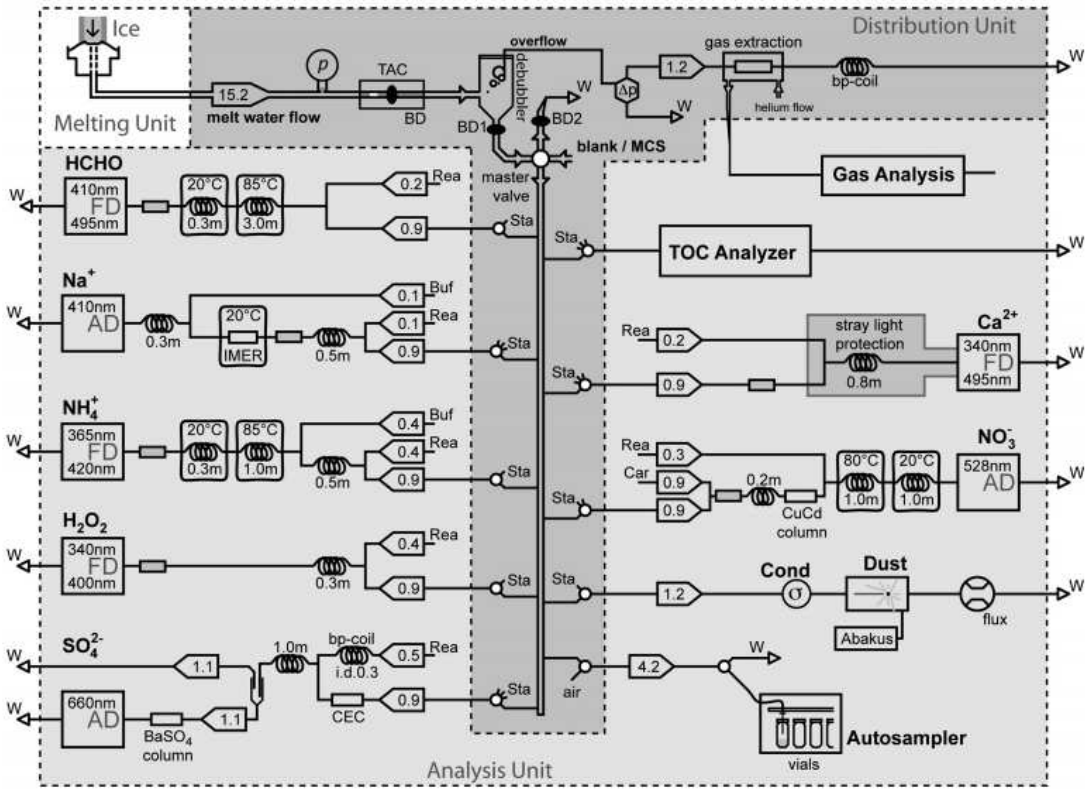

Figure 20 - The Bern Continous Flow Analysis system: schematic view (Kaufmann et al., 2008)

Both the Fe^{2+} and total soluble Iron method were developed in the laboratories of the Ca' Foscari University of Venice. Both methods were coupled with the Bern-CFA system (Figure 20, Figure 21, Figure 22; Kaufmann et al., 2008) which routinely measures dust (Abakus Klotz, Germany), conductivity and major ions such as Na^+, Ca^{2+}, NH_4^+, NO_3^-, SO_4^{2-} and H_2O_2 with different spectrophotometric techniques (absorption and fluorescence).

Figure 21 - The Bern CFA system: real view

The Bern system also provides a melted ice water stream to the Inductively Coupled Plasma Time Of Flight Mass Spectrometer (ICP-TOF-MS) and to an autosampler for discrete anion measurements. The melting unit is contained in a freezer at -20°C at the University of Bern (Figure 22) where ice cores are processed and cut (cross section 32x32 mm).

1) Melthead
2) Table to process and cut ice cores
3) CFA system

Figure 22 - The freezer where ice cores where cut and melted

The melthead is made in copper and coated by gold (Figure 23). Its temperature is regulated in order to control the melting speed. For the B17 ice core the meltspeed varied from 3.4 $cm \cdot min^{-1}$ for the upper part, to 2.8 $cm \cdot min^{-1}$ for the deepest part (Table 5). For EGRIP, the meltspeed was kept constant at 3.0 $cm \cdot min^{-1}$ for all the depths.

Depth top /m	**Meltspeed /cm·min^{-1}**	**Chronology /years**
32.0-35.0	3.4	1851-1833
36.0-38.0	3.3	1827-1814
39.0-45.0	3.2	1809-1771
68.0-70.0	2.8	1611-1596

Table 5 - Analyzed sections, meltspeed and chronology for the B17 ice core.

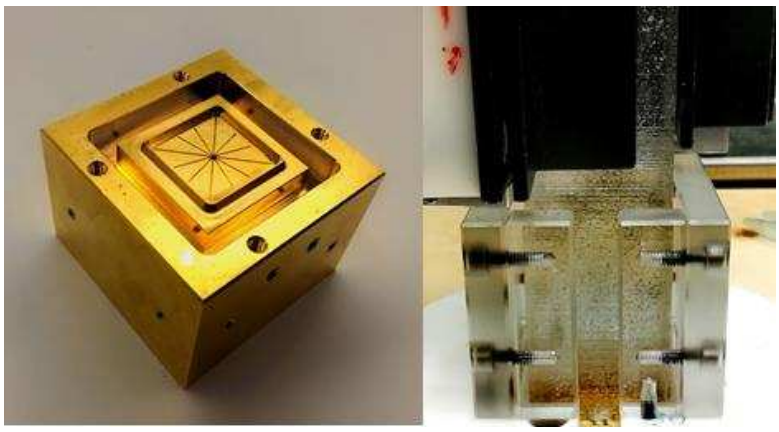

Figure 23 - Left: the melthead used for the analysis. Right: the ice core when it is melted

2.6 Soluble Aluminium method

An optimization of a soluble aluminium method (Spolaor et al., 2013b), for an application on the Dome C snow pit was also performed. Aluminium is the most abundant crustal element and can give us information about dust transport and deposition. In ice and snow matrices it is commonly determined by ICP-MS. However, especially in the oceanographic field (Obata et al., 2000), soluble Aluminium has been detected using fluorescence techniques that involve the formation of the Al-lumogallion complex (Hydes and Liss, 1976) particularly enhanced at 70°C. The fluorescent signal was enhanced adding a surfactant such as Brij-L25. The excitation wavelength was 490 nm, while the emission wavelength was 550 nm.

It was reported that significant increases in soluble Aluminium concentration could be also linked to volcanic eruptions (Gabrielli et al., 2008; Spolaor et al., 2013b).

2.6.1 Analytical set-up

As mentioned above, the determination of soluble Al relies on the formation of the fluorescent compound Al-lumogallion (4-chloro-6-[(2,4-dihydroxyphenyl)azo]-1-hydroxybenzene-2-sulfonic acid) that, excited at 490 nm, it emits light at 550 nm. Since the formation of this complex has a slow kinetic, a long reaction coil (10 meters in total) and heating at 70°C are necessary to accelerate the reaction.

The sample flow of 0.65 ml·min^{-1} is mixed with 0.01 M HCl. The mixture is then combined with lumogallion buffer in an 8 m reaction coil heated at 70°C. A diluted (5%) solution of Brij-L23 is added subsequently and all the solution is cooled to room temperature in a 2 meters long reaction coil. Brij-L25 is necessary to preserve and maximize the fluorescence emission.

A fluorescence flow cell (internal volume: 8 µl) is put in front of a photomultiplier. Light is acquired with an integration time of 1 second. An excitation and an emission filter are used to avoid light interferences.

Figure 24 - Analytical set-up for the soluble Al method

2.7 Total Iron determination by ICP-TOF-MS

Total iron concentrations were measured using an ICP-TOF-MS (icpTOF, Tofwerk, Thun, Switzerland) (Hendriks et al., 2017) directly connected to the meltwater stream of the Bern CFA system (Erhardt et al. in prep). Similar to other CFA-ICP-MS setups (Knüsel et al., 2003; McConnell et al., 2002), the sample stream was acidified on-line to 1% HNO_3 (Optima grade, Fisher, USA) adding an internal standard, in this case Rh (TraceCert, Sigma Aldrich, USA), to assess system stability. The system uses a glass concentric nebulizer (Glass Expansion, Australia) and peltier-cooled cyclonic spay chamber. To enable the determination of iron using ^{56}Fe, the collision/reaction cell (Q-Cell) of the icpTOF was pressurized with a mixture of 7% H_2 and 93% He at a flow rate of 5 ml/min.

Calibration measurements where performed before and after each measurement run using dilutions of multi-element standard solution (TraceCert, Sigma Aldrich) ranging from 2 to 20 ng g^{-1}. Data acquisition was run at 250 ms integration time and the data was subsequently down-sampled to 1 mm nominal depth resolution. Average sensitivities for total iron were 11 kcps·ng·g^{-1} at <1.5% RSD and detection limits of 0.13 ng g^{-1} at 250 ms integration time resulting in a LoD of 0.043 ng g^{-1} for the 1 mm resolution data reported here.

2.8 Discrete Sulphate determination

Sulphate measurements were performed on discrete samples collected at a nominal resolution of 2 to 5 cm and later analysed at the Alfred Wegener Institute in Bremerhaven. All samples were analysed by Capillary Ion Chromatography (Dionex 5000+, ThermoFisher Scientific, USA) in a reagent-free system and gradient elution configuration that utilises an Ionpac AS19 resin column (250 x 0.4 mm i.d.) for anions measurements. Overall reproducibility and accuracy are 0.05% and 0.01% RSD respectively, maintaining the sensitivity of the conductivity detector in the range of 0.2-0.5 nS·ng·g^{-1}, resulting in a LoD of 0.07 ng·g^{-1} in the case of sulphate.

3.

Results and discussion

The author has previously published part of the work described in this chapter in:

Burgay, François, et al. "Fe^{2+} in ice cores as a new potential proxy to detect past volcanic eruptions." *Science of The Total Environment* (2018)

3.1 Iron (II) analytical performances

3.1.1 Fe^{2+} method – Calibration and matrix effect

To investigate the matrix effects, a comparison between a calibration made in UPW and in a real Antarctic melted ice was performed. The calibration in UPW (orange line, Figure 25) had a higher sensitivity (248603 $(ng{\cdot}g^{-1})^{-1}$) than the one prepared using the Dome C matrix (blue line, Figure 25, 4902 $(ng{\cdot}g^{-1})^{-1}$). This is consistent with other studies performed on seawater samples (Hansard and Landing, 2006), freshwater samples (Emmenegger et al., 1998) and sea-ice samples (Lannuzel et al., 2006). The matrix effect might be explained by some impurities present both in the samples and in the reagents. Environmental light might as well affect the chemiluminescence signal either enhancing or dampening it.

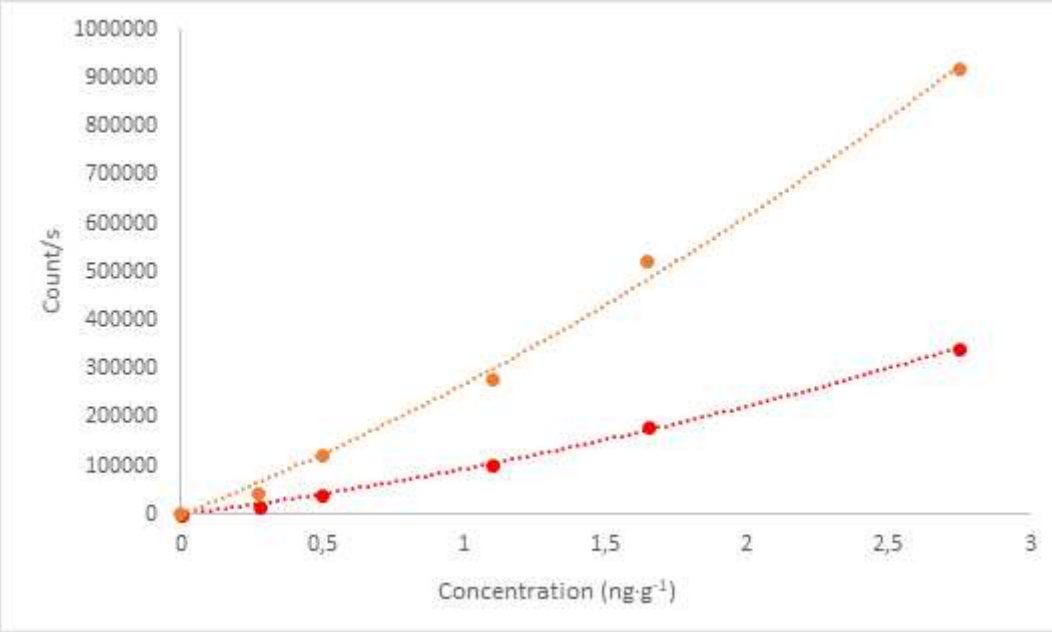

Figure 25 - A comparison between a calibration curve made in UPW (orange dots) and in Dome C matrix (red dots) shows the presence of the matrix effect

Following the procedure proposed by Hansard and Landing (2006), the uncontaminated outflow from the melting unit was stirred for 120 minutes under a laminar flow bench to ensure air dissolution. Subsequently, it was stored under dark conditions and at +4°C for at least 24 hours, considered enough for the oxidation of all the Fe^{2+} in the sample (Hansard and Landing, 2006). The aged matrix was spiked with known concentration of Fe^{2+} (55 $pg{\cdot}g^{-1}$, 110 $pg{\cdot}g^{-1}$and 220 $pg{\cdot}g^{-1}$) to obtain a calibration curve (Figure 26).

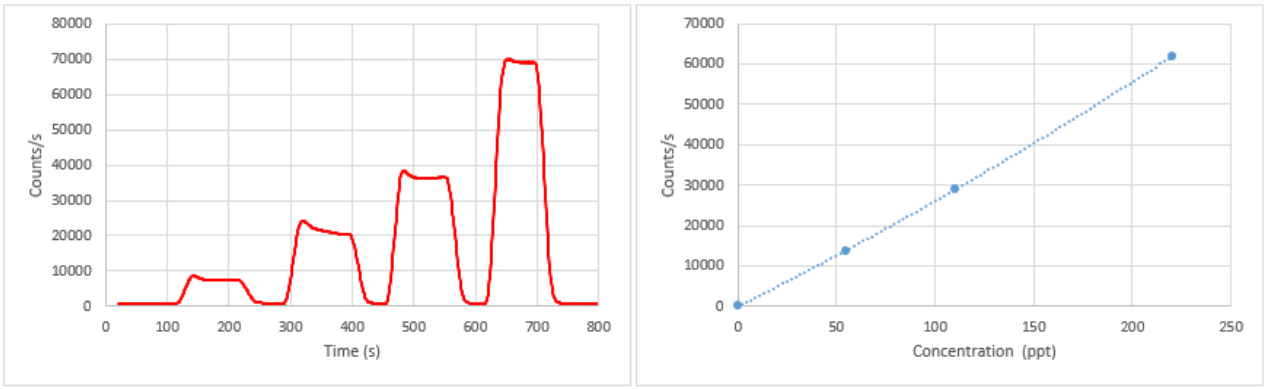

Figure 26 - Typical Fe^{2+} calibration. Left: the signal in continuous mode for the blank, first, second and third standard. Right: the polynomial calibration curve

To evaluate the dynamic range of the method and following the procedure described above, a calibration from 55 pg·g^{-1} to 1760 pg·g^{-1} was done. The calibration curve (Figure 27) was quadratic ($R^2 \geq 0.99$) suggesting the reliability of this method to quantify both the Fe^{2+} input from volcanic eruptions and the aeolian contribution.

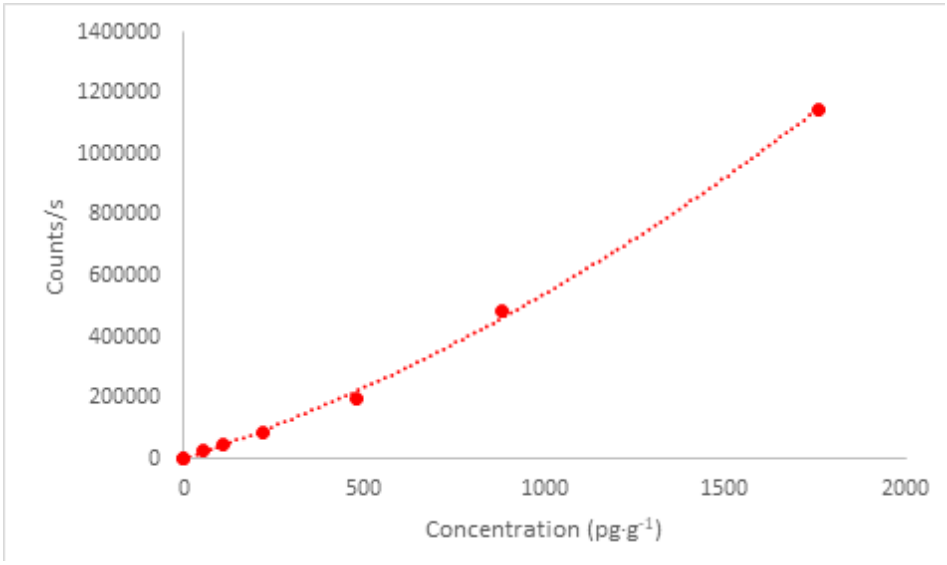

Figure 27 - Linearity test done using aged EGRIP matrix

3.1.2 Fe^{2+} method – Accuracy, reproducibility and Limit of Detection (LoD)

Accuracy is defined as how close we are with our measurements to the true value, while reproducibility is defined how close the readings of the same concentration are. To calculate the accuracy a certified material is needed. Unfortunately, no Fe^{2+} certified material exists for ice matrices. This is the reason why, we tested accuracy doing a recovery test. Using two different ice matrices (Dome C, Antarctica and NEEM, Greenland) we calculated two distinct calibration curves. Then, 2220 pg·g^{-1} and 1375 pg·g^{-1} of Fe^{2+} were added to each matrix and, through the calibration curve, their concentration was calculated. The calculated concentration for Dome C was 2184 ± 4 pg·g^{-1} (recovery: 99.4%) and for NEEM was 1535 ± 3 pg·g^{-1} (recovery: 113%).

For the reproducibility, we measured the same standard at 55 pg·g^{-1} five times (Table 6). The standard was prepared fresh after each reading to avoid oxidation problems. Every reading lasted 60 seconds (integration time: 1 second). The reported value is the average. We conclude that reproducibility of the method is about 3-4% RSD.

Table 6 - Reproducibility was determined reading the same standard at 55 pg·g^{-1} five times. Counts/s for each reading (from 1 to 5) are expressed. σ = standard deviation; Ave = Average.

Standard	**1**	*σ*	**2**	*σ*	**3**	*σ*	**4**	*σ*	**5**	*σ*	**Ave**	*σ*
55 pg·g^{-1}	40918	*1%*	40012	*2%*	40354	*1%*	39504	*1%*	36992	*2%*	**39556**	*4%*

The detection limit was calculated by repeated analysis of the ice sample matrix after 48 h of storage in the dark and calculated as three times the standard deviation of the blank concentration. We calculated the detection limit (LoD) before each run and, under these conditions, its value varied from 0.5 pg·g^{-1} to 10 pg·g^{-1} (median value: 4.5 pg·g^{-1}). The method shows a sensitivity that is one order of magnitude higher than the other available method for the detection of Fe^{2+} in ice matrices (Spolaor et al, 2012).

3.1.3 Fe^{2+} method – Sensitivity

During the analytical session, we calibrated our data with either a linear or a quadratic curve. The reason why we observed different calibration curves is mainly due to the change of the reaction conditions (e.g. light, impurities in the reagents, temperature…). This lead to the production of free radicals during the analytical session that might change the sensitivity of the method (Rose and Waite, 2001). As shown in Table 7, it appears crucial to calibrate frequently (every 2 hours) data since the sensitivity might change significantly (≈ 30%) during one day of analysis. The sensitivity for the quadratic curve was obtained, calculating the first derivative of the calibration curve at the point x_0, where x_0 = 110 pg·g^{-1}.

Table 7 - How sensitivity changes for the Fe^{2+} method during one day of CF

Calibration n°	**Sensitivity (pg·g^{-1})$^{-1}$**	**Fitting**	**Solution**	**R^2**
1	421	Polynomial	Luminol_1	R^2 = 0.99
2	323	Polynomial	Luminol_1	R^2 = 0.99
3	353	Polynomial	Luminol_1	R^2 = 0.99
4	456	Polynomial	Luminol_2	R^2 = 0.99
5	549	Polynomial	Luminol_2	R^2 = 0.99

We used a polynomial fit where the R^2 for the linear one was < 0.99. However, it is worth noting that during the same day we used either polynomial or linear fittings for all the calibrations. This suggests that the "day by day" different conditions (especially in terms of reagent preparation, shielding of tubing…) caused the observed differences in terms of calibration fitting.

3.1.4 Fe^{2+} method – Fe^{2+} oxidation in melted ice matrices

Fe^{2+} species are easily oxidized by O_2 to the more stable Fe^{3+} form. To understand how fast this process is in ice matrices, we evaluated the oxidation kinetic of 55 pg·g^{-1} of Fe^{2+} added to an aged ice matrix from EGRIP (Greenland) at room temperature. We compared the results with not-acidified Ultrapure Water (Figure 28). The Fe^{2+} oxidation follows first order kinetics and it appears significantly different between Ultrapure Water and the EGRIP matrix. In particular, EGRIP (blue dots, Figure 28) shows a lower half-life time (117 minutes) than the one obtained for Ultrapure Water (347 minutes, yellow dots, Figure 28).

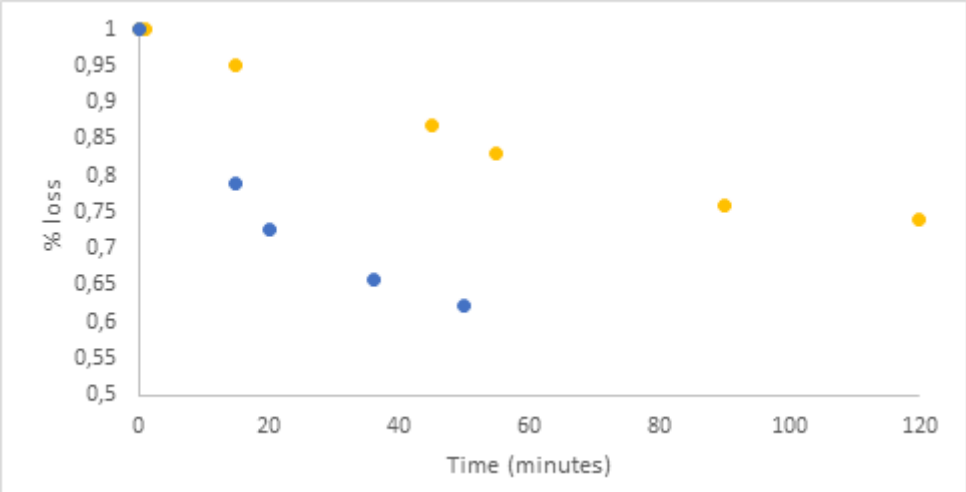

Figure 28 - Comparison of Fe^{2+} oxidation in UPW (yellow dots) and in melted and aged EGRIP matrix (blue dots).

To calculate the kinetic constant and the half-life time of first order reactions, we recall that the rate law of a first order reaction is (eq. 18):

$$[A] = [A]_0 \cdot e^{-kt} \qquad \text{(eq. 18)}$$

To calculate the kinetic constant, we use the Fe^{2+} concentration [A] calculated at 50 minutes for EGRIP and 55 minutes for UWP water. $[A]_0$ is the concentration at the beginning of the run.

To calculate the half-life time we substitute $[A] = [A]_0/2$ in eq. 2 and we obtain eq. 19

$$t_{1/2} = \frac{\ln 2}{k} \qquad \text{(eq. 19)}$$

In Table 8, we present the results for both the kinetic constant and the half-life time.

Table 8 - Kinetic constant and half-life time of Fe^{2+} oxidation in EGRIP and in UWP water

Matrix	Kinetic constant /min^{-1}	Half-life time / min
EGRIP	0.005	117
UPW	0.002	347

Our findings were compared with the results obtained by Spolaor et al (2012). This study reported an half-life time in UPW of 250 minutes which is of the same order of magnitude of our results. Furthermore, they show that in real ice matrices the oxidation might be two times faster than in UPW, suggesting that it is crucial analysing the sample water within 120-180 seconds.

The results obtained from our study, together with data reported in the literature (Spolaor et al., 2012; Morgan and Lahav, 2007; Zhuang et al., 1995) suggest that there is not a significant Fe^{2+} loss from the melthead to the detector (approximately 90 seconds).

3.2 Fe^{2+} – Discrete analyses calibration

For both the Dome C snowpit and the Holtedahlfonna ice core, we performed discrete sample analysis through the standard addition method. In particular, we acidified 10 ml of sample to pH = 2 and then we analysed it for 120 seconds at 1 ml min^{-1}. Then we spiked the sample with 20 µl of daily prepared 13.2 ng g^{-1} standard Fe^{2+} solution and we recorded the signal for 90 seconds. We repeated the procedure for three standard additions. We added 33 pg·g^{-1}, 73 pg·g^{-1} and 125 pg·g^{-1} of Fe^{2+} obtaining a linear calibration curve with $R^2 \geq 0.99$ (Figure 29).

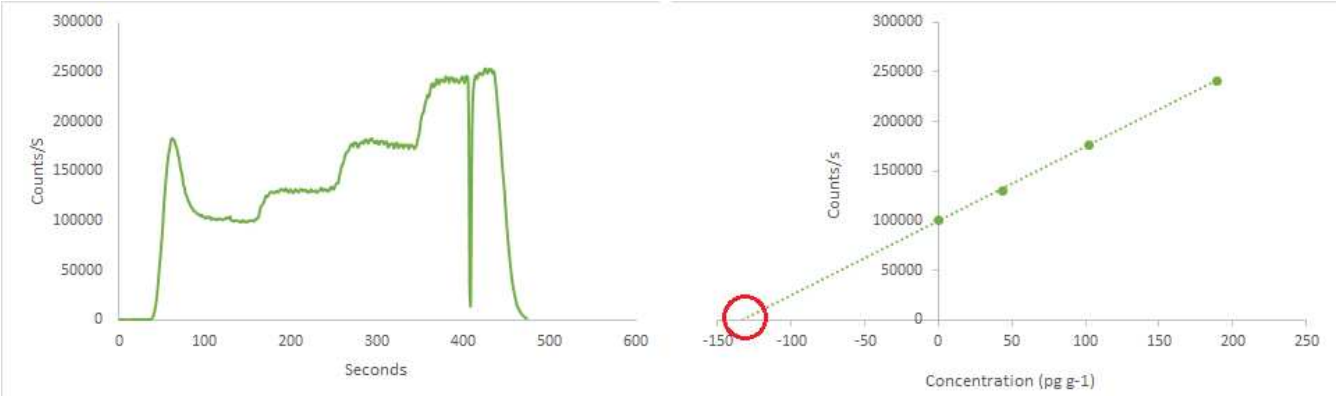

Figure 29 – For discrete Fe^{2+} analysis on snow samples an external calibration was performed. The melted sample was immediately analysed for 120 seconds at 1ml min^{-1} (first point at "concentration = 0"). Subsequently 20 µl of daily prepared 13.2 ng g^{-1} standard Fe^{2+} solution were added to obtain the calibration curve. The actual concentration of the sample was the one extrapolated at count/s = 0.

3.3 Total Soluble Iron analytical performances

3.3.1 Total Soluble Iron method – Calibration and matrix effect

The absorption method to detect total soluble Iron relies on the catalytic reaction of Fe^{3+} on the oxidation of N,N-dimethyl-p-phenylenediamine (DPD) by hydrogen peroxide in weakly acidic media (Hirayama and Unohara, 1988) to a semiquinonic form (DPDQ). Absorption was monitored at 514 nm. The method has been already applied for other ice cores analysis (Hiscock et al., 2013; Spolaor et al., 2012; Traversi et al., 2004) with detection limits lower than 0.05 ng g^{-1}. In the framework of the B17 analysis, an optimized version of the method is proposed in terms of analytical setup. Furthermore, we looked for the presence/absence of matrix effects that has never been done before. To do that, a standard addition calibration using a B17 aged matrix and an external calibration in UPW were performed (Figure 30). The sensitivities of the two calibration curves were compared and a *t-test* (α = 5%) was performed to evaluate if a significant difference between them existed. The method does not show any matrix effect.

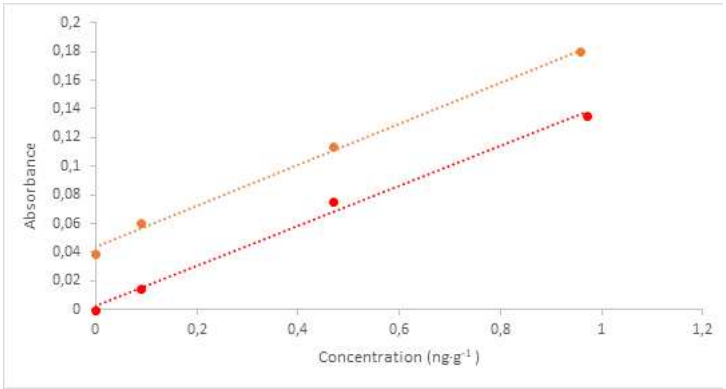

Figure 30 – Comparison between a calibration made in UPW (red line) and B17 matrix (orange line) to look at the possible presence of matrix effects.

Calibrations were done using three not-acidified standards which were freshly prepared from the mother solution at 1 mg·g^{-1} concentration immediately before. Calibrations were linear with $R^2 \geq 0.99$. The typical signal in continuous mode and the typical calibration curve are shown in Figure 31.

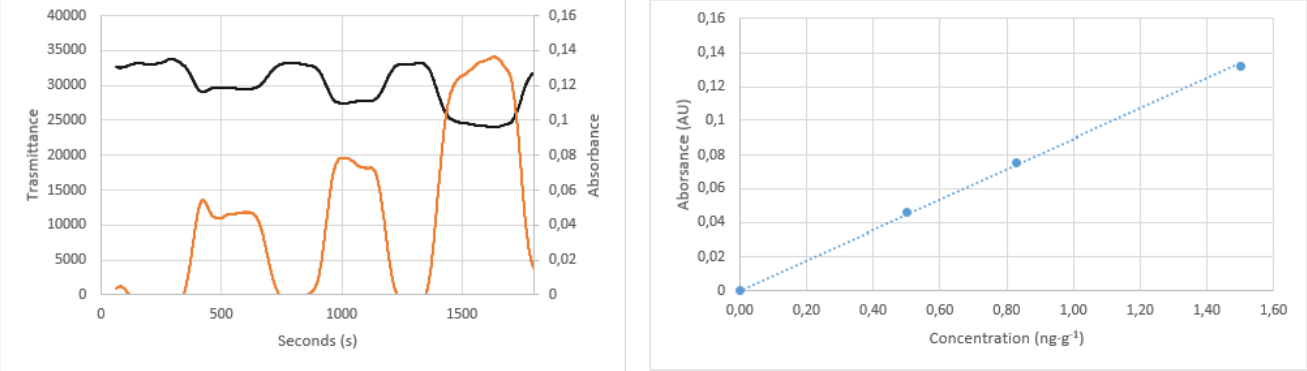

Figure 31 - Left: calibration in continuous mode. Black line represents the signal in transmittance, while the orange is the signal in absorbance. Right: calibration curve in the range 0.50 ng·g^{-1}, 0.83 ng·g^{-1} and 1.50 ng·g^{-1}.

To evaluate the linearity of the method we calculated a calibration curve from 0.5 ng·g^{-1} to 8 ng·g^{-1} (0.5 ng·g^{-1}, 1 ng·g^{-1}, 2 ng·g^{-1}, 4 ng·g^{-1}, 8 ng·g^{-1}). The calibration curve was linear up to the highest standard ($R^2 = 0.9975$) without showing any memory effect (Figure 32). This is consistent with previous results (Traversi et al., 2004; Spolaor et al., 2013; Hiscock et al., 2013).

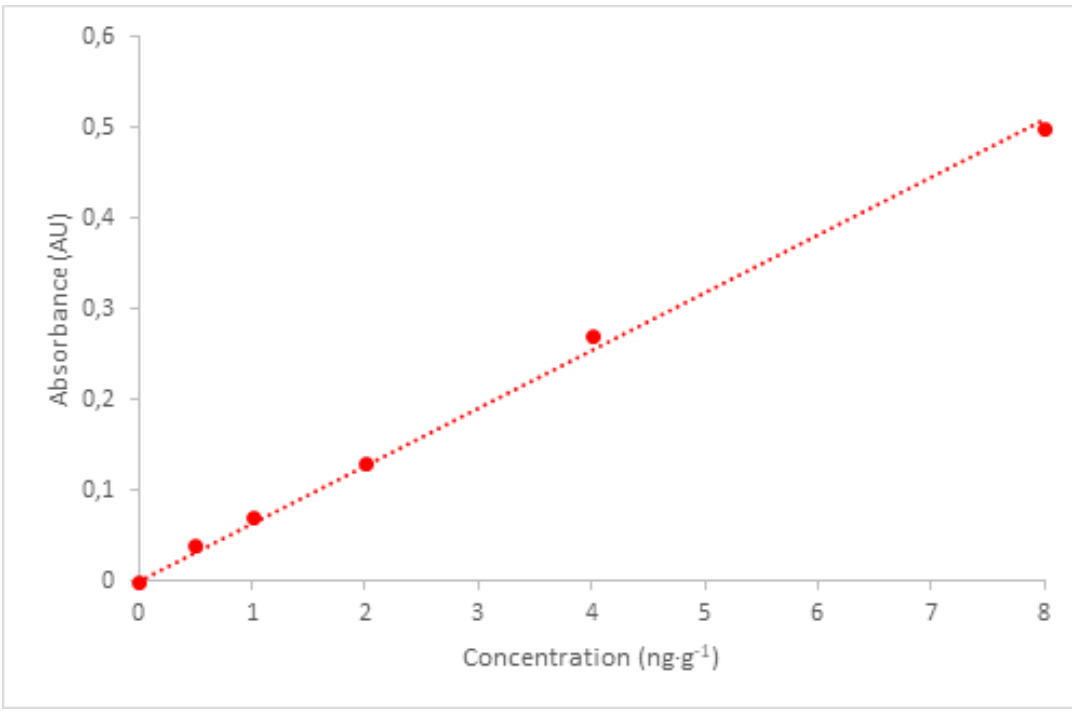

Figure 32 - Linearity test for the total soluble iron method from 0.5 ng·g^{-1} to 8 ng·g^{-1}

3.3.2 Total Soluble Iron method – Accuracy, reproducibility and LOD

As for the Fe^{2+} method, we tested accuracy doing a recovery test. We realized a calibration curve (from 0.047 $ng \cdot g^{-1}$to 1 $ng \cdot g^{-1}$, R^2 = 0.99) and then we analysed a standard at known concentration (0.50 $ng \cdot g^{-1}$) prepared in UPW. Through the calibration curve, we obtain a value of 0.52 ± 0.04 $ng \cdot g^{-1}$, which corresponds to an accuracy of 96%.

For reproducibility we measure the same standards at 0.5 $ng \cdot g^{-1}$ and 1 $ng \cdot g^{-1}$ five times each for 60 seconds (integration time: 6000 µs) and we found a precision of 2% RSD (Table 9). However, precision was worst for lower standards: for a standard at 0.05 $ng \cdot g^{-1}$, precision calculated in the same way as before was of 19% RSD.

Table 9 - Precision of the total soluble iron method calculated reading five times two standards at 0.5 and 1.0 ng·g-1. Ave = average. σ = standard deviation

Standard	**1**	*σ*	**2**	*σ*	**3**	*σ*	**4**	*σ*	**5**	*σ*	**Ave**	**σ**
0.5 $ng \cdot g^{-1}$	20704	*2%*	21691	*1%*	21049	*2%*	21842	*1%*	21397	*2%*	**21336**	**2%**
1.0 $ng \cdot g^{-1}$	18251	*1%*	19058	*1%*	19301	*1%*	19236	*1%*	18631	*1%*	**18895**	**2%**

The LoD, calculated as three times the standard deviation of the blank was 0.020 $ng \cdot g^{-1}$, lower than the one reported by both Traversi et al. (2004) and Spolaor et al., (2012), but of the same order of magnitude than the one obtained by Hiscock et al. (2013). It must be said that during routine CFA, the LoD might increase up to 0.1 $ng \cdot g^{-1}$. However, it is low enough to catch most of the seasonal cycles during the Holocene.

3.3.3 Total Soluble Iron method – Sensitivity

We found that during one day of analysis, sensitivity might change significantly (Table 10). This is the reason why, as for the Fe^{2+} method, frequent calibrations are needed to take into account fluctuations in sensitivity. Changes in sensitivity might be related to changes in the environmental temperature. This is the reason why it is strongly suggested, for future studies, to control the temperature.

Table 10 - How sensitivities changes for the total soluble iron method during one CFA session (1 day)

Calibration n°	**Sensitivity $(ng \cdot g^{-1})^{-1}$**	**Fitting**	**R^2**
1	0.065	Linear	R^2 = 0.99
2	0.037	Linear	R^2 = 0.99
3	0.041	Linear	R^2 = 0.99
4	0.051	Linear	R^2 = 0.99

3.3.4 Total Soluble Iron method – Optimization of the analytical setup

Because hydrogen peroxide is used as an oxidizing agent, one of the main problems of the total soluble iron method is the microbubble formation in the Z-cell. We found that increasing the concentration of Brij-L23 in the buffer solution reduces the possibility of bubbles to get stuck in the Z-cell. Furthermore, the introduction of a vacuum degasser just before the Z-cell (Systec, IDEX, USA) helped in reducing significantly the amount of microbubbles and in obtaining a more stable baseline.

Since the system is characterized by several meters of tubing, minimizing backpressure is a key parameter not to be neglected. Using the Hagen-Poisseuille equation (eq. 20), we calculated the right tubing length in order to equalize the flow pressure at the mixing joints.

$$\Delta P = \frac{8\mu L Q}{\pi R^4} \qquad \text{(eq. 20)}$$

Where:

ΔP is the pressure difference between the two ends,

L is the length of pipe,

μ is the dynamic viscosity,

Q is the volumetric flow rate,

R is the tubing radius.

3.3.5 Total Soluble Iron method – Oxidation of the DPD

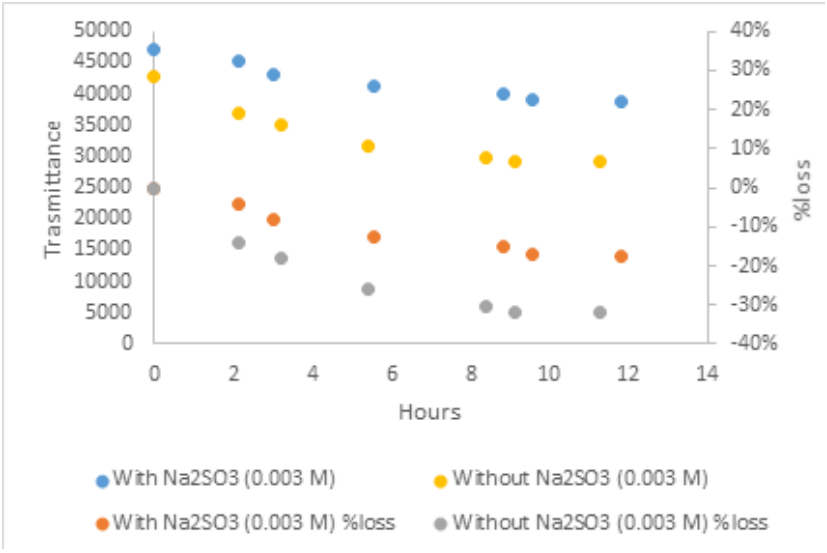

Figure 33 - DPD oxidation with and without sodium sulphite

As stated above, the oxidation of the colourless DPD into its semiquinonic form (DPDQ) catalysed by the Fe^{3+} species dissolved in the matrix, is the key reaction of the method. However, DPD is quickly oxidized by air, which means that the baseline might change during the run. The proposed solution was to prepare the DPD solution in a reductive environment. In particular in a 0.003 M solution of Na_2SO_3 (Hydes and

Liss, 1976) that acts as an oxygen scavenger (Hiscock et al., 2013). In Figure 33 it is possible to see that the drift is somewhat lower for the solution with Na_2SO_3 (*rDPD*, blue and orange dots) than the one without Na_2SO_3 (*oDPD*, yellow and grey dots). During one day of analysis 18% of the rDPD is oxidized into the DPDQ form, while 32% of the oDPD is oxidized. Comparing the kinetic costants, we can conclude that the oDPD oxidation (k_{oDPD} = -0.034) is 2.125 times faster than that of rDPD (k_{oDPD} = -0.016).

3.4 Total Soluble Aluminium analytical performances

3.4.1 Calibration, matrix effect and LoD

We performed a calibration in the range 0-15 ng·g^{-1} both to evaluate the linearity of the method and to check the Limit of Detection (Figure 34). The method appears to be linear ($R^2 \geq 0.99$) in the studied interval according to previous studies (Traversi et al., 2004; Spolaor et al., 2012). The detection limit we found was 0.123 ng·g^{-1} which is one order of magnitude higher than the one reported by Traversi et al., (2004) (0.01 ng·g^{-1}) but the same as the one reported by Spolaor et al., (2012).

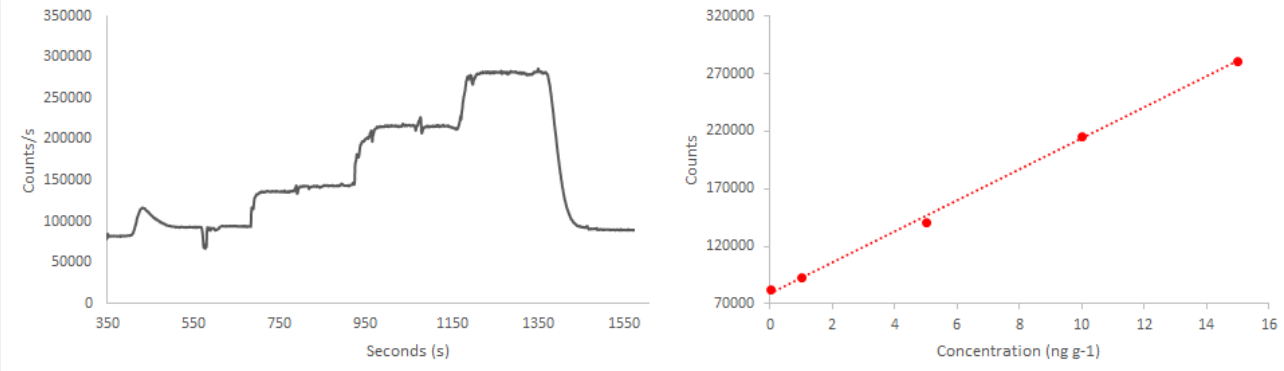

Figure 34 - Calibration and linearity test from 1 ng g^{-1} to 15 ng g^{-1}.

Matrix effects were also investigated. As for the total soluble Iron, no previous studies have been performed about the matrix effect for the soluble aluminium method in ice cores. For this purpose, we performed an external standard calibration and we compared the slope with a calibration done using the standard addition method on an Antarctic melted ice sample. The results (Figure 35), obtained in the range 0 - 10 ng·g^{-1} showed a significant difference between the slope of the two calibration curves, suggesting the presence of a matrix effect. However, further studies on different matrices (e.g. ice from Greenland) are needed to better clarify this effect.

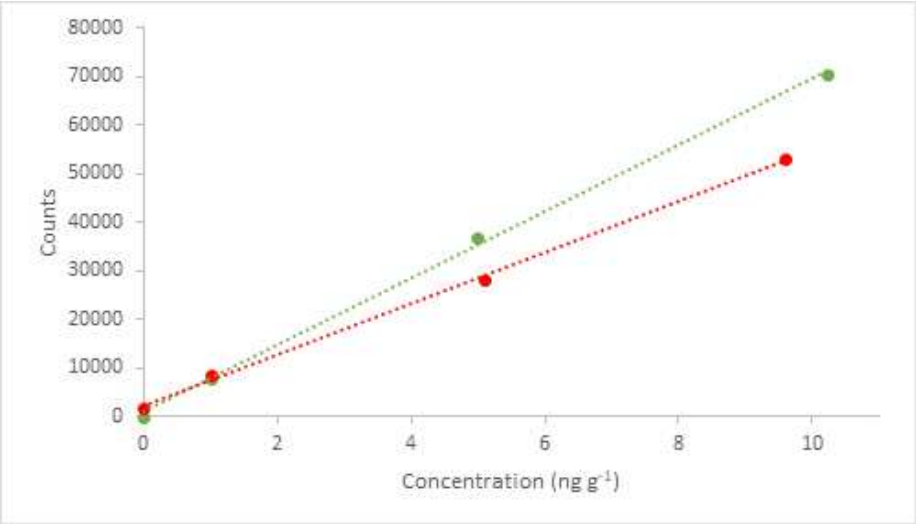

Figure 35 - Evaluation of the matrix effect for the soluble aluminium method. Green line: external standard calibration; Red line: standard addition calibration performed on an Antarctic melted ice sample.

3.4.2 Accuracy and precision

The standard deviation associated to a single measurement (reading time: 60 s) varied from 0.2% to 1.9%. When we read the same standard at 5 ng g^{-1} three times we obtain a precision of 2.2% (Table 11).

Table 11 - Evaluation of the analytical precision of the soluble Al method

Standard	**1**	*σ*	**2**	*σ*	**3**	*σ*	**Ave**	**σ**
5 ng·g^{-1}	127145	*0.4%*	126679	*0.8%*	131874	*0.5%*	**128566**	**2.2%**

The accuracy of the method was quantified through a recovery test at 5 ng·g^{-1} and was 93%. This means that the method slightly underestimates the actual concentration.

3.5 Summary of the method performances

The main performances of the three developed and optimized analytical methods are reported in Table 12. All the methods are suitable for application on real ice core matrices from both Greenland and Antarctica.

Table 12 - Accuracy, Precision and Limit of Detection (LoD) for the three CFA methods developed during the PhD thesis

Method	**Accuracy**	**Precision**	**LoD /ng·g^{-1}**	**Concentration range in ice cores**	**Matrix effect**
Total Soluble Iron	96%	2.0 %	0.05	LoD-4 ng g^{-1}	No
Soluble Fe^{2+}	99%-113%	4.0%	0.0045	LoD – 590 pg g^{-1}	Yes
Soluble Aluminium	93%	2.2%	0.123	0.8 – 6 ng g^{-1}	Yes[6]

[6] However, the method should be tested on different ice matrices

3.6 Application on the B17 ice core

The new CFA-CL-Fe^{2+} method, the optimized total soluble iron method and the total iron method were applied to selected sections of the B17 ice core: from 1777 AD to 1850 AD (Figure 4, left panel) and from 1589 AD to 1611 AD (Figure 4, right panel). Values for total soluble iron vary from the LoD (0.020 ng g^{-1}) to 4 ng g^{-1}, while Fe^{2+} concentration ranged from the LoD (0.0045 ng g^{-1}) up to 590 pg g^{-1}. Total iron values ranged from the LoD (0.043 ng g^{-1}) to 25 ng g^{-1}.

Both total soluble iron and total iron show a seasonal pattern corresponding to the winter/spring maximum in dust fluxes (Lupker et al., 2010), while the Fe^{2+} signal is mainly influenced by volcanic events where it can be up to 50 times higher than the baseline. Time series of conductivity, dust and sulphate are also included. These findings are reported on a paper that was recently published on Science of the Total Environment (Burgay et al., 2018).

3.6.1 Fe^{2+} as a new potential proxy to detect past volcanic eruptions

Volcanic eruptions emit large quantities of SO_2, which are then converted in the atmosphere into sulfuric acid and into sulphate (SO_4^{2-}). Both the continuous and discrete quantification of sulphates are widely use to date and synchronize ice cores. However, these methods struggle to achieve the sensitivity and the limits of detection needed for deep polar ice analyses. Volcanoes emit a wide variety of other chemicals too. This includes large quantities of soluble and bioavailable iron which, especially at the low pH values of the volcanic aerosol, is present as Fe^{2+}.

Performing a continuous total soluble iron a Fe^{2+} analysis on a Greenland ice core (B17) from 1850 to 1777 and from 1611 to 1589 we were able to detect seven past volcanic eruptions. Furthermore, through an outliner detection method, a high correspondence between sulphate, the main proxy for detecting past volcanic eruptions, and the Fe^{2+} was found. In details, the 86% of the SO_4^{2-} peaks were associated to Fe^{2+} peaks. Only one eruption, the Ruiz (1596 A.D.), did not result into a significant sulphate outliner and this can be explained by the low VEI that this eruption has. The results suggest that Fe^{2+} might be a suitable proxy for identifying past volcanic events.

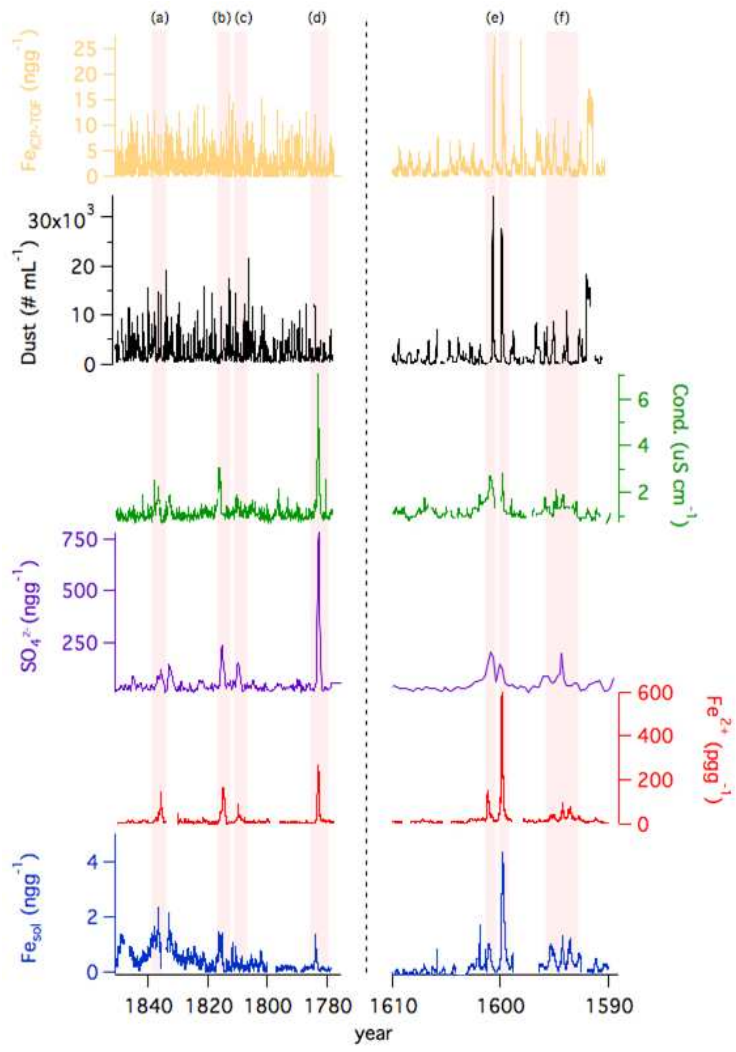

Figure 36 - Results from the B17 melting campaign. More details in the text

In the first frame (Figure 36, left panel) we detected four volcanic eruptions: the (a) Cosigüina eruption in 1836 (12.98°N, 87.34°W) (Longpré et al., 2014), the (b) Tambora eruption in 1816 (8.15°S 118.00°E), an (c) Unknown eruption that happened in 1810 (Dai et al., 1991) and the (d) Laki eruption in 1783 (Thordarson and Self, 2003). All these eruptions were particularly strong (Volcanic Explosivity Index ≥ 5). The Cosiguina one, with its 40.2 Tg and 13.4 Tg of sulphate aerosol injection, was the largest and most explosive in Central America since Spanish colonization (Scott et al., 2006). The Tambora eruption in Indonesia is the strongest documented eruption with 140 Gt of expelled magma and with 60 Mt of sulphur injected into the stratosphere. To make a comparison, the sulphur injection into the atmosphere was six-fold the one from the 1991 Pinatubo eruption. The radiative forcing caused by the Tambora in the year that followed the eruption was about -5W·m^{-2} (Raible et al., 2016) and lead to the so-called "year without summer" (Oppenheimer, 2003) with a cooling over Europe of about 0.4-0.8°C relative to the climatological mean (D'Arrigo et al., 2009). The Laki eruption emitted appr7oximately 122 Mt SO_2 into the atmosphere that triggered an unsual hot summer followed by a severe winter in Europe and North America. The temperature anomaly recorded for the following 2-3 years were around -1.3°C (Thordarson and Self, 2003).

In the second time frame (Figure 36, right panel), the (e) Huaynaputina (16°36′30″S 70°51′00″W) eruption in 1600 was the strongest recorded. Thanks to the developed high-resolution method, it was possible to detect two different peaks suggesting either that the eruption has occurred over two different periods or that the atmospheric deposition occurred in two different occasions.

An increase in both sulphate and soluble iron concentrations was detected also from 1594 to 1596. Even though it is difficult to associate these events to a precise volcanic eruption, it is possible to infer that they might belong to the Raung in 1594 (8°07′30″S 114°02′30″E) and Ruiz in 1596 (04°53′43″N 75°19′21″W).

3.6.2 Iron speciation during volcanic eruptions

In coincidence with volcanic eruptions, both Fe^{2+} and total soluble iron were affected. More in details, their concentrations increased from 7 ± 4 pg g^{-1} and 0.6 ± 0.2 ng g^{-1} in quiescent periods respectively, up to 560 560 pg g^{-1} and 4 ng g^{-1} during the Huaynaputina eruption respectively. However, if the Fe^{2+} concentration during the volcanic eruptions was two orders of magnitude higher than the average value, this was not always verified for the total soluble iron. As an example, from between 1820 and 1830 spikes higher than 1 ng g^{-1} were detected and they were comparable to the one associated with the Unknown (1810) eruption. This suggests that if Fe^{2+} uniquely identifies a volcanic eruption, total soluble iron does not.

It is possible to extend the same conclusion for the total iron detected by the ICP-TOF-MS. What is more, total iron did not increase significantly for 6 out of 7 volcanic eruptions and it was impossible to discern the possible volcanic contribution from the seasonal one. The only eruption that showed a remarkable increase in concentration (up to 24 ng g^{-1}) was the Huaynaputina eruption.

Finally, we investigated if the increase in the soluble iron with respect to the total iron was a possible tool to detect volcanic events (Table 13). We observed that, even though for two volcanic events (Cosiguina and Tambora) the soluble fraction was up to 50% of the total iron, for other events the percentage decreased down to 20% suggesting that neither this parameter is a suitable proxy for volcanic eruptions.

3.6.3 Seasonality

Both total iron and total soluble iron show a season pattern with values that range from below the LoD (0.043 ng g^{-1}) to 10 ng g^{-1} and from below the LoD (0.020 ng g^{-1}) up to 2.0 ng g^{-1} respectively. The Fe^{2+} profile is well correlated (R = 0.8) with the total soluble iron. This indicates that also this species has a seasonal profile. Iron deposition over the Greenland ice sheet is mainly due to the seasonally enhanced dust transport from Central Asian desert areas (Bory et al., 2002) with some smaller contributions from the Sahara and Alaska (Lupker et al., 2010).

3.6.4 Comparison between the continuous Fe^{2+} and the continuous SO_4^{2-} determination

Up to now, SO_4^{2-} has been indirectly quantified through the competitive reactions between SO_4^{2-} and Ba^{2+}, which results in an insoluble salt (solubility = 0.0024 g/l at 25 °C), followed by the reaction between Ba^{2+} and methylthymol blue (MTB). Indirect quantification of sulphate it is possible by either monitoring the absorbance at 460 nm for the uncomplexed MTB or at 608 nm for the MTB-barium complex (Bigler et al., 2002). As sulphate concentration increases, the concentration of MTB-Ba decreases while the concentration of the uncomplexed MTB increases. In this section, we want to compare the analytical performance of this method with the sensitivity of the new Fe^{2+} approach. Starting from the simpler analytical setup, we show that Fe^{2+} is a suitable alternative to detecting volcanic eruptions.

If we compare the method performances for the Huaynaputina eruption (Table 14), we see that the Fe^{2+} method shows a higher S/N ratio (S/N = 45) than the sulphate one (S/N = 10). The Fe^{2+}-CL method has a LoD that is 5 orders of magnitude lower than that reported for the sulphate method. This should allow us to identify volcanic events with a VEI < 5. Moreover, it indicates that this technique might be particularly suitable for deep ice cores where the low sample availability requires high-resolution techniques (e.g. Epica Oldest Ice project whose aim is to reconstruct the Earth climate and environmental conditions of the last 1.5 million years).

3.6.5 Conclusions

Through the analysis of the B17 ice core and the validation of the new CFA-CL-Fe^{2+} method, it was possible to identify up to seven past volcanic eruptions suggesting that Fe^{2+} might be a promising proxy for this purpose. The low detection limit, the high sensitivity, precision and accuracy together with a fast analytical response and the absence of memory effects suggest that this method might be applied on older ice where the low sample availability requires high-resolution techniques.

Together with the continuous determination of total soluble iron and total iron with the ICP-TOF-MS, it was possible to provide the first iron speciation on ice cores by distinguishing among the bioavailable, the soluble and the particulate fraction of iron.

Table 13 - Main eruptions identified through the new approach. n.a. = not available. Distance is reported as direct line (as the crow flies) from the volcano to the B17 site.

Year	Volcanic event	VEI	Distance /km	$[Fe^{2+}]$ /pg g^{-1}	[Soluble Fe] /ng g^{-1}	[Total Fe] /ng g^{-1}	$[Fe^{2+}]$/ [Soluble Fe]	[Sol. Fe]/ [Total Fe]	$[SO_4^{2-}]$ /ng g^{-1}
1836	Cosigüina	5	7500	150	2.0	4.0	0.08	0.5	110
1816	Tambora	7	12400	160	1.4	3.7	0.11	0.4	217
1810	*Unknown*	≥ 5	n.a.	90	0.9	5	0.10	0.2	130
1783	Laki	6	1400	260	1.3	6.3	0.20	0.2	780
1600	Huaynaputina	6	10500	570	4.2	24	0.14	0.2	208
1596	Ruiz?	4	8100	40	1.0	11.4	0.04	0.1	90
1594	Raung?	5	12000	94	1.27	7.0	0.07	0.2	199

Table 14 - Comparison between the Fe^{2+} method and the CFA-sulphate methods commonly used to detect past volcanic eruptions in ice cores

	LOD	Sensitivity	Accuracy	Precision	S/N ratio	Matrix effect
Fe^{2+} method (Burgay et al., 2018)	4.5 pg·g^{-1}	420 (pg g^{-1})$^{-1}$	99-113%	3-4%	45	Yes
SO_4^{2-} method (Bigler et al., 2002)	40 ng·g^{-1}	0.25 (ng g^{-1})$^{-1}$	67-99%	15%	10	No

4.

Processes affecting iron solubility in ice and snow

4. Processes affecting iron solubility in ice and snow

Both during transport as aeolian mineral dust (which is the main iron source for ice cores) and once deposited on ice or entrained in sea-ice, iron species might undergo several chemical transformations modifying the equilibrium between Fe^{3+} and Fe^{2+} species. It was found (Zhuang et al., 1992) that the soluble fraction of iron in aerosols was ≈ 1% close to the sources, while it increased up to 10-40% farther away. The first explanation of this phenomenon was linked to the Sulphur cycle. The biogenic dimethylsulphide (DMS) emitted from the ocean surface might directly influence the Fe^{2+}/Fe^{3+} ratio in the aerosols enhancing the Fe(III) photo-reduction. In more detail, the oxidative atmospheric processes that involve DMS provide more SO_2 and H_2SO_4 leading to an acidification of the superficial dust layers. This, in turn, results in an increased solubilisation of Fe(III) that can be photo-reduced to Fe^{2+}.

The second explanation is related to the kinetics of the Fe(III) photo-reduction which is faster in ice media (i.e. cloud condensation nuclei) under ultraviolet and visible irradiation at low pH values (Kim et al., 2010) than in aqueous solution. The reason why both dissolution and photoreductive reactions are faster in ice media rather than in an aqueous one, can be ascribed to the "freeze concentration effect" (Takenaka et al., 1996), which concentrates iron oxide particles, organic ligands and protons in the liquid-like boundary domains in ice accelerating the dissolution and reduction of iron oxides. Under dark conditions, only the dissolution of iron oxides take place. Iron oxides can be also dissolved under dark condition (Jeong et al., 2012).

The above-mentioned "freeze concentration effect" is also involved in different post-depositional transformations. Besides the photochemical dissolution of iron oxides described above, Kim et al., (personal communication) showed, under laboratory conditions, that in the ice-grain boundary layer, the reaction between Fe(III) and I^- was enhanced (eq. 21) resulting in the production of Fe^{2+}_{aq} and I_3^- species, under acidic conditions (pH ≤5). The mechanism involves a ligand to metal charge transfer (LMCT) followed by the dissolution of Fe^{2+}. I_3^- originates from the disproportionation reaction $I_2^- + I_2^-$. This last reaction takes place both under light and dark conditions. However, it is slower in the absence of light probably because under irradiation another mechanism occurs. Photons promote the excitation of one electron in the conduction band which is injected in the lattice Fe(III) to form Fe^{2+} that is then released into the solution. I^- is oxidized by valence band holes.

These processes suggest a new interesting mechanism that can provide, on the one hand bioavailable iron to the HNLC area during the sea-ice melting season, on the other hand gaseous iodine compounds in the polar atmosphere. Among the several climatic impacts that gaseous iodine species have (Saiz-Lopez et al., 2007; Saiz-Lopez et al., 2008), they might promote the generation of ultrafine aerosol particles that contribute to the

formation of Cloud Condensation Nuclei (CCN) (Hoffmann et al., 2001), reducing the amount of incoming solar radiation.

$$\alpha Fe_2O_3 + 3I^- + 6H^+ \rightarrow 2Fe^{2+} + I_3^- + 3H_2O \qquad \text{(eq. 21)}$$

Organic ligands as well can play an important function in solubilize and stabilize Fe^{2+} species (Baker and Croot, 2010). Their role has been widely studied both in the aerosol and in seawater (Baker and Croot, 2010), while only laboratory studies has been performed on ice matrices (Kim et al., 2010). Organic ligands derive mostly from biogenic and anthropogenic processes as well as oxidation of precursors in the gas or aqueous phase. They can be directly released from biomass burning activities (Talbot et al., 1990), vehicular exhaust emissions (Kawamura et al., 1985) and emissions from vegetation (Kesselmeier and Staudt, 1999). A study performed on a Greenland ice core, showed that anthropogenic sources were higher than the natural ones in the 1950s, with a decrease during the 1990s, suggesting an improvement of engines and subsequent reduction of VOCs emissions (Legrand et al., 2003). Furthermore, especially before the industrial revolution, increased levels of formate and acetate have been often related to wildfire events that occurred in Canada (Legrand et al., 2016; Savarino and Legrand, 1998).

In the following, we provide the first insight on the possible role that organic ligands and iodine might have in promoting the iron dissolution in real snow and ice matrices. We selected two specific polar locations: Dome C (Antarctica) and the Holtedahlfonna glacier (Svalbard Islands) to test the effects of organic ligands and iodine on the Fe speciation and fractionation. The results suggest that the iodine species might enhance the solubilisation of Fe from the lattice where the concentration of organic ligands is low (e.g. Antarctica), while in sites characterized by higher organic ligands concentration and summer thawing (e.g. Svalbard Islands) its role is negligible.

4.1 Fe^{2+} and iodine profile on the snow snowpit collected at Dome C

The results (Figure 37) obtained from a 292.5 cm-depth snow pit at Dome C, showed an average Fe^{2+} concentration of 16 pg g^{-1}. This value is similar to the average concentration determined in Greenland from the B17 ice core (Burgay et al., 2018). The snow pit was dated following the age model for the EPICA Dome C ice core (Parrenin et al., 2007) that attributes the bottom of the snow pit to 1985 A.D. At 195 cm, we observe a five-fold increase in the Fe^{2+} concentration (77 ± 5 pg g^{-1}) with respect to the average value. According to the

age model, the estimated age at 195 cm depth corresponds to the 1991, when the Pinatubo eruption occurred. The increase in Fe^{2+} in snow and ice can be linked both to the large emission of soluble and bioavailable iron from volcanic eruptions (Langmann et al., 2010; Santana-González et al., 2017; Watson, 1997) and to transport and post-depositional processes. During volcanic eruptions, the pH of the snow/ice might decrease from 5.7 to 4.5 pH units (Kjær et al., 2016). A five-fold concentration increase in Fe^{2+} was observed under laboratory conditions with a decrease of 0.5 units of pH (Kim et al., 2010), which means that the iron oxides (e.g. Fe_2O_3) in the volcanic ash might be dissolved and photo-reduced at high dissolution rates. Even though we cannot state if this process is linked more to transport or post-depositional mechanisms, we could consider the enrichment detected in Fe^{2+} in the Dome C snow pit as a direct consequence of the Pinatubo volcanic eruption. The observed increase in Fe^{2+} concentration from between 60 cm to 120 cm (that corresponds to the period that spans from 2000 A.D. to 2006 A.D.) might be linked either to local volcanic activity or to the Concordia Station construction and drilling activities.

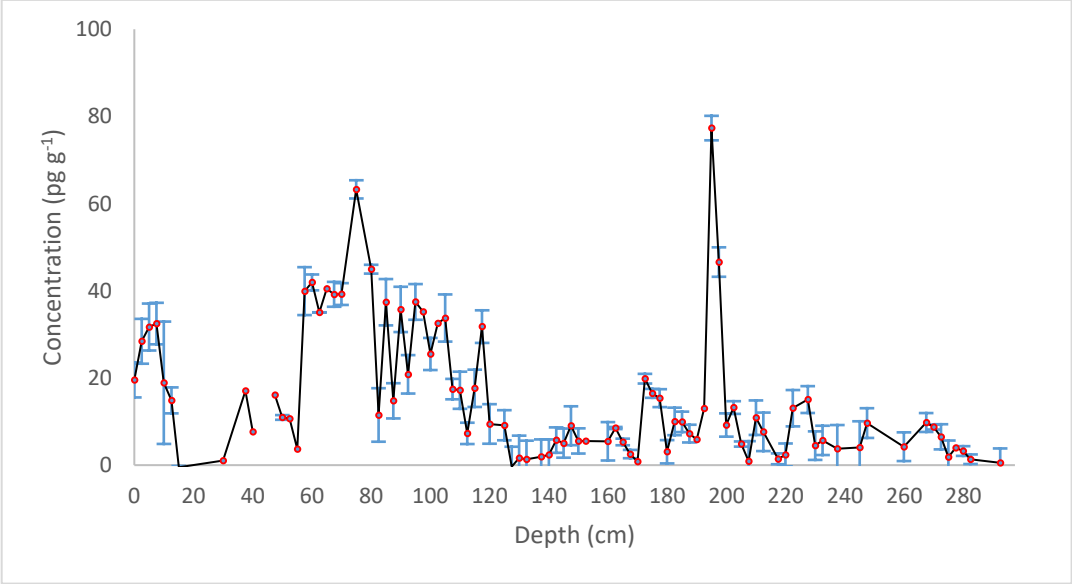

Figure 37 - Fe^{2+} profile obtained from the snowpit collected at Dome C

Another important mechanism that might affect the iron species and might enhance the Fe^{2+} solubilisation is the one that involves the photochemical reaction between Fe(III) and iodine as suggested by Kim et al., 2018 (eq. 21). Iodine concentration in the selected frame ranged from between 7 pg g^{-1} to 70 pg g^{-1} with an average value of 32 pg g^{-1} ± 16 pg g^{-1}. Considering that this reaction promotes the dissolution and the subsequent photo-reduction of Fe(III) species from the lattice to the aqueous phase, we investigated the possible role that iodine might have through the comparison of the $Fe^{2+}/Fe_{(tot)}$ ratio with the iodine concentration. Since iodine quantification was only possible from 70 cm to 245 cm (70% of the entire snow pit) due to the lack of sample, we focused on this frame. Here, we found a significant correlation (r = 0.537)

between the $Fe^{2+}/Fe_{(tot)}$ ratio and the Iodine concentration (Figure 38). This suggests that the theoretical results obtained by Kim et al., 2018 could play a not negligible role in controlling Fe^{2+} production in the inner Antarctic Plateau. Even though we did not performed a mineralogical study, Fe in the ice is mainly present as Fe_2O_3 and the ratio between Fe^{2+} and Fe(III) at the surface is of about 30:70 (Baccolo et al., 2018). This suggests that the mechanism proposed by Kim et al., is likely to happen in the analysed snowpit. However, further studies on the mineralogical composition of the snow matrix are strongly suggested to validate this preliminary hypothesis.

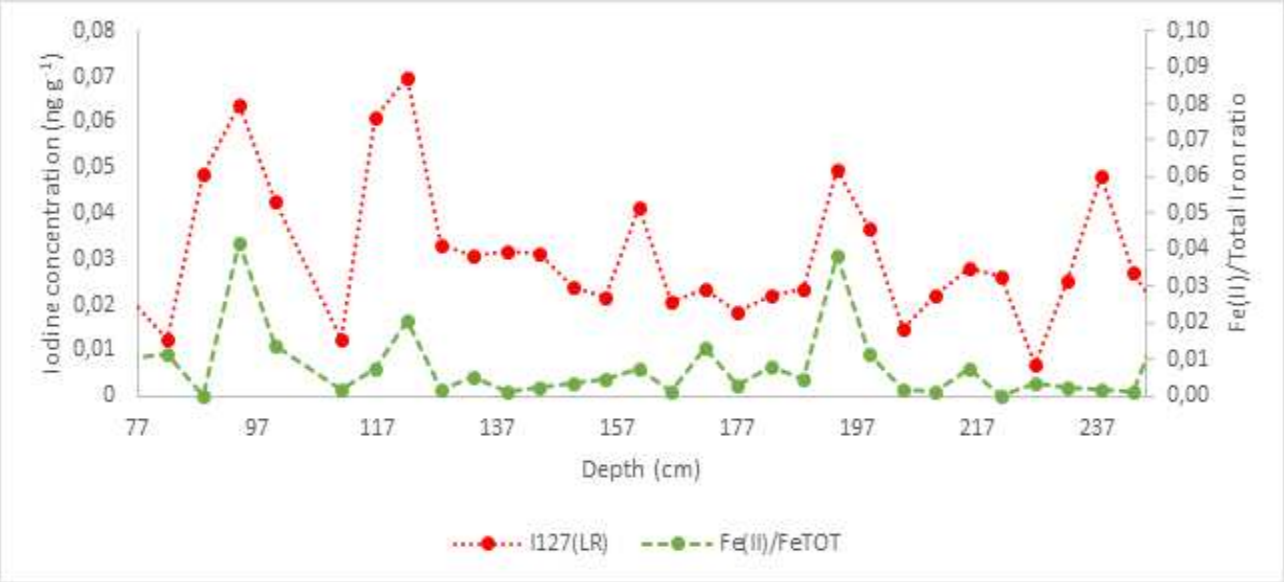

Figure 38 - Iodine profile (red curve) and $Fe^{2+}/FeTOT$ ratio profile (green line) from between 77 cm to 245 cm. A significant correlation (r = 0.537) was found.

4.2 Fe^{2+} profile, iodine and organic compounds contribution on the Holtedahlfonna glacier

Fe^{2+}, iodine and organic ligands quantification was performed on the Holtedahlfonna shallow ice core. The average Fe^{2+} concentration (54 pg g^{-1}) was slightly higher than the one recorded in Dome C, while the Fe^{2+} fraction over the total iron was lower (0.8%) than the one recorded in Dome C (3.3%) and comparable with the one obtained from another Greenland ice core (Burgay et al., 2018).

Iodine showed a concentration that ranged from between 2 pg g^{-1} to 56 pg g^{-1} with an average value of 15 ± 9 pg g^{-1}, lower than the one detected on the Holtedahlfonna glacier. As for Dome C, we investigated the role of Iodine in solubilising the Fe from the lattice to the soluble Fe^{2+} form. We evaluated how the $Fe^{2+}/Fe_{(tot)}$ ratio changed with respect to the iodine concentration and we did not find any significant correlation (r =

0.090) between these two variables suggesting that other mechanisms might be involved in the solubilisation of the Fe^{2+} species. Since in the Arctic snow and ice the amount of organic ligands is up to 2 order of magnitudes higher than the one recorded in Antarctica (Legrand and Saigne, 1988) and liquid water is present during summertime, we investigated their role in solubilizing Fe from the lattice as proposed by Kim et al., 2010. We did not find any significant correlation between the $Fe^{2+}/Fe_{(tot)}$ ratio and the organic ligands we identified: Formate (r = -0.035), Acetate (r = 0.163) and Glycolate (r = 0.038). However, we found a significant correlation between the absolute Fe^{2+} concentration and Formate (r = 0.448), Acetate (r = 0.512) and Glycolate (r = 0.376). In Figure 39 we show the profile for both Fe^{2+} (green) and acetate (yellow). The possible explanations might be linked either to the mineralogy of the iron oxides in the ice core (e.g. hematite did not show any photoreductive dissolution under laboratory conditions, Kim et al., 2010), or to the fact that organic ligands, acting as electron donors, can reduce the already soluble Fe^{3+} species (Baker and Croot, 2010). Moreover, considering that: 1) specific organic ligands, such as acetate, are also key intermediates in the bacterial anaerobic degradation of the organic matter (Ljungdhal, 1986), 2) microorganisms inhabit glaciers (Boetius et al., 2015) and that, 3) melt ponds caused by strong solar radiation might favour the development of bacteria on the glaciers (Pittino et al., 2018); a possible alternative interpretation of the results might be related to the oxidation of the organic matter paired with the Fe^{3+} respiration in anoxic environments by bacteria (Schlesinger and Bernhardt, 2013). The high concentration of acetate (147 ng g^{-1}) at 850 cm depth, which correspond to more than ten-fold higher than the typical organic ligands concentration in Greenland (Legrand and De Angelis, 1996) and 8-fold higher than the average acetate value (25 ng g^{-1}), might endorse this hypothesis.

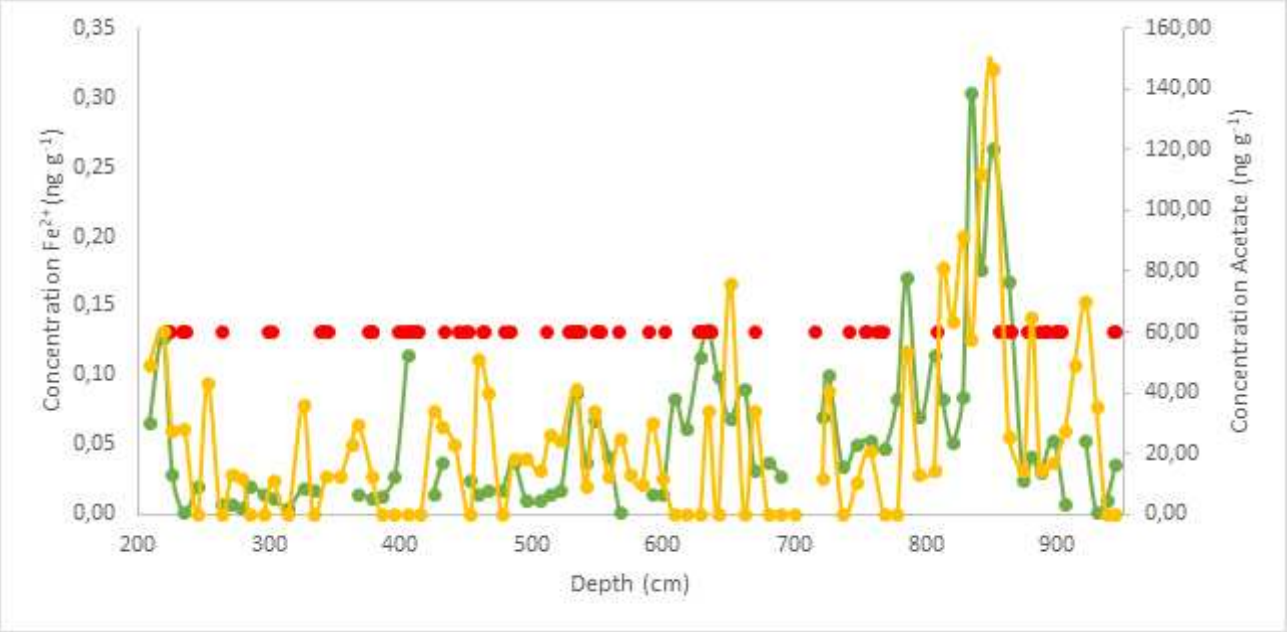

Figure 39 - Fe^{2+} (green) and acetate (yellow) profile for the shallow Holtedahlfonna ice core. Red dots: ice lenses

4.3 Preliminary conclusions and future perspectives

This study represents the first attempt to describe the Fe^{2+} behaviour in snow and ice on two different locations: Svalbard Islands and Antarctica. The results suggested that on the Antarctic plateau, iodine might play a significant role in reducing the unsoluble Fe from the lattice to Fe^{2+}. Considering that the unsoluble iron is mainly present as Fe_2O_3 (Baccolo et al., 2018), the redox reaction between iron oxides from the lattice and iodine (Kim et al., 2018) might be a plausible explanation of this finding. The Holtedahlfonna shallow core exhibited completely different features with lower concentration of iodine and two orders of magnitude more organic ligands such as acetate, formate and glycolate. In this core, we did not detect any correlation between iodine and the $Fe^{2+}/Fe_{(tot)}$ ratio, while we observed that organic ligands might play a role in keeping Fe^{2+} in the soluble form. Even though it is well known that organic ligands might stabilize Fe^{2+} species (Baker and Croot, 2010), it has never been detected on the Arctic firn. Considering that the Holtedahlfonna shallow core showed several ice lenses suggesting significant surface snow melting, the high concentration of acetate and glycolate, together with the increase in Fe^{2+} concentration, might also suggest the presence of anaerobic bacterial respiration of the organic matter in the melt ponds that form during summer on the glacier surface.

To conclude, future studies are needed to better quantify the role of iodine and organic ligands in other matrices (e.g. sea-ice, icebergs…) to evaluate to what extent these processes might increase the bioavailable iron supply directly to the oceans. Moreover, we suggest performing soluble Fe^{2+} and Fe^{3+} quantification, mineralogical evaluation of the iron oxides present in the ice/snow and a microbiological investigation to have a greater insight on the role of organic ligands on iron speciation and on their sources.

5.

Conclusions and future perspectives

5.1 Conclusions and future perspectives

During my PhD I developed and optimized three analytical methods and I first applied them on four different ice and snow matrices. The CFA-CL method able to detect Fe^{2+} at pg g^{-1} levels represents now a reliable approach to detect past volcanic eruptions in ice cores with higher resolution and higher sensitivity than the traditional sulphate method. The first application on the B17 ice core allowed us to detect 7 past volcanic eruptions. When it was applied on the EGRIP core, together with continuous pH data, we were able to detect the last 3000 years of volcanic eruptions. The optimization and the first application on about 300 meters of the EGRIP ice core of the continuous total soluble iron method, represents another important achievement. Indeed, this method can provide useful information about actual iron bioavailability and, together with Fe^{2+} data can be useful to understand, together with other proxies, how it changed in the last millennia. The soluble aluminium method represents an alternative approach to evaluate and to understand dust transport and can be used, together with the other two methods, as a complementary proxy to detect past volcanic eruptions.

Finally, the study about transport and post-depositional processes involving Fe species, represents a first step towards the understanding of the main factors that might affect Fe solubility. We observed that in Antarctica, Iodine species, more than organic ligands, might favour Fe solubility (from the lattice to the solution). In contrast, in Svalbard we observed a completely different behaviour. Being organic ligands 2-3 order of magnitudes more concentrated, they might play a major role in regulating Fe^{2+} solubility, while iodine species did not show any appreciable contribution in reducing Fe(III) to soluble Fe^{2+}. Since the presence of Fe binding species in seawater is a crucial parameter for its solubility, better understanding organic ligands behaviour and sources is critical to assess and quantify the actual Fe bioavailability. However, further studies to clarify transport mechanisms that might affect Fe speciation are needed. The main limitation of our pioneering study was related to the bad quality of the ice core, thus analyses on better preserved ice (e.g. from Greenland or Antarctica) are required together with the quantification of other compounds (e.g. hydrogen peroxide) that might influence the equilibrium between Fe^{3+} and Fe^{2+} species.

The results I obtained represent a first step towards a new research field topic in ice core science such as the multidisciplinary study of the potential role of volcanic eruptions in fertilizing the HNLC regions. Furthermore, with the next EGRIP melting campaign (January-April 2019) we will finally achieve the complete Fe speciation on an polar ice core for the last 12 kyrs, with a particular emphasis on the last 200 years evaluating the anthropogenic contribution to iron species in the atmosphere.

Finally, in view of the next EPICA Oldest Ice drilling, the CFA-CL method represents a possible alternative for volcano detection to the traditional sulphate methods that, if applied to ice older than 400 kyrs, fail, although it would not provide a quantitative sulfate flux estimate and therefore no estimate of the sulphate radiative forcing in the stratosphere. Therefore, it will be extremely important to test the method on old ice to see if it represents still a reliable approach to detect past volcanic eruptions.

5.2 Summary of the activities

Iron is a key element of the Earth system since it can fertilize the so-called High-Nutrient Low-Chlorophyll oceans, enhancing their productivity. During my PhD thesis I developed a new method to detect soluble Fe^{2+} species in ice cores. Furthermore, I optimized a method to detect total soluble iron in ice cores. I applied both methods on a Greenland ice core (B17) and I found that Fe^{2+} species can be used as a reliable proxy to detect past volcanic eruptions.

5.2.1 Periods abroad

Period	Institution	Country	Supervisor	Activities
10/2015	Centre for Ice and Climate	Denmark	Paul Vallelonga	Ice Core melting
12/2016	Centre for Ice and Climate	Denmark	Paul Vallelonga	Ice Core melting
03/2017	Centre for Ice and Climate	Denmark	Paul Vallelonga	Ice Core melting
04/2017	Norwegian Polar Institute	Svalbard Islands	Andrea Spolaor	Field activity
09-10/2017	University of Bern	Switzerland	Hubertus Fischer	Ice Core melting
02-03/2018	University of Bern	Switzerland	Hubertus Fischer	Ice Core melting
04/2018	Universidad de Las Palmas de Gran Canaria	Spain	Juana Magdalena Santana Gonzalez	Discrete analyses with luminol technique
06/2018	European Synchrotrone Facility	France	Francesco D'Acapito	Milled rocks and filtered snow analyses

5.2.2 Projects

Project	Role	Fundings
Iron Speciation in Svalbard Ice Core and Snow (ISSICOS)	Project Owner	EUR 8.000
EGRIP	Participant	-
Ice Memory	Participant	-

5.2.3 Summer Schools

Date	Title	Location
09/2017	ICAT Summer School	Centre for Ice and Climate. Copenhagen, Denmark

5.2.4 Seminars and Conferences

Date	Title	Location
10/03/2017	Meeting Ice Memory	UNESCO, Paris
05/06/2017	Memory of an ice core	OAC-INAF, Cagliari
28/09/2017	Ice Memory	UNESCO, Paris
01/12/2017	Saving the Earth's climate history	Antarctic Day, Ca' Foscari, Venice
17/04/2018	Fe^{2+} as a new potential proxy to detect past volcanic eruptions	Universidad de las Palmas de Gran Canaria, Telde, Spain
17/10/2018	Fe^{2+} as a new potential proxy to detect past volcanic eruptions	6th SISC Conference, Venice

5.2.5 Publications

Burgay, F.*, Erhardt, T., Della Lunga, D., Jensen, C. M., Spolaor, A., Vallelonga, P., Fischer H., & Barbante, C. (2018). Fe^{2+} in ice cores as a new potential proxy to detect past volcanic eruptions. *Science of The Total Environment.* (* Corresponding author)

Vecchiato M., Barbaro E., Spolaor A., **Burgay F.,** Barbante C., Piazza R., Gambaro A., *Fragrances and PAHs in snow and seawater of Ny-Ålesund (Svalbard): Local and long-range contamination.* Environmental Pollution, 2018.

5.2.5.1 Upcoming publications

Burgay F.*, Spolaor A., Barbaro E., Isaksson E., Gallet J.C., Stenni B., Dreossi G., Saiz-Lopez A., Kim K., Barbante C., *Iron transport and post-depositional processes on snow and ice: a preliminary study.* Geophysical Research Letters. *Submitted.* (* Corresponding author)

5.2.6 Other activities

Date	Activity	Location
07/2017	Tutoring and teaching activities at the Ca' Foscari - Harvard Summer School for the course "Earth's Climate" held by Prof. Carlo Barbante	Venice
11/09/2017	Organizing Committee Member, Workshop "Science Communication and Social Media". PAIS Conference	Trieste
29/09/2017	Co-organizer of the "Veneto Night"	Venice
01/12/2017	Co-organizer of the "Antarctic Day"	Venice
06/2018	Teaching activity on Climate Change and Palaeoclimate reconstructions *(6 hours)*	Lancenigo
07/2018	Tutoring and teaching activities at the Ca' Foscari - Harvard Summer School for the course "Earth's Climate" held by Prof. Carlo Barbante	Venice
09/2018	Coordination and support for the organization of the scientific exhibition "Artico" at the Scientific Campus (Mestre)	Venice
09/2018	Participant at the "Veneto Night"	Venice
10/2018	Co-organizer of the exhibition "Artico – Viaggio interattivo al Polo Nord"	Venice

APPENDIX A

Preliminary Results from the EGRIP core

A.1 Introduction

CFA analyses on the EGRIP ice core from Northeast Greenland represents the first opportunity to test the total soluble iron and the Fe^{2+} methods in order to reconstruct both the evolution of Fe solubility and to perform paleovolcanic reconstructions over a millennial time scale. To melt the whole core (approximately 2550 m long), three or four melting campaigns are needed. In 2017, the first 350 meters were melted (14%) covering approximately the last 3000 years of Earth history. The aim of the project is to obtain a high-resolution climate record of impurities (besides greenhouse gasses and water isotopes) of the last 25.000 years, covering in particular the entire present interglacial. In this chapter, we present the first continuous data about total soluble Fe, with some highlights related to specific volcanic eruptions where Fe^{2+} data are shown as well. These preliminary data will be integrated with conductivity, dust, pH, trace elements (ICP-TOF-MS) and discrete sulphate data together with a more precise dating.

A.2 Selected volcanic eruption: *Eldjà* volcanic eruption

In the following, we present the total soluble iron profile for some selected volcanic eruptions. In particular we present the Fe^{2+} data and the soluble iron data for the Eldjà eruption (940 AD) which is considered the largest eruption that happened in Iceland during the Common Era (Oppenheimer et al., 2018). I am quite confident to attribute the signal to the Eldjà volcano because it was the strongest eruption that happened in the estimated period associated to the ice core depth. The Eldjà eruption triggered one of the coolest summer of the last 1500 years, as suggested by tree rings, especially in Central Europe, Scandinavia, Alaska and Central Asia with summer average temperatures 2°C lower than the average of that period.

First results from Fe^{2+} and total soluble Fe method suggested that the eruption caused an increase in soluble iron deposition on the ice. The recorded values were the highest ever recorded in this first melting campaign: 16.9 ng g^{-1} for the total soluble Fe and 3.8 ng g^{-1} for Fe^{2+} (Figure 40).

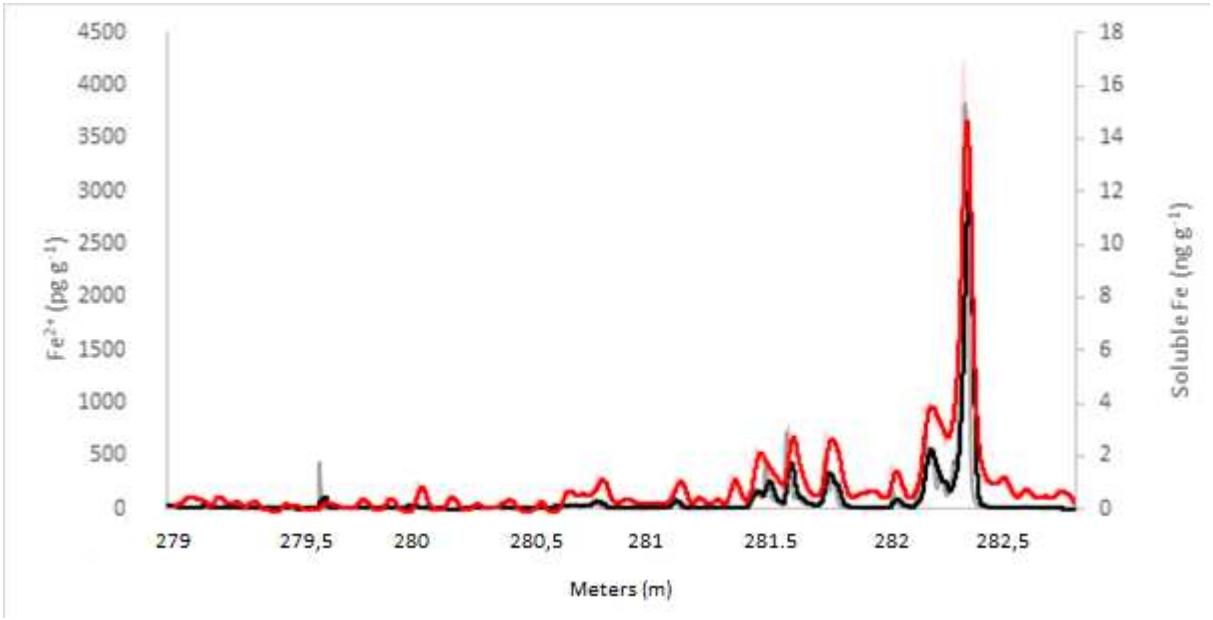

Figure 40 - Soluble Iron (red line) and Fe^{2+} (black line) profiles for bag 342-347 where the Eldjà eruption likely occurred (940 AD).

A.3 Other volcanic eruptions

During the core analysis, several other volcanic eruptions were identified. Up to now, however, it is difficult to attribute the signal to a specific volcanic event in absence of any other proxy and precise dating. The strongest volcanic eruptions in terms of Fe^{2+} concentration are reported in Figure 41 and Figure 42.

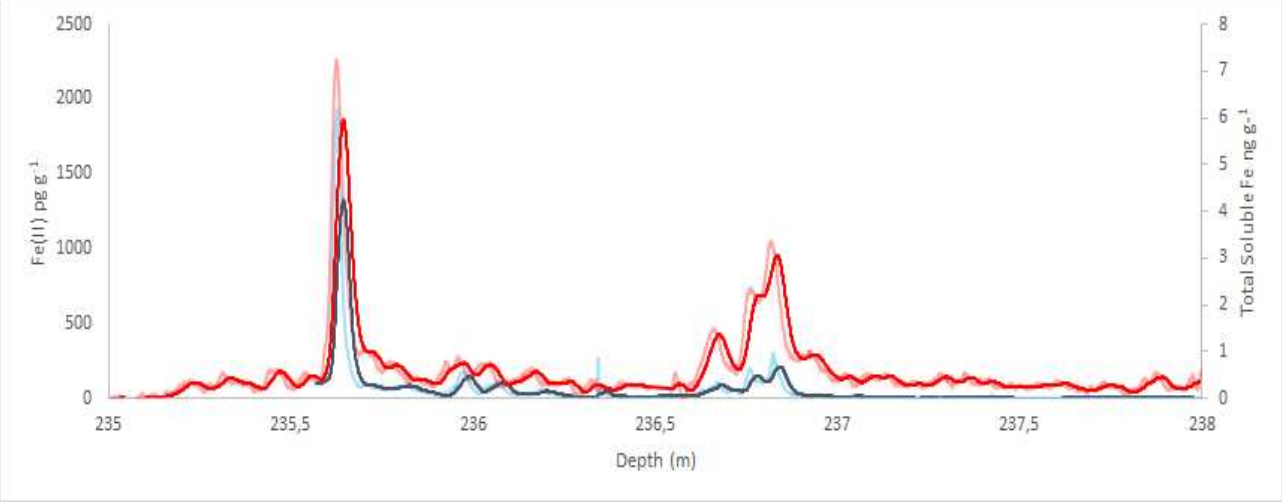

Figure 41 - Soluble Iron (red line) and Fe^{2+} (black line) profiles for bag 427-432 where at least two strong eruptions in terms of Fe^{2+} concentration occurred.

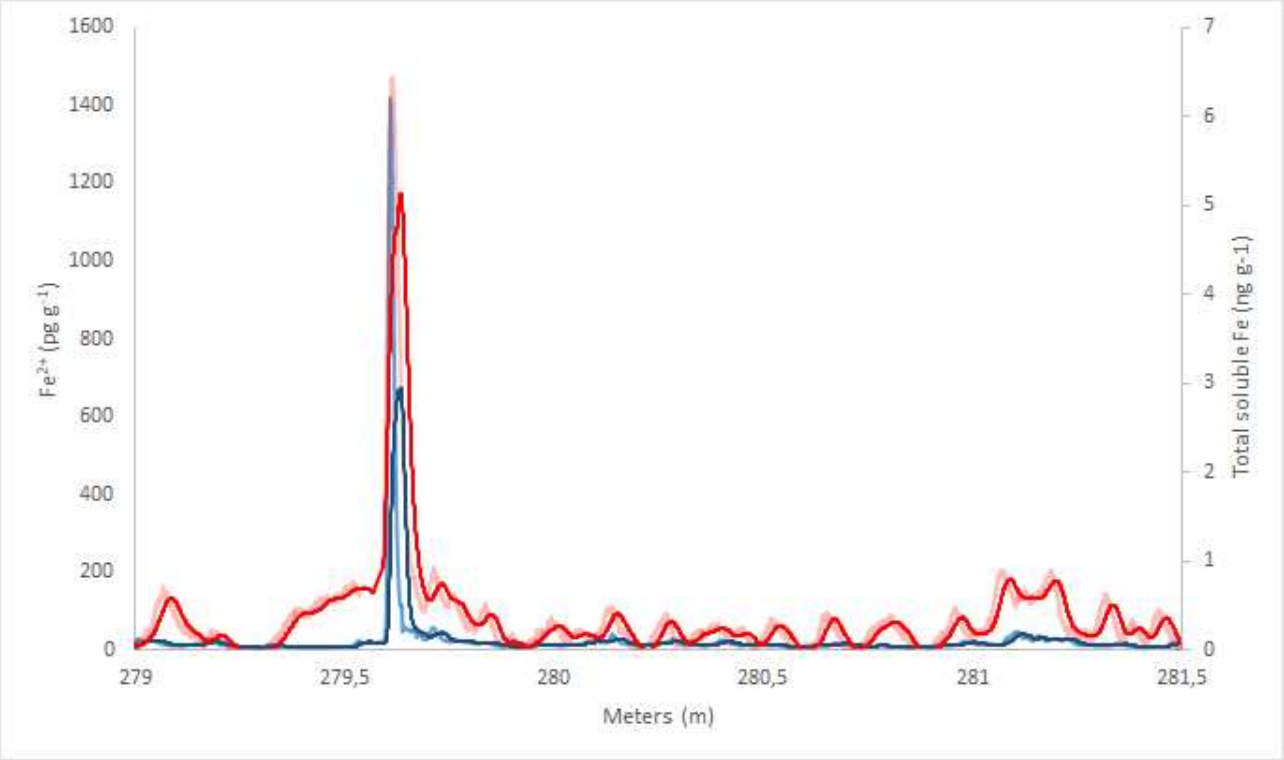

Figure 42 - Soluble Iron (red line) and Fe^{2+} (black line) profiles for bag 507-512 where a strong eruption in terms of Fe^{2+} concentration occurred.

5.4 Soluble iron long-term concentration trend

Unfortunately, because of different issues in the set-up of the method, continuous measurements of total soluble Fe only started from bag 128 (70 meters depth). However, from the next melting campaign on, which will begin in 2019, one shallow core covering the last 600 years will be melted and it will be possible to acquire the missing data. The goal for this new melting campaign will be both to understand if an increase in total soluble iron is recorded from the Industrial Revolution to the present and to provide the first complete reconstruction of volcanic eruptions through the new Fe^{2+} proxy for the last six centuries.

In this paragraph, the complete total soluble Fe for the last 3000 years is shown (Figure 44). As already highlighted on the B17 ice core, total soluble iron shows a seasonal cycle (Figure 43) with values that range from the LoD up to 1.5 ng g^{-1}. The average total soluble Fe concentration in the considered time interval is 0.5 ng g^{-1} ± 0.55 ng g^{-1} with no significant increase in total soluble iron concentration. Coupling these data with total Fe concentration determined by ICP-TOF-MS, it will be possible to understand how the soluble fraction has evolved as a function of temperature and other parameters. However, the main objective is to show that total soluble iron measurements, as well as Fe^{2+} quantification, are feasible and reliable over 2 months-long

melting campaign. The climate interpretation of these data requires the integration of different ice core proxy parameters that, to date, are not yet fully available from the EGRIP ice core.

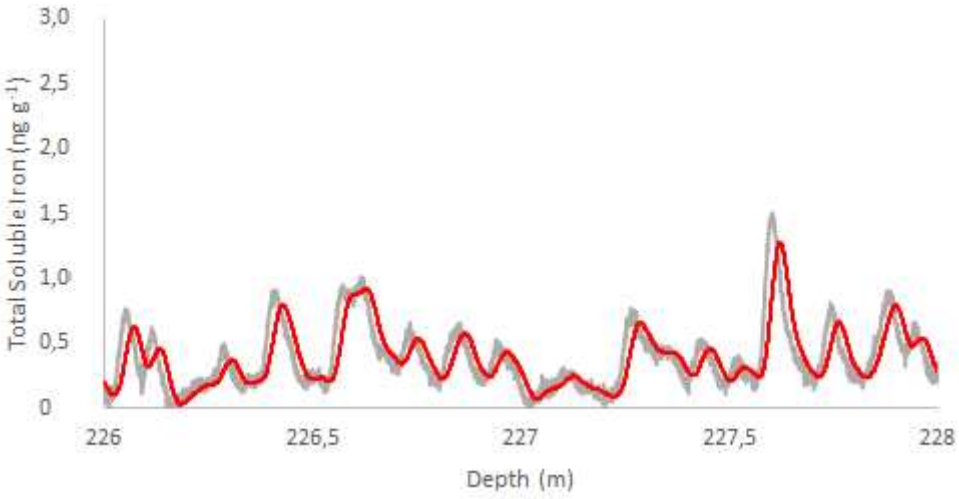

Figure 43 – Selected frame from 226 m to 228 meters depth that shows the seasonal-like profile of the total soluble Fe

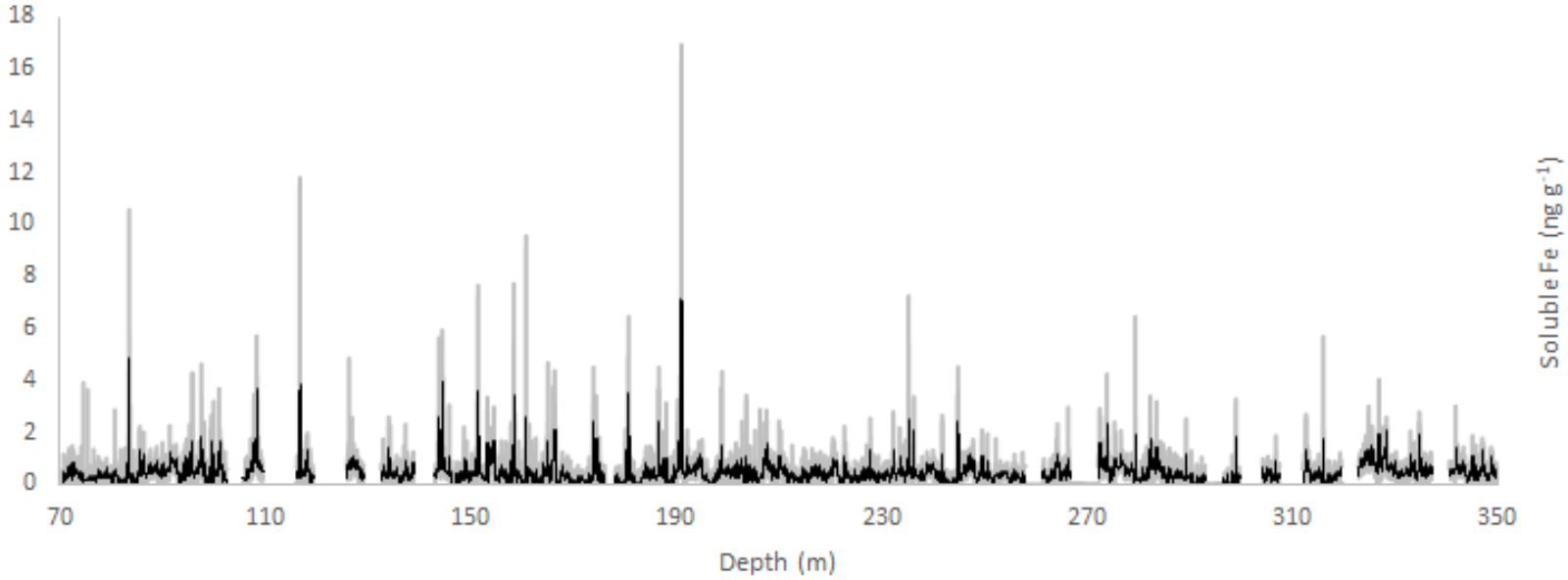

Figure 44 - Total soluble Fe profile from 70 meters to 350 meters depth

AKNOWLEDGMENTS

The PhD represents the first scientific challenge you are asked to tackle. It is also an individual challenge: you, your methods, your failures and your successes. However, during these 3 years-journey I met many people that supported me from the beginning until the end. Everyone with his specific role.

I had the chance to have Prof. Carlo Barbante and Andrea Spolaor as a tutor and co-tutor respectively. I think it is very difficult to find so helpful and enthusiastic people. I am so glad having them as my scientific references. During my PhD, I also met Paul Vallelonga and Helle Kjaer that were fundamental to teach me how a CFA system works. I can remember my first experience with the CFA in Copenhagen: I was so terrified by all these tubes, pumps, reagents, colours. With their help, I started to make some order in my mind.

The B17 ice core, melted in Bern, represented the first benchmark for me and my methods. The success obtained in that campaign has been the most important results during my PhD. In this occasion, the suggestions and the availability of Tobias Erhardt were crucial. We can say that in Bern my methods went from an alpha-phase to a beta-phase. Thanks also to Hubertus Fischer who, through precious suggestions, helped me a lot in optimizing the first paper I wrote about the Fe^{2+} method.

If B17 was the first experience with the continuous determination of Fe^{2+} and Fe^{3+}, the main one was EGRIP. In that occasion the "Italian Team" composed by me, Federico Scoto and Ilaria Crotti, obtained a very important result with the continuous iron speciation of the first 350 meters of the ice-core. I adopted also Sophie Darfeuil (from France) and I thank her a lot for staying in the lab until midnight sometimes.

However, this journey does not finish with the PhD. Many scientific challenges are waiting for me and I finally thank Carlotta Dentico that, maybe unawares, presented me other scientists interested in the volcanic impacts on climate. Maybe I will continue with this kind of research only because we casually met during the "Artico-exhibition"!

Finally yet importantly, all my family that supported me at every time: when I was demotivated and when I was motivated. Sometimes I couldn't stand me, but they could. It was not easy, I have to recognize it.

A PhD is an individual challenge. During this challenge, you have the opportunity to meet different people with different expertises that might improve the idea you have. Maybe a simple acknowledgment is not enough, but you were all fundamental: thanks!

REFERENCES

Achterberg EP, Holland TW, Bowie AR, Mantoura RFC, Worsfold PJ. Determination of iron in seawater. Analytica Chimica Acta 2001; 442: 1-14.

Achterberg EP, Moore CM, Henson SA, Steigenberger S, Stohl A, Eckhardt S, et al. Natural iron fertilization by the Eyjafjallajökull volcanic eruption. Geophysical Research Letters 2013; 40: 921-926.

Arrigo KR, van Dijken G, Pabi S. Impact of a shrinking Arctic ice cover on marine primary production. Geophysical Research Letters 2008; 35.

Baccolo G, Cibin G, Delmonte B, Hampai D, Marcelli A, Di Stefano E, et al. The Contribution of Synchrotron Light for the Characterization of Atmospheric Mineral Dust in Deep Ice Cores: Preliminary Results from the Talos Dome Ice Core (East Antarctica). Condensed Matter 2018; 3: 25.

Baker AR, Croot PL. Atmospheric and marine controls on aerosol iron solubility in seawater. Marine Chemistry 2010; 120: 4-13.

Barbante C, Bellomi T, Mezzadri G, Cescon P, Scarponi G, Morel C, et al. Direct determination of heavy metals at picogram per gram levels in Greenland and Antarctic snow by double focusing inductively coupled plasma mass spectrometry. Journal of analytical atomic spectrometry 1997; 12: 925-931.

Bigler M, Wagenbach D, Fischer H, Kipfstuhl J, Miller H, Sommer S, et al. Sulphate record from a northeast Greenland ice core over the last 1200 years based on continuous flow analysis. Annals of Glaciology 2002; 35: 250-256.

Blau F. Über neue organische Metallverbindungen. Monatshefte für Chemie und verwandte Teile anderer Wissenschaften 1898; 19: 647-689.

Boetius A, Anesio AM, Deming JW, Mikucki JA, Rapp JZ. Microbial ecology of the cryosphere: sea ice and glacial habitats. Nature Reviews Microbiology 2015; 13: 677.

Bory A-M, Biscaye PE, Svensson A, Grousset FE. Seasonal variability in the origin of recent atmospheric mineral dust at NorthGRIP, Greenland. Earth and Planetary Science Letters 2002; 196: 123-134.

Bowie AR, Achterberg EP, Sedwick PN, Ussher S, Worsfold PJ. Real-time monitoring of picomolar concentrations of iron (II) in marine waters using automated flow injection-chemiluminescence instrumentation. Environmental science & technology 2002; 36: 4600-4607.

Boyd P, Ellwood M. The biogeochemical cycle of iron in the ocean. Nature Geoscience 2010; 3: 675.

Buesseler KO, Andrews J, Pike SM, Charette MA, Goldson LE, Brzezinski MA, et al. Particle export during the southern ocean iron experiment (SOFeX). Limnology and Oceanography 2005; 50: 311-327.

Burgay F, Erhardt T, Della Lunga D, Jensen CM, Spolaor A, Vallelonga P, et al. Fe2+ in ice cores as a new potential proxy to detect past volcanic eruptions. Science of The Total Environment 2018.

Butler JH. The potential role of the ocean in regulating atmospheric CH3Br. Geophysical research letters 1994; 21: 185-188.

Cather SM, Dunbar NW, McDowell FW, McIntosh WC, Scholle PA. Climate forcing by iron fertilization from repeated ignimbrite eruptions: The icehouse–silicic large igneous province (SLIP) hypothesis. Geosphere 2009; 5: 315-324.

Chan K, Jiang S, Ning Z. Speciation of water soluble iron in size segregated airborne particulate matter using LED based liquid waveguide with a novel dispersive absorption spectroscopic measurement technique. Analytica chimica acta 2016; 914: 100-109.

Chiapello I, Moulin C, Prospero JM. Understanding the long-term variability of African dust transport across the Atlantic as recorded in both Barbados surface concentrations and large-scale Total Ozone Mapping Spectrometer (TOMS) optical thickness. Journal of Geophysical Research: Atmospheres 2005; 110.

Croot PL, Laan P. Continuous shipboard determination of Fe (II) in polar waters using flow injection analysis with chemiluminescence detection. Analytica Chimica Acta 2002; 466: 261-273.

D'Arrigo R, Wilson R, Tudhope A. The impact of volcanic forcing on tropical temperatures during the past four centuries. Nature Geoscience 2009; 2: 51.

Dai J, Mosley-Thompson E, Thompson LG. Ice core evidence for an explosive tropical volcanic eruption 6 years preceding Tambora. Journal of Geophysical Research: Atmospheres 1991; 96: 17361-17366.

de Baar HJ. Distributions, sources and sinks of iron in seawater. The biogeochemistry of iron in seawater 2001: 123-253.

De Silva SL, Zielinski GA. Global influence of the AD 1600 eruption of Huaynaputina, Peru. Nature 1998; 393: 455.

de Vernal A, Gersonde R, Goosse H, Seidenkrantz M-S, Wolff EW. Sea ice in the paleoclimate system: the challenge of reconstructing sea ice from proxies–an introduction. Quaternary Science Reviews 2013; 79: 1-8.

Duggen S, Olgun N, Croot P, Hoffmann LJ, Dietze H, Delmelle P, et al. The role of airborne volcanic ash for the surface ocean biogeochemical iron-cycle: a review. Biogeosciences (BG) 2010; 7: 827-844.

Duprat LP, Bigg GR, Wilton DJ. Enhanced Southern Ocean marine productivity due to fertilization by giant icebergs. Nature Geoscience 2016; 9: 219.

Elrod VA, Johnson KS, Coale KH. Determination of subnanomolar levels of iron (II) and total dissolved iron in seawater by flow injection and analysis with chemiluminescence detection. Analytical Chemistry 1991; 63: 893-898.

Emmenegger L, King DW, Sigg L, Sulzberger B. Oxidation kinetics of Fe (II) in a eutrophic Swiss lake. Environmental Science & Technology 1998; 32: 2990-2996.

Evan AT, Mukhopadhyay S. African dust over the northern tropical Atlantic: 1955–2008. Journal of Applied Meteorology and Climatology 2010; 49: 2213-2229.

Fraile-Nuez E, González-Dávila M, Santana-Casiano JM, Arístegui J, Alonso-González IJ, Hernández-León S, et al. The submarine volcano eruption at the island of El Hierro: physical-chemical perturbation and biological response. Scientific Reports 2012; 2: 486.

Frajka-Williams E, Rhines PB. Physical controls and interannual variability of the Labrador Sea spring phytoplankton bloom in distinct regions. Deep Sea Research Part I: Oceanographic Research Papers 2010; 57: 541-552.

Gabrielli P, Barbante C, Plane JM, Boutron CF, Jaffrezo JL, Mather TA, et al. Siderophile metal fallout to Greenland from the 1991 winter eruption of Hekla (Iceland) and during the global atmospheric perturbation of Pinatubo. Chemical Geology 2008; 255: 78-86.

Gaspari V, Barbante C, Cozzi G, Cescon P, Boutron CF, Gabrielli P, et al. Atmospheric iron fluxes over the last deglaciation: Climatic implications. Geophysical Research Letters 2006; 33.

Gerringa LJ, Alderkamp A-C, Laan P, Thuroczy C-E, De Baar HJ, Mills MM, et al. Iron from melting glaciers fuels the phytoplankton blooms in Amundsen Sea (Southern Ocean): Iron biogeochemistry. Deep Sea Research Part II: Topical Studies in Oceanography 2012; 71: 16-31.

Hansard SP, Landing WM. Determination of iron (II) in acidified seawater samples by luminol chemiluminescence. Limnology and Oceanography: Methods 2009; 7: 222-234.

Harvey Jr AE, Smart JA, Amis E. Simultaneous spectrophotometric determination of iron (II) and total iron with 1, 10-phenanthroline. Analytical Chemistry 1955; 27: 26-29.

Hawkings JR, Wadham JL, Tranter M, Raiswell R, Benning LG, Statham PJ, et al. Ice sheets as a significant source of highly reactive nanoparticulate iron to the oceans. Nature communications 2014; 5: 3929.

Haygood MG, Holt PD, Butler A. Aerobactin production by a planktonic marine Vibrio sp. Limnology and Oceanography 1993; 38: 1091-1097.

Hendriks L, Gundlach-Graham A, Hattendorf B, Günther D. Characterization of a new ICP-TOFMS instrument with continuous and discrete introduction of solutions. Journal of Analytical Atomic Spectrometry 2017; 32: 548-561.

Hiscock WT, Fischer H, Bigler M, Gfeller G, Leuenberger D, Mini O. Continuous flow analysis of labile iron in ice-cores. Environmental science & technology 2013; 47: 4416-4425.

Hoffmann T, O'Dowd CD, Seinfeld JH. Iodine oxide homogeneous nucleation: An explanation for coastal new particle production. Geophysical Research Letters 2001; 28: 1949-1952.

Hopwood MJ, Bacon S, Arendt K, Connelly D, Statham P. Glacial meltwater from Greenland is not likely to be an important source of Fe to the North Atlantic. Biogeochemistry 2015; 124: 1-11.

Hudson RJ, Morel FM. Iron transport in marine phytoplankton: Kinetics of cellular and medium coordination reactions. Limnology and Oceanography 1990; 35: 1002-1020.

Huybers P, Langmuir C. Feedback between deglaciation, volcanism, and atmospheric CO2. Earth and Planetary Science Letters 2009; 286: 479-491.

Hydes D, Liss P. Fluorimetric method for the determination of low concentrations of dissolved aluminium in natural waters. Analyst 1976; 101: 922-931.

Iida T, Saitoh S-I. Temporal and spatial variability of chlorophyll concentrations in the Bering Sea using empirical orthogonal function (EOF) analysis of remote sensing data. Deep Sea Research Part II: Topical Studies in Oceanography 2007; 54: 2657-2671.

Jeong D, Kim K, Choi W. Accelerated dissolution of iron oxides in ice. Atmospheric Chemistry and Physics 2012; 12: 11125-11133.

Jickells T, An Z, Andersen KK, Baker A, Bergametti G, Brooks N, et al. Global iron connections between desert dust, ocean biogeochemistry, and climate. science 2005; 308: 67-71.

Kanna N, Toyota T, Nishioka J. Iron and macro-nutrient concentrations in sea ice and their impact on the nutritional status of surface waters in the southern Okhotsk Sea. Progress in Oceanography 2014; 126: 44-57.

Kaufmann PR, Federer U, Hutterli MA, Bigler M, Schüpbach S, Ruth U, et al. An improved continuous flow analysis system for high-resolution field measurements on ice cores. Environmental science & technology 2008; 42: 8044-8050.

Kawamura K, Ng LL, Kaplan IR. Determination of organic acids (C1-C10) in the atmosphere, motor exhausts, and engine oils. Environmental science & technology 1985; 19: 1082-1086.

Kesselmeier J, Staudt M. Biogenic volatile organic compounds (VOC): an overview on emission, physiology and ecology. Journal of atmospheric chemistry 1999; 33: 23-88.

Kim K, Choi W, Hoffmann MR, Yoon H-I, Park B-K. Photoreductive dissolution of iron oxides trapped in ice and its environmental implications. Environmental science & technology 2010; 44: 4142-4148.

King DW. Role of carbonate speciation on the oxidation rate of Fe (II) in aquatic systems. Environmental Science & Technology 1998; 32: 2997-3003.

King DW, Lounsbury HA, Millero FJ. Rates and mechanism of Fe (II) oxidation at nanomolar total iron concentrations. Environmental science & technology 1995; 29: 818-824.

Kinnard C, Zdanowicz CM, Koerner RM, Fisher DA. A changing Arctic seasonal ice zone: Observations from 1870–2003 and possible oceanographic consequences. Geophysical Research Letters 2008; 35.

Kirchman DL. Oceanography: microbial ferrous wheel. Nature 1996; 383: 303-304.

Kjær HA, Vallelonga P, Svensson A, Elleskov L. Kristensen M, Tibuleac C, Winstrup M, et al. An optical dye method for continuous determination of acidity in ice cores. Environmental Science & Technology 2016; 50: 10485-10493.

Knüsel S, Piguet DE, Schwikowski M, Gäggeler HW. Accuracy of continuous ice-core trace-element analysis by inductively coupled plasma sector field mass spectrometry. Environmental science & technology 2003; 37: 2267-2273.

Kozak J, Gutowski J, Kozak M, Wieczorek M, Kościelniak P. New method for simultaneous determination of Fe (II) and Fe (III) in water using flow injection technique. Analytica chimica acta 2010; 668: 8-12.

Kustka A, Sañudo-Wilhelmy S, Carpenter EJ, Capone DG, Raven JA. A revised estimate of the iron use efficiency of nitrogen fixation, with special reference to the marine cyanobacterium Trichodesmium spp.(Cyanophyta) 1. Journal of Phycology 2003; 39: 12-25.

Lambert F, Delmonte B, Petit J-R, Bigler M, Kaufmann PR, Hutterli MA, et al. Dust-climate couplings over the past 800,000 years from the EPICA Dome C ice core. Nature 2008; 452: 616.

Langmann B, Zakšek K, Hort M, Duggen S. Volcanic ash as fertiliser for the surface ocean. Atmospheric Chemistry and Physics 2010; 10: 3891-3899.

Lannuzel D, De Jong J, Schoemann V, Trevena A, Tison J-L, Chou L. Development of a sampling and flow injection analysis technique for iron determination in the sea ice environment. Analytica Chimica Acta 2006; 556: 476-483.

Lannuzel D, Vancoppenolle M, van der Merwe P, de Jong J, Meiners K, Grotti M, et al. Iron in sea ice: Review and new insights. Elem Sci Anth 2016; 4.

Legrand M, De Angelis M. Light carboxylic acids in Greenland ice: A record of past forest fires and vegetation emissions from the boreal zone. Journal of Geophysical Research: Atmospheres 1996; 101: 4129-4145.

Legrand M, McConnell J, Fischer H, Wolff EW, Preunkert S, Arienzo M, et al. Boreal fire records in Northern Hemisphere ice cores: a review. Climate of the Past 2016; 12: 2033-2059.

Legrand M, Preunkert S, Wagenbach D, Cachier H, Puxbaum H. A historical record of formate and acetate from a high-elevation Alpine glacier: Implications for their natural versus anthropogenic budgets at the European scale. Journal of Geophysical Research: Atmospheres 2003; 108.

Legrand M, Saigne C. Formate, acetate and methanesulfonate measurements in Antarctic ice: some geochemical implications. Atmospheric Environment (1967) 1988; 22: 1011-1017.

Ljungdhal L. The autotrophic pathway of acetate synthesis in acetogenic bacteria. Annual Reviews in Microbiology 1986; 40: 415-450.

Longpré MA, Stix J, Burkert C, Hansteen T, Kutterolf S. Sulfur budget and global climate impact of the AD 1835 eruption of Cosigüina volcano, Nicaragua. Geophysical Research Letters 2014; 41: 6667-6675.

Lupker M, Aciego SM, Bourdon B, Schwander J, Stocker T. Isotopic tracing (Sr, Nd, U and Hf) of continental and marine aerosols in an 18th century section of the Dye-3 ice core (Greenland). Earth and Planetary Science Letters 2010; 295: 277-286.

Mahowald N, Ballantine J, Feddema J, Ramankutty N. Global trends in visibility: implications for dust sources. Atmospheric Chemistry and Physics 2007; 7: 3309-3339.

Mahowald NM, Baker AR, Bergametti G, Brooks N, Duce RA, Jickells TD, et al. Atmospheric global dust cycle and iron inputs to the ocean. Global biogeochemical cycles 2005; 19.

Mahowald NM, Luo C. A less dusty future? Geophysical Research Letters 2003; 30.

Mahowald NM, Muhs DR, Levis S, Rasch PJ, Yoshioka M, Zender CS, et al. Change in atmospheric mineral aerosols in response to climate: Last glacial period, preindustrial, modern, and doubled carbon dioxide climates. Journal of Geophysical Research: Atmospheres 2006; 111.

Mahowald NM, Rivera GDR, Luo C. Comment on "Relative importance of climate and land use in determining present and future global soil dust emission" by I. Tegen et al. Geophysical Research Letters 2004; 31.

Majestic BJ, Schauer JJ, Shafer MM, Turner JR, Fine PM, Singh M, et al. Development of a wet-chemical method for the speciation of iron in atmospheric aerosols. Environmental science & technology 2006; 40: 2346-2351.

Mantas VM, Pereira A, Morais PV. Plumes of discolored water of volcanic origin and possible implications for algal communities. The case of the Home Reef eruption of 2006 (Tonga, Southwest Pacific Ocean). Remote Sensing of Environment 2011; 115: 1341-1352.

Markle BR, Steig EJ, Roe GH, Winckler G, McConnell JR. Concomitant variability in high-latitude aerosols, water isotopes and the hydrologic cycle. Nature Geoscience 2018: 1.

Martin JH, Fitzwater SE. Iron deficiency limits phytoplankton growth in the north-east Pacific subarctic. Nature 1988; 331: 341.

Martin JH, Gordon RM, Fitzwater SE. Iron in Antarctic waters. Nature 1990; 345: 156.

Martínez-Garcia A, Rosell-Melé A, Jaccard SL, Geibert W, Sigman DM, Haug GH. Southern Ocean dust–climate coupling over the past four million years. Nature 2011; 476: 312.

Matsui H, Mahowald NM, Moteki N, Hamilton DS, Ohata S, Yoshida A, et al. Anthropogenic combustion iron as a complex climate forcer. Nature communications 2018; 9: 1593.

McConnell JR, Lamorey GW, Lambert SW, Taylor KC. Continuous ice-core chemical analyses using inductively coupled plasma mass spectrometry. Environmental science & technology 2002; 36: 7-11.

McEvoy A, Markvart T, Castañer L, Markvart T, Castaner L. Practical handbook of photovoltaics: fundamentals and applications: Elsevier, 2003.

Mendez J, Guieu C, Adkins J. Atmospheric input of manganese and iron to the ocean: Seawater dissolution experiments with Saharan and North American dusts. Marine Chemistry 2010; 120: 34-43.

Merényi G, Lind J, Eriksen TE. Luminol chemiluminescence: chemistry, excitation, emitter. Journal of Bioluminescence and Chemiluminescence 1990; 5: 53-56.

Meskhidze N, Chameides W, Nenes A. Dust and pollution: a recipe for enhanced ocean fertilization? Journal of Geophysical Research: Atmospheres 2005; 110.

Mills MM, Ridame C, Davey M, La Roche J, Geider RJ. Iron and phosphorus co-limit nitrogen fixation in the eastern tropical North Atlantic. Nature 2004; 429: 292.

Morel F, Hering JG, Hering JG. Principles and applications of aquatic chemistry: John Wiley & Sons, 1993.

Moteki N, Adachi K, Ohata S, Yoshida A, Harigaya T, Koike M, et al. Anthropogenic iron oxide aerosols enhance atmospheric heating. Nature Communications 2017; 8: 15329.

Newhall CG, Self S. The volcanic explosivity index (VEI) an estimate of explosive magnitude for historical volcanism. Journal of Geophysical Research: Oceans 1982; 87: 1231-1238.

Obata H, Nozaki Y, Okamura K, Maruo M, Nakayama E. Flow-through analysis of Al in seawater by fluorometric detection with the use of lumogallion. Field Analytical Chemistry & Technology 2000; 4: 274-282.

Oppenheimer C. Climatic, environmental and human consequences of the largest known historic eruption: Tambora volcano (Indonesia) 1815. Progress in Physical Geography: Earth and Environment 2003; 27: 230-259.

Oppenheimer C, Orchard A, Stoffel M, Newfield TP, Guillet S, Corona C, et al. The Eldgjá eruption: timing, long-range impacts and influence on the Christianisation of Iceland. Climatic Change 2018; 147: 369-381.

Paolo FS, Fricker HA, Padman L. Volume loss from Antarctic ice shelves is accelerating. Science 2015; 348: 327-331.

Parekh P, Dutkiewicz S, Follows M, Ito T. Atmospheric carbon dioxide in a less dusty world. Geophysical research letters 2006; 33.

Parrenin F, Barnola J-M, Beer J, Blunier T, Castellano E, Chappellaz J, et al. The EDC3 chronology for the EPICA Dome C ice core. Climate of the Past 2007; 3: 485-497.

Pascual C, Romay C. Effect of antioxidants on chemiluminescence produced by reactive oxygen species. Journal of bioluminescence and chemiluminescence 1992; 7: 123-132.

Pittino F, Ambrosini R, Azzoni R, Diolaiuti G, Villa S, Gandolfi I, et al. Post-Depositional Biodegradation Processes of Pollutants on Glacier Surfaces. Condensed Matter 2018; 3: 24.

Pullin MJ, Cabaniss SE. Colorimetric flow-injection analysis of dissolved iron in high DOC waters. Water research 2001; 35: 363-372.

Raible CC, Brönnimann S, Auchmann R, Brohan P, Frölicher TL, Graf HF, et al. Tambora 1815 as a test case for high impact volcanic eruptions: Earth system effects. Wiley Interdisciplinary Reviews: Climate Change 2016; 7: 569-589.

Raiswell R, Benning LG, Tranter M, Tulaczyk S. Bioavailable iron in the Southern Ocean: the significance of the iceberg conveyor belt. Geochemical transactions 2008; 9: 7.

Rignot E, Velicogna I, van den Broeke MR, Monaghan A, Lenaerts JT. Acceleration of the contribution of the Greenland and Antarctic ice sheets to sea level rise. Geophysical Research Letters 2011; 38.

Rogan N, Achterberg EP, Le Moigne FA, Marsay CM, Tagliabue A, Williams RG. Volcanic ash as an oceanic iron source and sink. Geophysical Research Letters 2016; 43: 2732-2740.

Rose AL, Waite TD. Chemiluminescence of luminol in the presence of iron (II) and oxygen: oxidation mechanism and implications for its analytical use. Analytical chemistry 2001; 73: 5909-5920.

Rue EL, Bruland KW. The role of organic complexation on ambient iron chemistry in the equatorial Pacific Ocean and the response of a mesoscale iron addition experiment. Limnology and oceanography 1997; 42: 901-910.

Saitoh K, Hasebe T, Teshima N, Kurihara M, Kawashima T. Simultaneous flow-injection determination of iron (II) and total iron by micelle enhanced luminol chemiluminescence1. Analytica Chimica Acta 1998; 376: 247-254.

Saiz-Lopez A, Mahajan AS, Salmon RA, Bauguitte SJ-B, Jones AE, Roscoe HK, et al. Boundary layer halogens in coastal Antarctica. Science 2007; 317: 348-351.

Saiz-Lopez A, Plane J, Mahajan A, Anderson P, Bauguitte S-B, Jones A, et al. On the vertical distribution of boundary layer halogens over coastal Antarctica: implications for O 3, HO x, NO x and the Hg lifetime. Atmospheric Chemistry and Physics 2008; 8: 887-900.

Sanderson P, Su S, Chang I, Saborit JD, Kepaptsoglou D, Weber R, et al. Characterisation of iron-rich atmospheric submicrometre particles in the roadside environment. Atmospheric Environment 2016; 140: 167-175.

Santana-Casiano JM, González-Dávila M, Fraile-Nuez E, De Armas D, González AG, Domínguez-Yanes JF, et al. The natural ocean acidification and fertilization event caused by the submarine eruption of El Hierro. Scientific reports 2013; 3: 1140.

Santana-González C, Santana-Casiano JM, González-Dávila M, Fraile-Nuez E. Emissions of Fe (II) and its kinetic of oxidation at Tagoro submarine volcano, El Hierro. Marine Chemistry 2017; 195: 129-137.

Savarino J, Legrand M. High northern latitude forest fires and vegetation emissions over the last millennium inferred from the chemistry of a central Greenland ice core. Journal of Geophysical Research: Atmospheres 1998; 103: 8267-8279.

Schallenberg C, van der Merwe P, Chever F, Cullen JT, Lannuzel D, Bowie AR. Dissolved iron and iron (II) distributions beneath the pack ice in the East Antarctic (120 E) during the winter/spring transition. Deep Sea Research Part II: Topical Studies in Oceanography 2016; 131: 96-110.

Schlesinger WH, Bernhardt ES. Biogeochemistry: an analysis of global change: Academic press, 2013.

Scott W, Gardner C, Devoli G, Alvarez A. TheA. D. 1835 eruption ofVolcán Cosigüina, Nicaragua: A guide for assessing local volcanic hazards. Volcanic Hazards in Central America 2006; 412: 167.

Sedwick PN, Sholkovitz ER, Church TM. Impact of anthropogenic combustion emissions on the fractional solubility of aerosol iron: Evidence from the Sargasso Sea. Geochemistry, Geophysics, Geosystems 2007; 8.

Seitz WR, Hercules DM. Determination of trace amounts of iron (II) using chemiluminescence analysis. Analytical Chemistry 1972; 44: 2143-2149.

Severi M, Udisti R, Becagli S, Stenni B, Traversi R. Volcanic synchronisation of the EPICA-DC and TALDICE ice cores for the last 42 kyr BP. Climate of the Past 2012; 8: 509-517.

Shaked Y, Kustka AB, Morel FM. A general kinetic model for iron acquisition by eukaryotic phytoplankton. Limnology and Oceanography 2005; 50: 872-882.

Sigl M, Winstrup M, McConnell J, Welten K, Plunkett G, Ludlow F, et al. Timing and climate forcing of volcanic eruptions for the past 2,500 years. Nature 2015; 523: 543.

Sigman DM, Hain MP, Haug GH. The polar ocean and glacial cycles in atmospheric CO 2 concentration. Nature 2010; 466: 47.

Smetacek V, Klaas C, Strass VH, Assmy P, Montresor M, Cisewski B, et al. Deep carbon export from a Southern Ocean iron-fertilized diatom bloom. Nature 2012; 487: 313.

Spirakis CS. Iron fertilization with volcanic ash? Eos, Transactions American Geophysical Union 1991; 72: 525-525.

Spolaor A, Vallelonga P, Cozzi G, Gabrieli J, Varin C, Kehrwald N, et al. Iron speciation in aerosol dust influences iron bioavailability over glacial-interglacial timescales. Geophysical Research Letters 2013a; 40: 1618-1623.

Spolaor A, Vallelonga P, Gabrieli J, Cozzi G, Boutron C, Barbante C. Determination of Fe2+ and Fe3+ species by FIA-CRC-ICP-MS in Antarctic ice samples. Journal of Analytical Atomic Spectrometry 2012; 27: 310-317.

Spolaor A, Vallelonga P, Gabrieli J, Roman M, Barbante C. Continuous flow analysis method for determination of soluble iron and aluminium in ice cores. Analytical and bioanalytical chemistry 2013b; 405: 767-774.

Stookey LL. Ferrozine---a new spectrophotometric reagent for iron. Analytical chemistry 1970; 42: 779-781.

Strong A, Chisholm S, Miller C, Cullen J. Ocean fertilization: time to move on. Nature 2009; 461: 347.

Takenaka N, Ueda A, Daimon T, Bandow H, Dohmaru T, Maeda Y. Acceleration mechanism of chemical reaction by freezing: The reaction of nitrous acid with dissolved oxygen. The Journal of Physical Chemistry 1996; 100: 13874-13884.

Talbot R, Andreae M, Berresheim H, Jacob DJ, Beecher K. Sources and sinks of formic, acetic, and pyruvic acids over Central Amazonia: 2. Wet season. Journal of Geophysical Research: Atmospheres 1990; 95: 16799-16811.

Tegen I, Werner M, Harrison S, Kohfeld K. Relative importance of climate and land use in determining present and future global soil dust emission. Geophysical Research Letters 2004; 31.

Thordarson T, Self S. Atmospheric and environmental effects of the 1783–1784 Laki eruption: A review and reassessment. Journal of Geophysical Research: Atmospheres 2003; 108.

Vaughan NE, Lenton TM. A review of climate geoengineering proposals. Climatic change 2011; 109: 745-790.

Wang S, Bailey D, Lindsay K, Moore J, Holland M. Impact of sea ice on the marine iron cycle and phytoplankton productivity. 2014.

Watson AJ. Volcanic iron, CO2, ocean productivity and climate. Nature 1997; 385: 587.

Weissbach S, Wegner A, Opel T, Oerter H, Vinther B, Kipfstuhl S. Spatial and temporal oxygen isotope variability in northern Greenland–implications for a new climate record over the past millennium. Climate of the Past 2016; 12: 171-188.

Wiggs GF, O'hara SL, Wegerdt J, Van Der Meer J, Small I, Hubbard R. The dynamics and characteristics of aeolian dust in dryland Central Asia: possible impacts on human exposure and respiratory health in the Aral Sea basin. Geographical Journal 2003; 169: 142-157.

Williams M. The∼ 73 ka Toba super-eruption and its impact: History of a debate. Quaternary International 2012; 258: 19-29.

Wingenter OW, Haase KB, Strutton P, Friederich G, Meinardi S, Blake DR, et al. Changing concentrations of CO, CH4, C5H8, CH3Br, CH3I, and dimethyl sulfide during the Southern Ocean Iron Enrichment Experiments. Proceedings of the National Academy of Sciences 2004; 101: 8537-8541.

Xuan J, Sokolik IN. Characterization of sources and emission rates of mineral dust in Northern China. Atmospheric Environment 2002; 36: 4863-4876.

Yalcin K, Wake CP, Kreutz KJ, Germani MS, Whitlow SI. Ice core evidence for a second volcanic eruption around 1809 in the Northern Hemisphere. Geophysical Research Letters 2006; 33.

Zhuang G, Yi Z, Duce RA, Brown PR. Link between iron and sulphur cycles suggested by detection of Fe (n) in remote marine aerosols. Nature 1992; 355: 537.

Zielinski GA. Use of paleo-records in determining variability within the volcanism–climate system. Quaternary Science Reviews 2000; 19: 417-438.